Master's thesis

NTNU
Norwegian University of Science and Technology
Faculty of Information Technology and Electrical Engineering
Department of Electric Power Engineering

Mohammad Heidari

Control Models for Providing Virtual Inertia to the Electrical Grid of Offshore Platforms With Large Contribution of Offshore Wind

Master's thesis in Renewable Energies in the Marine Environment
Supervisor: Prof. Elisabetta Tedeschi
Co-supervisor: Salvatore D'Arco
June 2021

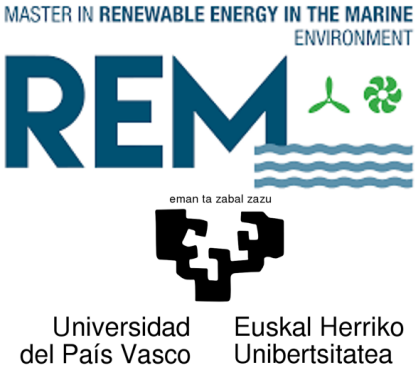

NTNU
Norwegian University of Science and Technology

Mohammad Heidari

Control Models for Providing Virtual Inertia to the Electrical Grid of Offshore Platforms With Large Contribution of Offshore Wind

Master's thesis in Renewable Energies in the Marine Environment
Supervisor: Prof. Elisabetta Tedeschi
Co-supervisor: Salvatore D'Arco
June 2021

Norwegian University of Science and Technology
Faculty of Information Technology and Electrical Engineering
Department of Electric Power Engineering

NTNU
Norwegian University of
Science and Technology

Control Models for Providing Virtual Inertia to the Electrical Grid of Offshore Platforms With Large Contribution of Offshore Wind

Mohammad Heidari

June 2021

Summary

Norway as one of the leading countries in the oil and gas and (floating) offshore wind energy sectors, plans to reduce its carbon emission according to the European commission strategy to become carbon-neutral by 2050. One of the considerable contributors to the carbon emission in Norway are oil and gas platforms. Supplying these platforms thorough offshore wind can accelerate realizing carbon-neutrality.

A well-built grid can withstand a contingency event and have an acceptable rate of change of frequency due to high inertial characteristics. The reduction of the grid inertia is one of the main issues with the paced integration of renewable energy sources into the electricity grid and replacing the conventional generators. To overcome this issue, multiple mathematical methods have been developed to ensure grid stability. These methods are based on an additional energy source to help the system stability throughout the event of a contingency.

In this project, a few of the methods to provide virtual inertia for renewable energy sources are reviewed and compared against each other. Based on the ideas inspired by these methods, an algorithm is proposed to assist the inertial response of the grid of oil and gas platforms.

The proposed algorithm is implemented on a voltage source inverter that extracts energy from energy storage and injects it into the grid of the platform alongside gas and wind turbines. The method is validated by a step-change in the load of the platform and the interactions of the grid components are presented. Compared to a scenario in which there is no inertial support provided, the proposed method proves operational in reducing the rate of change of frequency and therefore, stabilizing the grid during the contingency.

Key words: Electrification of oil and gas platforms, Offshore wind turbine, Virtual inertia, vector control of converter, Back to back converter control, DFIG, gas turbine, Energy storage

Acknowledgements

I have been studying abroad as part of the Erasmus Mundus joint master program REM (Renewable energies in the marine environment) and I would like to extend my gratitude towards the REM joint board of coordinators from the universities of Strathclyde, UPV/EHU, and NTNU. This work could not have been possible without the support and guidance of my coordinators, lecturers, and supervisors. I would also like to thank Ph. D. candidate Daniel Mota for his continuous help for the past six months. In the end, I want to thank my friends and family for their emotional support during the two years of my studies abroad.

Mohammad Heidari
June 2021

Contents

Figures

Tables

Acronyms

$Mil.Sm^3$ Million Standard cubic meters. 139

Q_{inj} Injection Rate. 140

Q_{oil} Oil Production. 140

AVR Automatic Voltage Regulator. 39, 40, 54, 55

CSC Current Source Converter. 17

CSV Constant Stator Voltage. 70

DCF Distortion Component factor. 36

DFIG Doubly Fed Induction Generator. viii, 9–11, 15, 32, 51, 57, 60, 62, 63, 67–69, 73, 74, 81, 83–86, 89, 92, 93, 100, 129

DG Distributed Generation. 47

DSP Digital Signal Processing. 36

ENTSOE European Network of Transmission System Operators for Electricity. 17

ESS Energy Storage System. 1, 14, 31, 44, 50–52, 54, 77, 78, 112, 115, 122, 127, 129–131

GOR Gas Oil Ratio. 140

GSC Grid Side Converter. 10, 17, 51, 57, 69, 75–77, 93, 100, 106, 111

GTO Gate Turn Off transistor. 17

IEPE Institute of Electrical Power Engineering. 35, 36, 49

IGBT Insulated Gate Bipolar Transistors. 14, 17

IGCT Integrated Gate Commutated Thyristor. 14

KHI Kawasaki Heavy Industries. 39, 40, 49

LEOGO Low Emission Oil and Gas Open. 5, 6, 53, 139

MOSFET Metal Oxide Semiconductor Field Effect Transistor. 14, 17

MPPT Maximum Power Point Tracking. 51, 67, 71, 74, 75, 89, 92, 100, 101, 106, 107, 129

NCS Norwegian Continental Shelf. 5

NREL National Renewable Energy Lab (US). 1

NTNU Norges teknisk-naturvitenskaplige universitet. 2

PCC Point of Common Coupling. 37, 76, 86, 111, 112, 129

PFCC power Factor Correction Capacitor. 16

PLL Phase-Locked Loop. 19, 32, 34, 36, 40, 41, 44, 47, 49, 71

PMSG Permanent Magnet SG. 7, 9, 16

PSD Power Spectral Density. 59

PWM Pulse Width Modulation. 22–25, 28, 32, 41, 44, 70, 71, 100, 111

R&D Research and Development. 6

RES Renewable Energy Source. 1, 14, 18, 31, 129

ROCOF Rate of Change of Frequency. 1, 9, 13, 44, 45, 125, 130

RSC Rotor Side Converter. 51, 57, 69, 70, 76, 93, 100, 106, 129

SCIG Squirrel Cage Induction Generator. 15, 16

SG Synchronous Generator. 1–3, 5–8, 10, 13, 16, 18, 31, 32, 34, 35, 37, 39, 41, 43, 44, 47, 49, 54, 115, 129

SMES Superconducting Magnetic Energy Storage. 17

SOC State of Charge. 44

SPC Synchronous power Controller. 43, 49

SRM Spectral Representation Method. 59

SVPWM Space Vector Pulse Width Modulation. 25, 28, 71, 72, 129

THD Total harmonic Distortion. 20

TSR Tip Speed Ratio. 65, 68

UPF Unity power Factor. 70

UPS Uninterrupted Power Supply. 139

VIC Virtual Inertia Converter. 77, 78

VISMA Virtual Synchronous Machine. 35

VOC Virtual Oscillator Controller. 19, 47

VSC Voltage Source Converters. 17

VSD Variable Speed Drive. xvii, 144

VSG Virtual Synchronous Generator. 39, 41, 43, 44

VSM Virtual Synchronous Motor. 32, 34

WC Water Cut. 140

WRIG Wound Rotor Induction Generator. 15

ZDC Zero D-axis Current. 70

Chapter 1

Introduction

1.1 Introduction

The continuous increase of demand for carbon emission reduction entails the integration of the Renewable Energy Source (RES) into the electricity grids. One of the major concerns of this change is the downgrading of the system inertia. Power converters which are the main bridge between RES and the electricity grid do not possess any inherited inertia [1, 2].

National Renewable Energy Lab (US) (NREL) refers to inertia in the power systems as "the stored energy in large rotating masses which gives them the tendency to remain rotating" [3]. The inertia in the system is mainly the factor that stabilises Rate of Change of Frequency (ROCOF) after a contingency event. Consequently, if the inertia constant of the system components is not adequate, the system might experience a drastic ROCOF. On the other hand, high inertia, reinforces the grid and prevents cascading failures and undesirable load shedding. In order to tackle this problem the concept of virtual inertia was introduced.

Virtual, synthetic, or hidden inertia is referred to any combination of power electronic components, Energy Storage System (ESS), RES, and control algorithms that virtually mimics the inertial response of the conventional power systems [4–6]. This virtual inertial response is the result of modifying the classic control methods of the power electronic converters. This modification generally aims to extract more energy from any stored form of energy behind the converters while reducing the ROCOF in comparision with a scenario in which the converters are controlled with the classic methods. From the grid viewpoint, this response is the same as the one from a Synchronous Generator (SG) in the event of a contingency.

1.2 Motivation

The oil and gas sector plays a vital role in financing the Norwegian economy. However, it is also one of the country's key carbon emitters. Roughly 20% of Nor-

way's total greenhouse gas emissions come from the offshore gas turbines operating on the Barents, North and Norwegian Seas. More environmentally friendly solutions, like offshore wind, have the potential to cut drastically those carbon emissions. However, as mentioned in section 1.1, wind generators and their power electronic converters lack the inherent inertia of SG that stabilizes electrical systems. Therefore, a deep understanding of virtual inertia strategies and their simulation models is necessary in order to study the impact of the integration of wind-farms into offshore platforms.

This thesis focuses on modeling control strategies for maintaining the stability of an offshore platform electrical system with a large contribution of wind energy. The project is a part of the Low emission Sub-Project on Energy Systems and Digital Solutions of the Low emission Research Centre, a cooperation between Norges teknisk-naturvitenskaplige universitet (NTNU) and SINTEF A. S. with the goal of developing technologies and solutions for reducing the offshore greenhouse gas emissions on the Norwegian Continental Shelf by 40% within 2030 and move towards zero emissions in 2050.

1.3 Objectives and Research Questions

The project is divided into smaller parts with separate goals for convenience and in the end assembled back together. The following objectives are defined to develop the model:

- Selection and modeling the wind farm and its control strategy
- Selection and modeling the energy source to provide virtual inertia
- Selection and modeling the control strategy to emulate the virtual inertia
- Modeling the grid of the oil and gas platform
- Assemble each part to build the complete model
- Successfully run the model and illustrate the operation of the virtual inertia control strategy

During the modeling of the grid of the oil and gas platform, the following research questions have to be answered:

- What are the important loads on the grid of oil and gas platform? How can they be modeled? How much detail is required for the purpose of this study?
- What are the conventional energy sources on the platform? Should they be altered in any way to integrate the wind energy? Is it possible/necessary to completely remove these generators?

- How should the wind turbines be modeled? How are they connected to the oil and gas grid? What should be the control strategy for power converters? What are the limitations to be considered in the modeling?
- Which methods can be implemented for providing virtual inertia? What is the source of energy behind this inertia?
- How is the power distributed between the sources and the loads? What is the role of each component and how essential is their contribution?

1.4 Methodology

To achieve the set goals of this thesis, different control schemes are tested and implemented in the Simulink graphical modeling tool, within the MATLAB numerical integrated environment. The main contributions of the thesis can be identified as:

- Provide an overview of the existing methods to provide virtual inertia;
- Develop a control strategy to emulate virtual inertia for the platform;
- Evaluate the effectiveness of the proposed method in the electric grid the oil and gas platform.

1.5 Thesis Outline

Chapter 2 provides the background and concept of inertia in the power systems. In this chapter, the inertial response of the traditional power plants with SGs is studied. Furthermore, the characteristics and loads of the understudy oil and gas platform are introduced. Subsequently, the changes in the wind turbine technology is discussed and the necessity for virtual inertia is investigated. Additionally, this chapters discusses power converters and their relevant background. Chapter 3 thoroughly studies the methods to provide virtual inertia in the literature, while presenting a background to the changes in the proposals for tackling the issue. Chapter 4 discusses the proposed method to emulate virtual inertia for the offshore wind turbines that support the oil and gas platform and presents the case study. Chapter 5 discusses steps taken for the modeling of the entire system. Chapter 6 gathers the simulation results, pointing out the satisfactory emulation of the virtual inertia in the system. Finally, conclusions and recommendations for future work are offered in Chapter 7.

Chapter 2

Background

2.1 Introduction

The operation of the traditional power plants is entirely different from the operation of the offshore wind parks. However, in order to understand the essence of inertia in the power system, the traditional power plants must be part of the study. In the traditional power plants, during the event of an imbalance in the available power supply and load, the SGs speed up or slow down via the governor to compensate for the imbalance. In this chapter, the background of the electric system of the the oil and gas platforms is introduced. Afterward, the inertial response of the SGs is provided and a connection is made to the offshore wind farms and changes happening in the methods to provide inertia for wind farms are discussed. A thorough background for power converters and their relevant technologies are also presented.

2.2 Oil and Gas Platforms

The oil and gas offshore platforms consist of multiple energy-demanding units such as drilling, processing, exporting, and accommodation. Most platforms on the Norwegian Continental Shelf (NCS) generate their own electrical power by gas turbines. The gas turbines are also used to directly drive compressors and pumps. These gas turbines generate about 80% of the total CO_2 and emissions from offshore installations [7]. As mentioned in section 1.2, this thesis investigates methods to provide virtual inertia for oil and gas platforms supplied by wind turbines. Hence, an analysis and modeling of a typical oil and gas platform is essential.

A consortium consisting of Equinor, Sintef A. S., and Siemens A. S. started a project in 2016 to implement the integration of offshore wind with a stand-alone electric grid for oil and gas offshore installations. The Low Emission Oil and Gas Open (LEOGO) reference platform is selected as the main structure to study in

this thesis [8]. LEOGO is a hypothetical oil and gas developed by the Low Emission centre of the SINTEF A. S. for Research and Development (R&D) purposes. Figure 2.1 illustrates all the components in the hypothetical platform. This figure shows the connection of the energy storage, wind turbines, gas turbines and other components of the grid of the oil and gas platform. Since the main goal of this thesis is investigating the control methods to provide virtual inertia, less emphasis is put on modeling the loads of the platform itself, meaning that except the gas and wind turbines and energy storage unit, the rest of the components in figure 2.1 are not modeled in detail but a whole representation of the electric loads are considered. Nevertheless, the specific model of the system is thoroughly explained in Annex 7.2 for future reference. In this Annex, the details of the power suppliers of the platform and its main electrical loads are explained and the electrical grid of the platform is illustrated in Simulink. The complete model of the built system of this study is presented in chapter 4 and the modeling of each element is available in chapter 5.

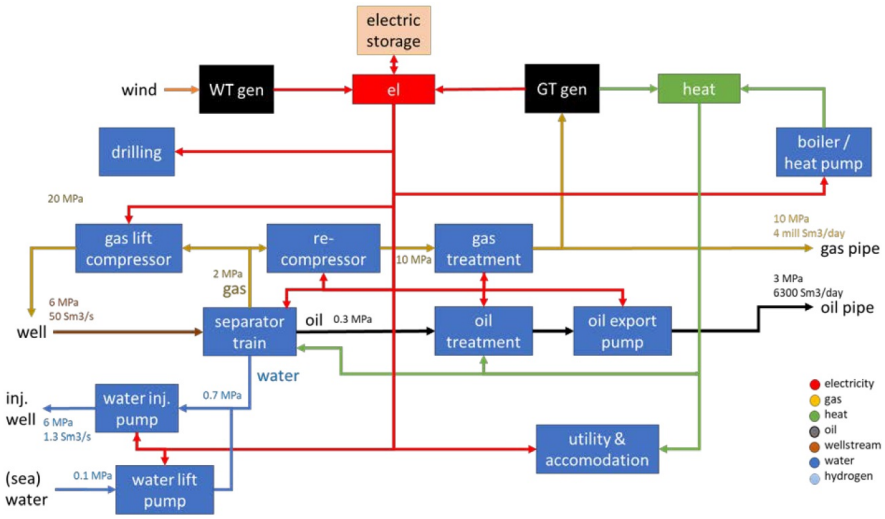

Figure 2.1: LEOGO platform main components and mass/energy flow [8]

2.3 Source of Inertia in the Power Systems

2.3.1 SG Model and Operation Principles

The SGs are the main source of energy supply to the electric grids. A SG consists of a set of windings that interact inside a magnetic field to convert mechanical energy into electricity: stator windings which are 3 AC winding distributed at 120° spaced along the circumference of the stator magnetic circuit and rotor winding which is a DC field winding. The shape of the rotor can be either rounded rotor (in turbogenerators- high speed prime movers) or salient pole rotor (in hydrogenerators- low speed prime movers). The field of the rotor can be created

either by a DC excitation (adding a DC field winding) or by using permanent magnets in the rotor (Permanent Magnet SG (PMSG)).

When the rotor shaft is turned by an external force, the rotor poles also rotate and create a rotating magnetic field B_R. As the magnetic field rotates, it passes from the stator windings and according to Faraday's law, an electromotive force (*emf*) is induced in the stator windings as illustrated in figure 2.2. The frequency of the output voltage depends on the number of pole pairs (P) and the rotational speed of the rotor also known as angular velocity (ω) in rad/s, Eq. 2.1 shows this relation:

$$f = \frac{P \cdot \omega}{2\pi} \tag{2.1}$$

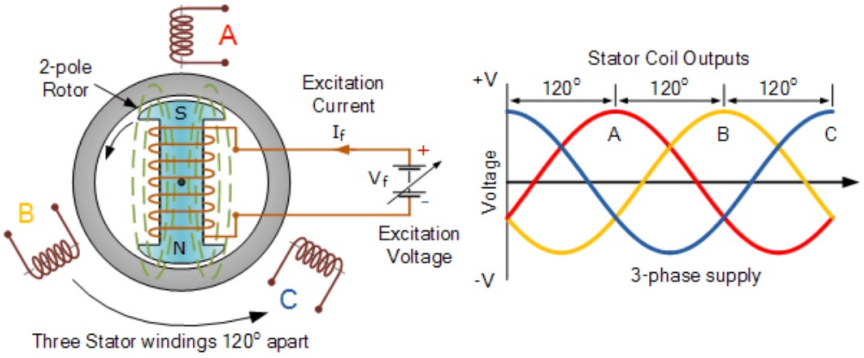

Figure 2.2: SG components and stator voltages [9]

The internal voltage E_A of the SG can be calculated from Eq. 2.2. In this equation, N_c is the number of conductors at angle zero. The induced voltage is proportional to the rotor flux φ for a given angular frequency. When generator is not loaded, the internal voltage is equal to the terminal voltage V_Φ and when loaded, current flows in stator windings which result in the rotating stator magnetic field. The voltage induced in the armature is the summation of the voltages induced by both rotor and stator fields. The output terminal voltage of the SG V_Φ,would be achieved by deducting the voltage drops from self and leakage inductances and resistance of the armature coils from the resultant voltage.

$$E_A = \sqrt{2}\pi N_c \varphi f \tag{2.2}$$

$$V_\Phi = E_A - I_A(R_s + jX_s) \tag{2.3}$$

If a load is connected to the output terminal of the generator, the current I_A starts to flow and the transmitted active and reactive power P, Q can be calculated:

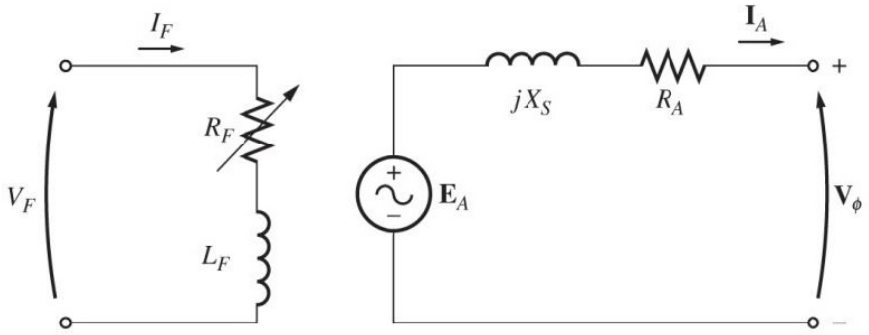

Figure 2.3: Simplified SG model

$$S = 3V_A \cdot I_A^*, \tag{2.4}$$

$$Z_s = R_s + jX_s \tag{2.5}$$

$$P = 3\frac{|E_A| \cdot |V_\Phi|}{|Z_s|} \cdot \cos(\gamma - \theta) - 3\frac{|V_\Phi|^2}{|Z_s|} \cdot \cos\gamma \tag{2.6}$$

$$Q = 3\frac{|E_A| \cdot |V_\Phi|}{|Z_s|} \cdot \sin(\gamma - \theta) - 3\frac{|V_\Phi|^2}{|Z_s|} \cdot \sin\gamma \tag{2.7}$$

in which, E_A, V_Φ are the internal and terminal voltages, γ, θ are the phase angle between E_A, V_Φ and V_Φ, I_A vectors and Z_s is the generator impedance. Considering that the value of R_s is quite negligible in the SG, the active and reactive powers can be simplified:

$$P = 3\frac{|E_A| \cdot |V_\Phi|}{|X_s|} \cdot \sin\theta \tag{2.8}$$

$$Q = 3\frac{|E_A| \cdot |V_\Phi| \cdot \cos\theta - |V_\Phi|^2}{|X_s|} \tag{2.9}$$

2.3.2 Traditional Power Plants

The main idea behind providing inertia for the grid in the traditional power plants was utilizing the capability of the SGs to slow down or speed up if necessary to cope with the power imbalances and provide a reasonable inertial response. The inertial response of a SGs follows the swing Eq. 2.10 [10]:

$$\frac{2H}{\omega}\frac{d^2\delta}{dt^2} = P_m - P_e = P_a \tag{2.10}$$

in which H is the inertial constant, ω is the angular velocity (synchronous speed), δ is the rotor angle and P_m and P_e are the mechanical and electrical power

respectively. The difference between P_m and P_e represents the accelerating/decelerating power (P_a) for the generator. In the normal operation with no power imbalance, the electrical and mechanical powers are equal and therefore, $P_a = 0$ and the generator runs at synchronous speed. The loads connected to the generator can vary (according to eq 2.8) much faster than the mechanical power of the generator because the generator inherits inertia and this can lead to instability.

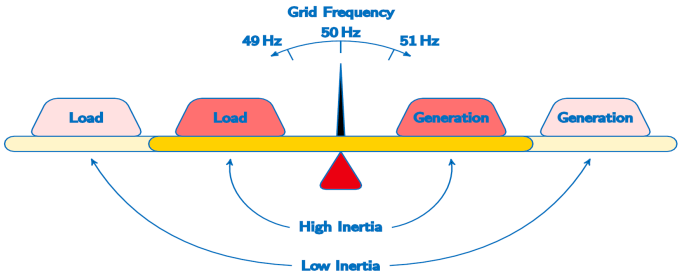

Figure 2.4: Low and high inertia concepts

The kinetic energy that is injected to the grid has to be replaced to provide support again if needed. Figure 2.4 illustrates the concept of the power imbalance in the system and the effect of inertia on the ROCOF. As the figure shows, lower inertia translates to faster ROCOF, which could be disastrous. Moreover, higher inertia constant allows larger imbalances to occur with slower ROCOF. Additionally, the inertial constant affects the frequency nadir as depicted in figure 2.5. Frequency nadir is the point in which the frequency the highest drop in value during a contingency event. Lower inertia leads to a lower frequency nadir, resulting in a higher probability of system collapse and failure [11].

2.3.3 DFIG model and operation principles

DFIGs have been used in wind turbines as a generator for a long time and although now PMSGs are preferred as the newer generators, a considerable portion of the installation still use DFIG. PMSGs are usually low speed and have no gearbox and their control strategy is straightforward but they are more expensive (additional cost because of the permanent magnets) and require full-rated converters due to the type 4 connection (explained in section 2.4.1) to the grid. On the other hand, lower cost (no need for permanent magnets and smaller scaled converters, usually one-third of the generator rated power) is an important advantage for DFIG, although considered as old-fashioned technology which needs gearbox [13]. This section explains the operation principles of DFIG based on [14] and chapter 10 of [15]. In this project, DFIG was selected instead of PMSG technology, hence the DFIG model is introduced more detailed.

A DFIG is supplied via a type three connection to the grid (explained in section

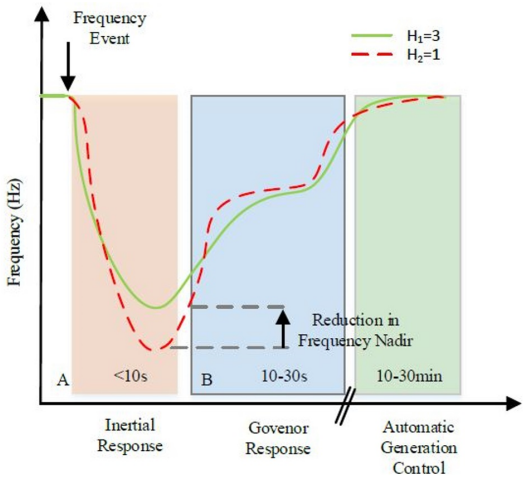

Figure 2.5: The inertial response of an SG with $H = 1$ (red) and $H = 3$ (green) to a contingency event [12]

2.4.1). Figure 2.6 illustrates the connection of the DFIG to the grid. Rotor and grid side filters are sometimes used for filtering the currents of the converters. Also, a capacitor is used in the DC link. The selection and design of the capacitor and filters are explained in chapter 5 under Grid Side Converter (GSC) control section. The model of the converter controllers are also presented in chapter 6.

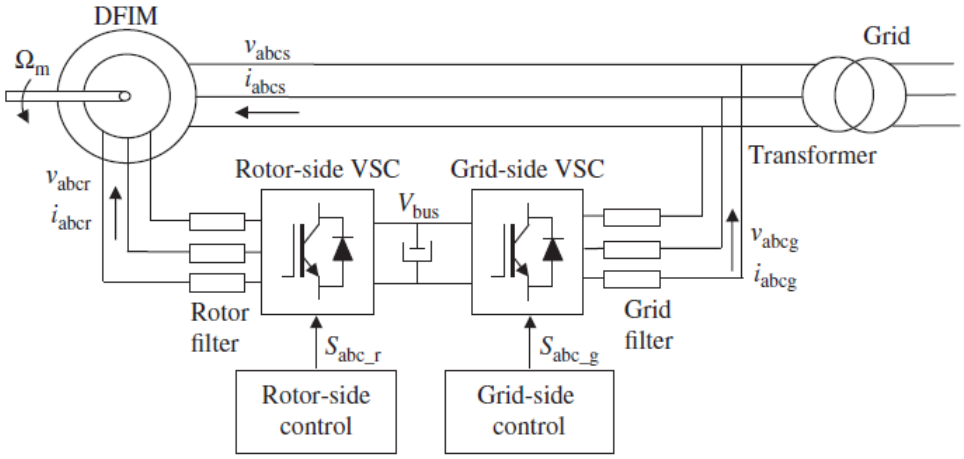

Figure 2.6: DFIG connection to the grid [15]

One of the main differences between DFIG and SG is that in DFIG the frequency in different windings are not identical. Eq 2.11 denotes the relation between the frequencies.

$$\omega_s = \omega_r + \omega_m \tag{2.11}$$

$$\omega_m = P \cdot \Omega_m \tag{2.12}$$

$$s = \frac{\omega_s - \omega_m}{\omega_s} = \frac{\omega_r}{\omega_s} \tag{2.13}$$

in which ω_s, ω_r and ω_m are the frequency of the stator, rotor voltages/currents and rotor electrical speed, respectively. Ω_m is the mechanical speed of the shaft, P is the number of pole pairs, and s is the slip of the machine. Note that, these equation are applicable both on speed and frequency. According to typical design of the DFIG, maximum slip can be considered 1/3 which means approximately 30 % of the stator power flows through the rotor. Since in most applications, the stator is directly connected to the grid, ω_s is equal to the grid frequency, known as synchronous frequency. A DFIG can operate in three different modes according to the previously mentioned speeds/frequencies:

- Sub-synchronous mode: $\omega_m < \omega_s \rightarrow \omega_r > 0 \rightarrow s > 0$
- Hyper-synchronous mode: $\omega_m > \omega_s \rightarrow \omega_r < 0 \rightarrow s < 0$
- Synchronous mode: $\omega_m = \omega_s \rightarrow \omega_r = 0 \rightarrow s = 0$

The relation between the stator and rotor winding turns are presented by parameter u, therefore the stator and rotor emf relations can be defined as:

$$E_{rs}^{'} = s\frac{E_s}{u} \tag{2.14}$$

In general to facilitate the analysis of the model, all the rotor parameters can be moved to the stator side. Figure 2.7 illustrates the schematic of this model. The rotor values when moved to the stator side (as shown in the figure) are as followed:

$$R_r = R_R^{'} \cdot u^2; L_{\sigma r} = L_{\sigma r}^{'} \cdot u^2; I_r = \frac{I_r^{'}}{u}; V_r = V_r^{'} \cdot u; E_{rs} = E_{rs}^{'} \cdot u \tag{2.15}$$

in which all the superscripted values are the original rotor values and the values without superscripts are the reflected values to the stator.

The power flow in the machine according to figure 2.7 can be expressed as followed:

$$P_s + P_r = P_{cu_s} + P_{cu_r} + P_m \tag{2.16}$$

in which P_s, P_r, P_{cu_s}, P_{cu_r} and P_m are stator, rotor, loss in stator, loss in rotor and shaft's mechanical powers. If P_m is positive, the machine is operating as generator

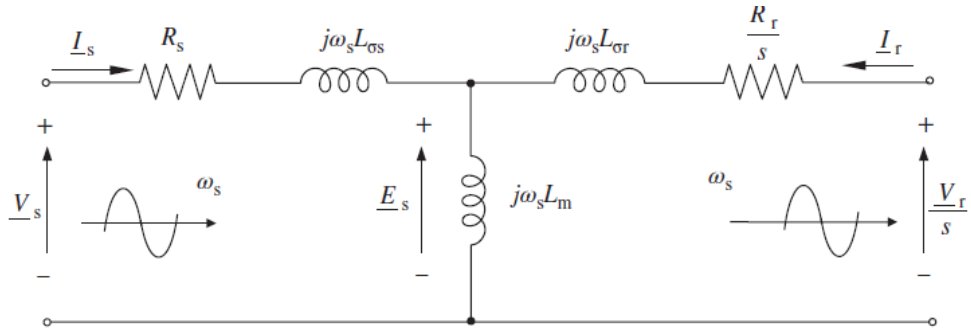

Figure 2.7: DFIG circuit [15]

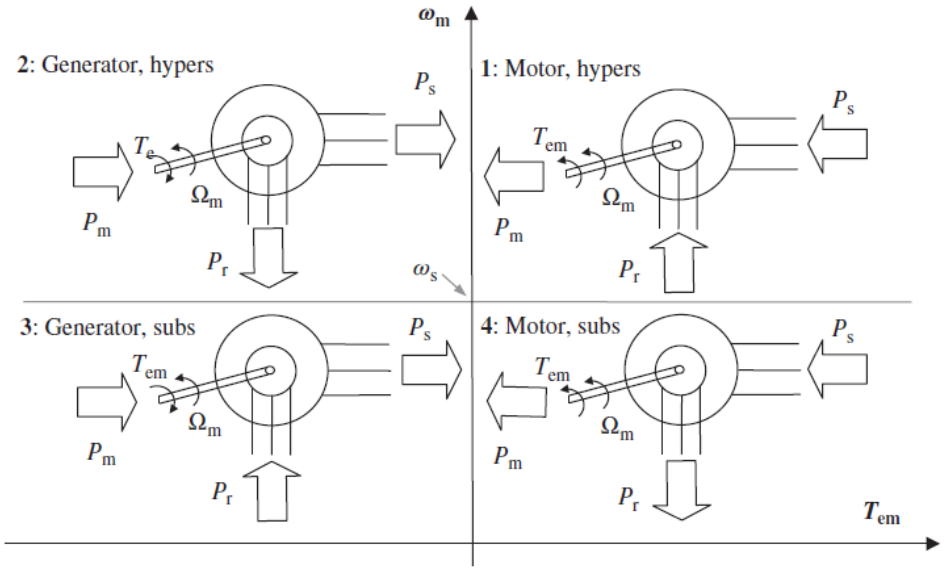

Figure 2.8: DFIG modes of operation [15]

and if P_m is negative, the machine runs as a motor. The sign of P_s is always opposite of P_m and the sign of P_r determines if the machine is in hyper-synchronous, sub-synchronous or synchronous modes. Figure 2.8 illustrates this concept.

The power parameters of the machine can be calculated from the classic power equations:

$$P_s = 3Re\{V_s \cdot I_s^*\}, \quad P_r = 3Re\{V_r \cdot I_r^*\} \tag{2.17}$$

$$Q_s = 3Im\{V_s \cdot I_s^*\}, \quad Q_r = 3Im\{V_r \cdot I_r^*\} \tag{2.18}$$

Substituting the values from KVL in circuit of figure 2.7:

$$P_s = 3R_s \mid I_s \mid^2 + 3\omega_s L_m Im\{I_s \cdot I_r^*\}, \quad P_r = 3R_r \mid I_r \mid^2 - 3s\omega_s L_m Im\{I_s \cdot I_r^*\} \tag{2.19}$$

$$Q_s = 3\omega_s L_s \mid I_s \mid^2 + 3\omega_s L_m Re\{I_s \cdot I_r^*\}, \quad Q_r = 3s\omega_s L_s \mid I_r \mid^2 + 3s\omega_s L_m Re\{I_s \cdot I_r^*\} \tag{2.20}$$

Additionally, the electromagnetic torque of the shaft can be written as:

$$P_{mec} = T_{em} \cdot \omega_m = T_{em} \frac{\omega_m}{P} \tag{2.21}$$

$$\begin{gathered} T_{em} = 3PL_m Im\{I_r^* \cdot I_s\} = 3P\frac{L_m}{L_s} Im\{\phi_s \cdot I_r^*\} = \\ 3P \cdot Im\{\phi_s^* \cdot I_s\} = 3P \cdot Im\{\phi_r \cdot I_r^*\} = \\ 3\frac{L_m}{L_r} P \cdot Im\{\phi_r^* \cdot I_s\} = 3P\frac{L_m}{\sigma L_s L_r} Im\{\phi_s \cdot \phi_r^*\} \end{gathered} \tag{2.22}$$

where $\sigma = 1 - L_m^2 / L_s L_r$. The copper losses can be neglected in the calculations to perform faster analysis and since the stator voltage is constant, the rotor voltage will only depend on slip/speed. With these assumptions in mind, the operation of the machine can be divided into four categories as demonstrated in figure 2.8.

2.3.4 Inertia for Wind Turbines

Unlike traditional power plants, the wind turbines have to compensate for the inertia by other means, due to the decoupling between grid and generators via the converters. One method to provide Inertia could be through the kinetic energy in the blades [3]. This service requires the operation of the wind turbine to be in the overloaded power zone for 100 *ms* and while slowing down the turbine and the reduction of ROCOF, other generators in the grid will have the window to inject more power to the grid and balance the system. Although, extra caution has to be applied in extracting this energy, since the wind turbine requires certain kinetic energy to operate continuously and if this energy is extracted, it must be replaced as quickly as possible, same as in SGs. Moreover, this is not always the situation in the industry and power deficit can be the main issue, therefore in this project the scenarios are defined based on power deficit.

Wind turbine installations are mostly shifting towards operating at variable speeds and connection via back-to-back converters, decoupling the grid and the turbine entirely [16]. Figure 2.9 illustrates the inertial constant of wind turbine technologies based on the size of the generation unit. The trend in the literature of wind turbines implies that with the increasing demand for variable speed wind turbines, the inertial response has to be much more scrutinised.

Expanding the control algorithms of the wind turbine is the key to introducing virtual inertia, and the desired response for the system can be implemented by producing feedback signals from terminal current and voltage of the point of common coupling [18].

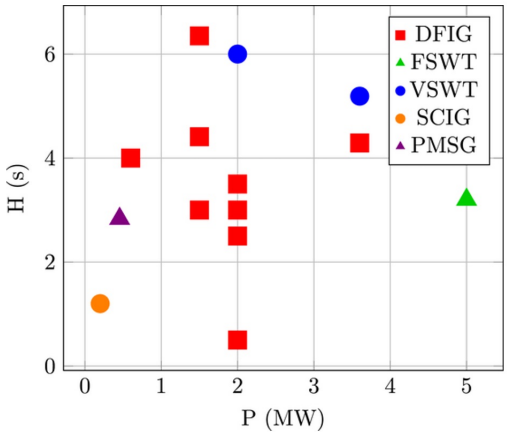

Figure 2.9: Inertia constant for different wind turbine technologies [17]

2.4 Converter Technology

Power converters are used for converting AC or DC voltages to AC or DC voltages with different amplitude and/or frequency. DC to AC converters, also known as inverters, are commonly used to connect the DC sources such as RESs and ESSs to the AC electrical grid. At the same time, the opposite applies to AC to DC converters (rectifiers). Additionally, to synchronize two grids with different frequencies converters can be used. A typical converter consists of a set of static and/or mechanical parts. The most recent converters are utilizing the semiconductor technology of controllable or uncontrollable switches (such as diodes, thyristors, Insulated Gate Bipolar Transistors (IGBT), Integrated Gate Commutated Thyristor (IGCT), Metal Oxide Semiconductor Field Effect Transistor (MOSFET)) to perform switching in the circuits and obtaining the desirable waveforms.

Figure 2.10 illustrates a simple controllable 3 phase back to back converter that connects a three phase generator to an AC grid via a DC link in between, and IGBT switches. As connecting the generator side with a DC link to the grid in long distance HV applications has proven to be less costly than traditional AC lines, more and more DC links are emerging worldwide to connect the RES plants to electrical grid [19]. Power converters can be categorized based on different principles such as application, types of connection to the grid, voltage or current source based, grid forming or grid following and generally depending on the control methods defined for the converter. As the links between power plants, grids and customers, converters play a substantial role in controlling the grid properties and ensuring power quality.

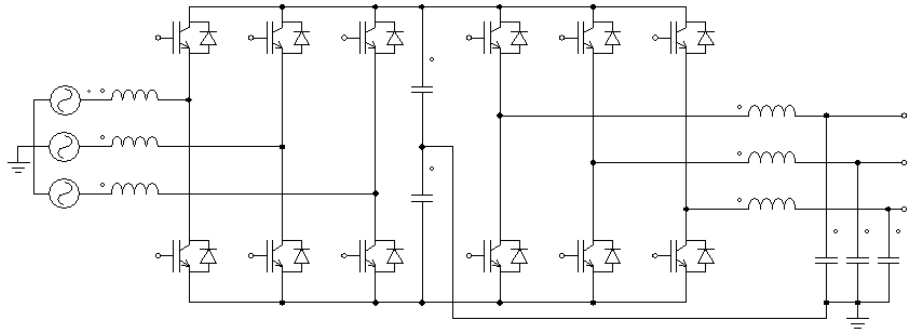

Figure 2.10: A 3 phase back to back converter

2.4.1 Types of grid connection for wind turbines

Wind turbines are usually classified by the control strategies implemented for mechanical power and generator speed. A common classification method is stall vs. pitch regulated turbines. In the stall regulated category, the wind turbine blades are shaped in such way that for very high speed winds, the airfoils generate less aerodynamic force, thus resulting in reduction of torque. While in the pitch regulation, the blades are twisted around their axis and as the speed of the wind increases, the blades are pitched into a new position to capture maximum energy or protect the blade if necessary. Another categorization of the wind turbines are called types. 4 main types are defined for wind turbines:

- Type 1:
  limited variable speed (type 1), which consists of a Squirrel Cage Induction Generator (SCIG) connected directly to a transformer and operates at grid frequency. The operating speed of the turbine, under steady condition is almost a linear function of the torque for a certain wind speed.

- Type 2:
  Similar to type 1, type 2 wind turbine has limited variability in the speed,

  while it consists of a Wound Rotor Induction Generator (WRIG). The connection is also similar to type 1 and directly via a step up transformer, although a variable resistor is added in the rotor circuit. The resistor is usually a set of resistors and power electronics components external to the rotor, and the current flows in the slip rings connected to the rotor. If the resistor is mounted directly on the rotor, the need for slip rings is eliminated and the model is called Weier design. The addition of resistors enables the control for the current and provision of constant power, even during gust winds and disturbances.

- Type 3:
  Type 3 wind turbines, commonly known as DFIG, benefit from variable speed control with partial power electronic conversion technology. In this

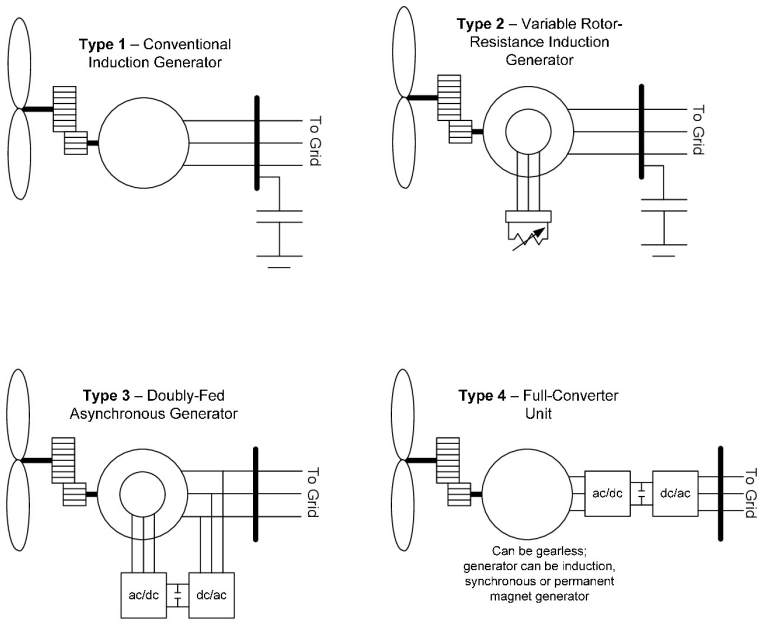

Figure 2.11: Different wind turbine types [20]

model in addition to advantages of type 2, a variable AC excitation system is added to the rotor circuit, which is supplied through slip rings and a voltage sourced converter. The converter is then connected back to back with a grid side converter that exchanges power with the electric grid.

- Type 4:
  Type 4 turbines have great flexibility as they are both variable speed and incorporate full power electronic conversion technology. In this model, the gearbox can be eliminated as the machine can spin at slow turbine speeds and considerably less frequencies than the grid. The generator can be wound rotor synchronous machines, PMSG, or SCIG.

Another type of wind turbine technology (type 5) is also available which is not used quite often. In this type, a typical variable speed wind turbine is connected to the grid by a speed/torque converter which is coupled with a SG. The converter changes the variable speed of the rotor shaft to a constant output speed.The topology of the four main types can be found in figure 2.11.

Grid codes of different countries have certain requirements for wind farms and the properties such as voltage, active and reactive power must be kept in certain ranges. Other requirements are also set by grid codes and generally all of them can be categorized into 5 sections of frequency stability, robustness, system restoration, general system management and voltage stability. As mentioned before, the control capabilities of a wind turbine generator depend on the generator type. Types 1 and 2 can not control the voltage and they use power Factor Correction

Capacitor (PFCC)s to maintain active, reactive powers and voltage in a desirable region. Types 3 and 4 are capable of controlling the voltage by varying reactive power at specified active power and voltage set points. Types 3 and 4 are more common as they offer not only this flexibility but also fulfill other requirements of the grid codes.

2.4.2 Voltage source vs current source converters

European Network of Transmission System Operators for Electricity (ENTSOE) defines Voltage Source Converters (VSC) as "self-commutated converters that connect HVAC and HVDC systems using devices suitable for high power electronic applications, such as IGBTs." The simplest difference between voltage source and Current Source Converter (CSC) as evident by their name is the DC side parameter. If the voltage on the DC side is constant, it considered a voltage source converter, while if the current of the DC link is constant, the converter is current sourced.

The notable characteristics of the two technologies are as followed:

VSC-

- Input voltage is constant
- Output voltage is independent of the load
- Output current depends on the load
- Needs feedback diodes
- Complicated commutation circuit
- MOSFET, IGBT, Gate Turn Off transistor (GTO) can be used

CSC-

- Input current is constant
- The magnitude of the output current is independent of load
- Output voltage depends on the load
- Does not need feedback diodes
- Simple commutation circuit
- MOSFET, IGBT, GTO can not be used

VSCs are preffered to CSCs in most of the applications for their benefits. Ac motor drive, Superconducting Magnetic Energy Storage (SMES) are application that GSC is preferred to VSC [21].

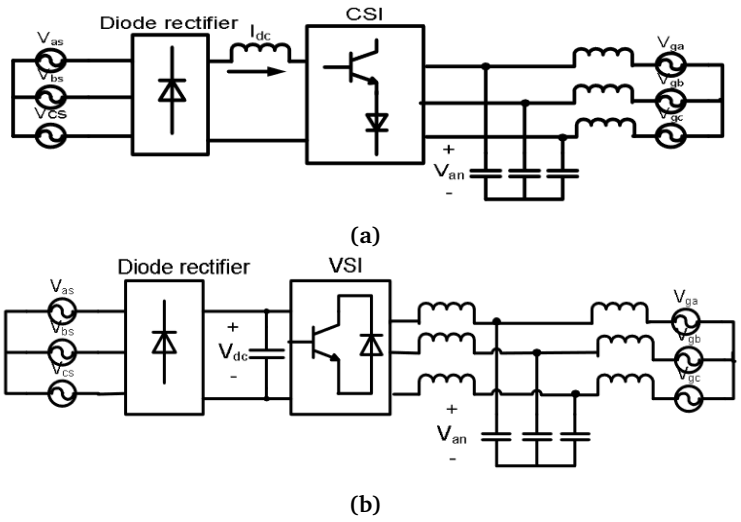

Figure 2.12: (a) CSC, (b) VSC topologies [21]

2.4.3 Grid forming vs grid following converters

The RESs such as wind farms are connected to the grid thorough the power converters. These converters are operated in either grid following or grid forming modes. Currently, most of the converters operate in the grid following mode but in islanded mode of microgrids they should be capable of operating in the grid forming mode. If the converter regulates the power output by measuring the angle of the grid voltage, it is operating as a grid following unit and follows the grid voltage angle and frequency without actively controlling them. On the other hand, the grid forming mode engages with controlling frequency and voltage angle, widely used in microgrid applications [22].

In the grid forming units, the rotational speed of the SG is directly linked with the frequency and by changing the speed, the frequency can be controlled. However, for the wind turbines with less support from SG, other algorithms are proposed to achieve the grid forming/following modes of operation for the converters. These methods are discussed in the next chapter.

Figure 2.13 depicts a simple example of the algorithm for the grid following and forming converter units in a *PV* plant. As illustrated, in the grid following mode, voltage angle and frequency are inputs and power is the output of the control algorithm. However, in the grid forming unit, the power is input and the voltage angle and frequency are the outputs of the control algorithm.

2.4.4 PLL units

Grid connected converters commonly require a dedicated synchronization to provide the phase and frequency of the grid voltage, in order to be connected to

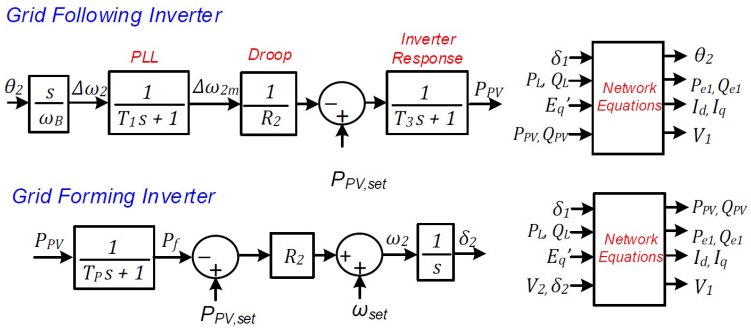

Figure 2.13: A simple Grid forming (down) and grid following (up) algorithm for a PV power plant [23]

the grid smoothly. A Phase-Locked Loop (PLL) is a control system that generates an output signal whose phase is related to the phase of the input signal. This implies that the frequency of both input and output signals are the same. Different PLL models can also generate signals with frequencies of multiple times of the input frequency.

The basic concept of operation of the PLL units are rather simple, however the mathematical analogy and the elements involved can be complicated. The diagram for a basic PLL is provided in figure 2.14. In this model, the signals from Virtual Oscillator Controller (VOC) and reference signal are connected to the input ports of the phase detector. Here the phase signals from the two inputs are compared and an error signal is generated. Then a low pass loop filter, receives the error signal from the phase detector and removes any high frequency harmonics that the signal might have. Then the error signal is passed back to the VOC as its tuning voltage. The operation of the loop is in such way that it reduces the difference in phase of the two main signals and synchronises their frequencies. The looping operation continues until the phase detector can not generate the error signal and the loop will be locked. In chapter 5, the proposed model for synchronization is discussed.

The main advantage of the PLL units as mentioned, are the synchronisation capability they offer to the system. However, PLLs are inherently nonlinear, noise sensitive and difficult to tune. Extra caution is required when designing PLLs because multiple PLL units can compete with each other and cause complexity, reduced performance and instability [24, 25].

2.4.5 Harmonics

Harmonics are basically the integer multiples of the fundamental frequency of a trigonometric sin or cos signal. Based on fourier analysis, any signal can be

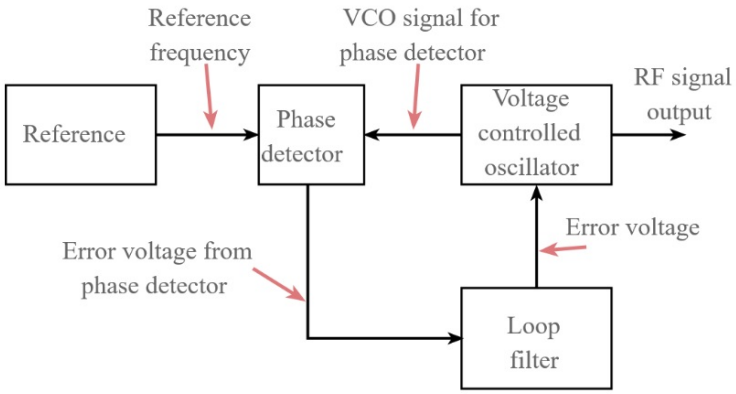

Figure 2.14: PLL unit diagram

expanded to sinusoidal waveforms with different harmonics. In the power systems, harmonics are a result of non-linear loads that draw non-sinusoidal current from a sinusoidal voltage source such as motor drives or converters (which compose a large portion of the grid itself). Harmonics on nature can be extremely dangerous specially in the power grids. They can cause voltage distortion, forced increase in the nominal utility sizing, reduced power factor, equipment malfunction, component overheating, resonance phenomenon and so on. Different grid codes set standards for acceptable ranges of harmonics which are defined as Total harmonic Distortion (THD). According to IEEE standard of 519-1992 the total acceptable THD is from 3.0 % to 10.0 % according to application. THD is defined as below:

$$THD = \frac{\sqrt{V_2^2 + V_3^2 + V_4^2 + ...}}{V_1} \tag{2.23}$$

in which V_n is the RMS value of the nth harmonic.

In power converters, it is inevitable to have THD to some extent. Reason is that the process of transforming voltage from ac to dc and dc to ac in nature is based on switching components which operate with pulses, later on explained in detail. In order to reduce the amount of harmonics injection many methods have been developed thus far. Reactors or chokes, passive and active filters, harmonic cancellation methods with high pulse count rectification and drive isolation transformer are the general methods. In the design of the power converters in this study the filters act an essential role. The main concerns about harmonics in this thesis are about power factor (active power delivered to the loads) and voltage distortion. The design procedure of the filters is explained in chapter 5.

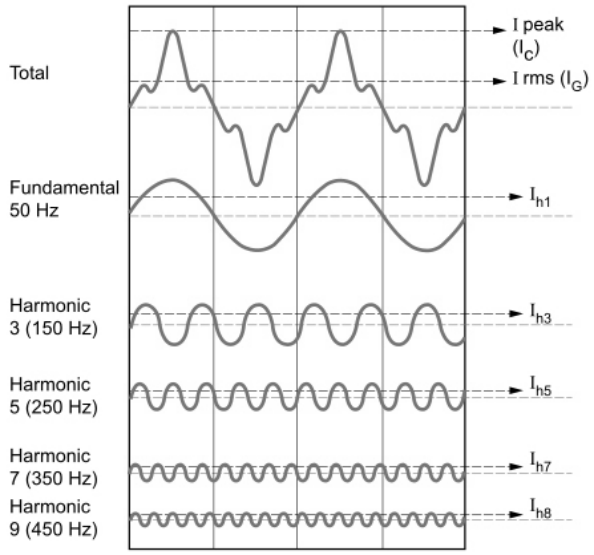

Figure 2.15: harmonics definition and waveform

2.4.6 Vector transformation

The control and analysis of a three phase system can be difficult if one decides to model every components in the abc reference frame. Therefore, vector transformation has been used since long time ago to facilitate the analysis of system components, control systems and so on. Two of such vector transforms are the Park and Clarke transforms.

2.4.6.1 Clarke vector transformation

The Clarke transformation changes three rotating vectors in fixed abc axis into stationary vectors on rotating axis reference frames ($\alpha\beta\gamma$):

$$\begin{bmatrix} V_\alpha \\ V_\beta \\ V_\gamma \end{bmatrix} = \frac{2}{3} \begin{bmatrix} 1 & -\frac{1}{2} & -\frac{1}{2} \\ 0 & \frac{\sqrt{3}}{2} & -\frac{\sqrt{3}}{2} \\ \frac{1}{2} & \frac{1}{2} & \frac{1}{2} \end{bmatrix} \begin{bmatrix} V_a(t) \\ V_b(t) \\ V_c(t) \end{bmatrix} \tag{2.24}$$

And the inverse of the Clarke transformation:

$$\begin{bmatrix} V_a(t) \\ V_b(t) \\ V_c(t) \end{bmatrix} = \begin{bmatrix} 1 & 0 & 1 \\ -\frac{1}{2} & \frac{\sqrt{3}}{2} & 1 \\ -\frac{1}{2} & -\frac{\sqrt{3}}{2} & 1 \end{bmatrix} \begin{bmatrix} V_\alpha \\ V_\beta \\ V_\gamma \end{bmatrix} \tag{2.25}$$

2.4.6.2 Park transformation

The Park transformation, also known as dq0 transformation, rotates the reference frame of the $\alpha\beta$ to an arbitrary frequency.

$$\begin{bmatrix} V_d \\ V_q \\ V_0 \end{bmatrix} = \frac{2}{3} \begin{bmatrix} \cos(\theta) & \sin(\theta) & 0 \\ -\sin(\theta) & \cos(\theta) & 0 \\ 0 & 0 & 1 \end{bmatrix} \begin{bmatrix} V_\alpha \\ V_\beta \\ V_\gamma \end{bmatrix} \tag{2.26}$$

The Clark and Park transformation combined together are the basis of the vector transformation used in the three phase converter control system, called the DQZ reference frame:

$$\begin{bmatrix} V_D \\ V_Q \\ V_Z \end{bmatrix} = \sqrt{\frac{2}{3}} \begin{bmatrix} \cos(\theta) & \cos(\theta - \frac{2\pi}{3}) & \cos(\theta + \frac{2\pi}{3}) \\ -\sin(\theta) & -\sin(\theta - \frac{2\pi}{3}) & -\sin(\theta + \frac{2\pi}{3}) \\ \frac{\sqrt{2}}{2} & \frac{\sqrt{2}}{2} & \frac{\sqrt{2}}{2} \end{bmatrix} \begin{bmatrix} V_a(t) \\ V_b(t) \\ V_c(t) \end{bmatrix} \tag{2.27}$$

And its inverse:

$$\begin{bmatrix} V_a(t) \\ V_b(t) \\ V_c(t) \end{bmatrix} = \sqrt{\frac{2}{3}} \begin{bmatrix} \cos(\theta) & -\sin(\theta) & \frac{\sqrt{2}}{2} \\ \cos(\theta - \frac{2\pi}{3}) & -\sin(\theta - \frac{2\pi}{3}) & \frac{\sqrt{2}}{2} \\ \cos(\theta + \frac{2\pi}{3}) & -\sin(\theta + \frac{2\pi}{3}) & \frac{\sqrt{2}}{2} \end{bmatrix} \begin{bmatrix} V_D \\ V_Q \\ V_Z \end{bmatrix} \tag{2.28}$$

2.4.7 Modulation techniques

The most extended modulation technique for inverters is Pulse Width Modulation (PWM). This technique is relatively easy to implement and can reduce

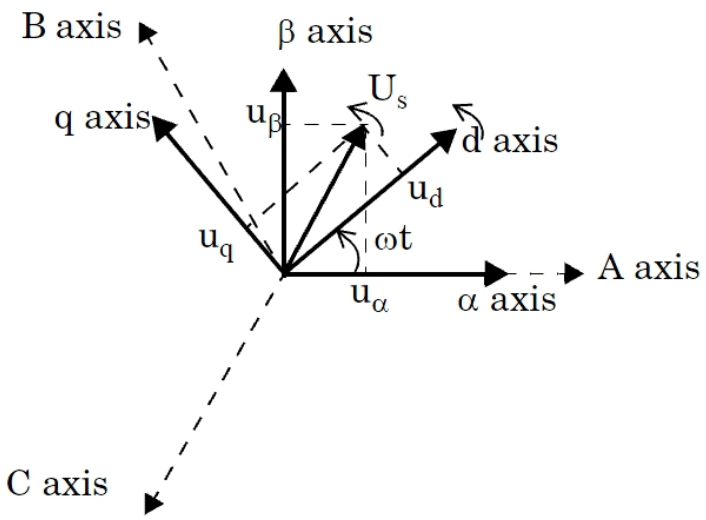

Figure 2.16: abc to $\alpha\beta$ to dq transformation

the low frequency harmonics to some extent. The method operates on the basis of switching at high frequencies and trying to maintain an average value equal to the reference input signal (which is usually sinusoidal). The method works by comparison of a reference signal V_{mod} (modulator) with a high frequency triangular wave V_{car} (carrier) and giving the resultant signal to the gate of the switches. Two of the most common PWM techniques are bipolar and unipolar modulation.

2.4.7.1 Bipolar PWM

Bipolar PWM is commonly used in half bridge and occasionally full bridge converters. In this method, a DC voltage with alternating sign is applied at the output such that an average value at each carrier signal period is achieved. Figure 2.17(a) shows the bipolar technique, in which V_ref is V_{mod} and the triangular waveform V_C is the carrier. The following function is applied to obtain the switching command:

$$S = \begin{cases} 1 & \text{if} \quad V_{mod} \geq V_{car} \\ 0 & \text{if} \quad V_{mod} < V_{car} \end{cases} \tag{2.29}$$

resulting in the output voltage equal to:

$$V_O = \begin{cases} +0.5V_{dc} & \text{if} \quad V_{mod} \geq V_{car} \\ -0.5V_{dc} & \text{if} \quad V_{mod} < V_{car} \end{cases} \tag{2.30}$$

2.4.7.2 Unipolar PWM

Unipolar PWM is only used in full bridge converters because it requires application of zero output voltage. In this method, the output voltage alternates between $+V_{dc}$ and 0 during positive cycle of the modulator, while alternating between $-V_{dc}$ and 0 during negative cycle of the modulator. Figure 2.17(b) shows the unipolar technique, in which V^* is V_{mod} and the triangular waveform is the carrier. The following equations demonstrate this method:

- Case one ($V_{mod} > 0$):

$$S_1 = \begin{cases} 1 & \text{if} \quad V_{mod} \geq V_{car} \\ 0 & \text{if} \quad V_{mod} < V_{car} \end{cases} \tag{2.31}$$

$$S_2 = 0 \tag{2.32}$$

Then the output voltage would be:

$$V_O = \begin{cases} +V_{dc} & \text{if} \quad V_{mod} \geq V_{car} \\ 0 & \text{if} \quad V_{mod} < V_{car} \end{cases} \tag{2.33}$$

- Case two ($V_{mod} < 0$):

$$S_1 = 0 \tag{2.34}$$

$$S_2 = \begin{cases} 1 & \text{if} \quad V_{mod} \geq V_{car} \\ 0 & \text{if} \quad V_{mod} < V_{car} \end{cases} \tag{2.35}$$

Then the output voltage would be:

$$V_O = \begin{cases} 0 & \text{if} \quad V_{mod} \geq V_{car} \\ -V_{dc} & \text{if} \quad V_{mod} < V_{car} \end{cases} \tag{2.36}$$

For a correct modulation the following conditions must be at place:

$$m_a < 1 \tag{2.37}$$

$$m_f \ll 1 \tag{2.38}$$

in which m_a and m_f are amplitude and frequency modulation indexes and are define as:

$$m_a = \frac{V_{mod_{max}}}{V_{car_{max}}} \tag{2.39}$$

$$m_f = \frac{f_{car}}{f_{mod}} \tag{2.40}$$

$$\tag{2.41}$$

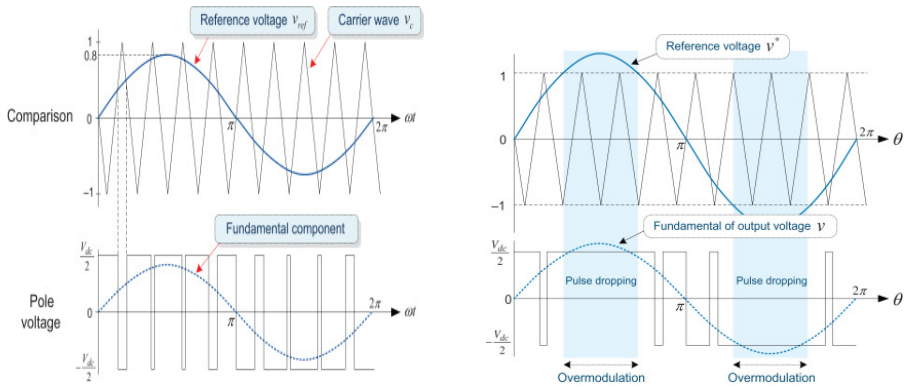

(a) **(b)**

Figure 2.17: (a) Bipolar, (b) Unipolar PWM

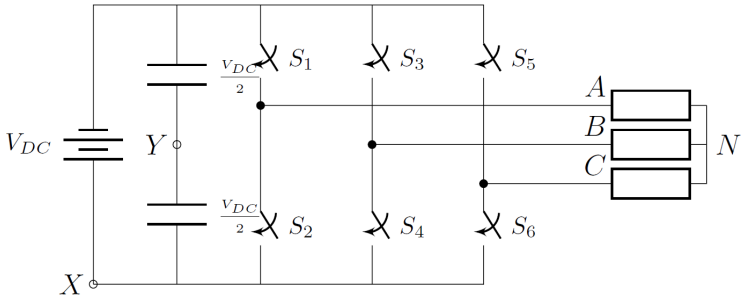

Figure 2.18: Three phase inverter with switching states

In case of bipolar modulation if m_f is an odd integer, then the output voltage will have an even symmetry. On the other hand, in unipolar modulation m_f is an even integer so that most of the harmonics present in bipolar modulation are canceled in unipolar. In this project, SVPWM is used and its basics are explained in the next subsection. The detials of the modulation technique is crucial for understanding the operation of the switches developed later on in the project.

2.4.7.3 Space Vector Pulse Width Modulation (SVPWM)

In the three phase inverters the SVPWM method is widely used which is on the basis of the explained PWM methods. This method, in high frequencies gives out almost sinusoidal voltages at the point of connection. Figure 2.18 illustrates a three phase inverter. Each switch pair has a switching function, resulting in 8 possible scenarios. These functions are presented in Equation 2.42 to 2.44 .

$$S_A = \begin{cases} 1 & \text{if } S_1 \text{ closed, } S_2 \text{ open} \\ 0 & \text{if } S_1 \text{ open, } S_2 \text{ closed} \end{cases} \tag{2.42}$$

$$S_B = \begin{cases} 1 & \text{if } S_3 \text{ closed, } S_4 \text{ open} \\ 0 & \text{if } S_3 \text{ open, } S_4 \text{ closed} \end{cases} \tag{2.43}$$

$$S_C = \begin{cases} 1 & \text{if } S_5 \text{ closed, } S_6 \text{ open} \\ 0 & \text{if } S_5 \text{ open, } S_6 \text{ closed} \end{cases} \tag{2.44}$$

Considering the switching functions, the operation of this circuit generates three phase to phase and phase to neutral output voltage magnitudes as in Equation 2.45 to 2.50.

$$V_{AB} = (S_A - S_B) \cdot V_{DC} \tag{2.45}$$
$$V_{BC} = (S_B - S_C) \cdot V_{DC} \tag{2.46}$$
$$V_{CA} = (S_C - S_A) \cdot V_{DC} \tag{2.47}$$

$$V_{AN} = (\frac{2}{3}S_A - \frac{1}{3}S_B - \frac{1}{3}S_C) \cdot V_{DC} \tag{2.48}$$
$$V_{BN} = (\frac{-1}{3}S_A - \frac{2}{3}S_B - \frac{1}{3}S_C) \cdot V_{DC} \tag{2.49}$$
$$V_{CN} = (\frac{-1}{3}S_A - \frac{1}{3}S_B + \frac{2}{3}S_C) \cdot V_{DC} \tag{2.50}$$

According to this terminology, the voltages are calculated from the dc input as shown in table 2.1 and 2.2. V_{LL0} to V_{LL7} are called voltage vectors. These vectros are shown on $\alpha - \beta$ plane as in figure 2.19.

From the 8 possible switching states, first and last one are evidently not practical to produce voltage and the rest are used (Those two can be used for adding dead time to the switching pattern). The six sections between each V_{LL} vector (forming a circle) is a possible location for the output voltage vector of the inverter (Although due to the nature of averaging, the actual area is a hexagon). The voltage synthesizing can be implemented by a triangular wave as trigger, assuming that the desired voltage reference is available (from the control system and after vector transformation).

The strategy is as followed: First determine the desired voltage vector is in which one of the six sectors, in order to understand which voltage vectors (meaning switches) need to be utilized. Then the weight (amplitude) of each vector can be found via the desired voltage magnitude and the prior knowledge of the DC link voltage. These weights are exactly the time that the corresponding switch

Table 2.1: Switching states and line voltages

S_A, S_B, S_C	V_{AB}	V_{BC}	V_{CA}	V_{LL}
000	0	0	0	$\overrightarrow{V}_{LL0} = \vec{0}$
100	V_{DC}	0	-V_{DC}	$\overrightarrow{V}_{LL1} = \sqrt{2}V_{DC}e^{j\frac{\pi}{6}}$
110	0	V_{DC}	-V_{DC}	$\overrightarrow{V}_{LL2} = \sqrt{2}V_{DC}e^{j\frac{3\pi}{6}}$
010	-V_{DC}	V_{DC}	0	$\overrightarrow{V}_{LL3} = \sqrt{2}V_{DC}e^{j\frac{5\pi}{6}}$
011	-V_{DC}	0	V_{DC}	$\overrightarrow{V}_{LL4} = \sqrt{2}V_{DC}e^{j\frac{7\pi}{6}}$
001	0	-V_{DC}	V_{DC}	$\overrightarrow{V}_{LL5} = \sqrt{2}V_{DC}e^{j\frac{9\pi}{6}}$
101	V_{DC}	-V_{DC}	0	$\overrightarrow{V}_{LL6} = \sqrt{2}V_{DC}e^{j\frac{11\pi}{6}}$
111	0	0	0	$\overrightarrow{V}_{LL7} = \vec{0}$

Table 2.2: Switching states and phase voltages

S_A, S_B, S_C	V_{AN}	V_{BN}	V_{CN}	V_{LL}
000	0	0	0	$\overrightarrow{V}_{LL0} = \vec{0}$
100	2/3 V_{DC}	-1/3 V_{DC}	-1/3 V_{DC}	$\overrightarrow{V}_{LL1} = \sqrt{\frac{2}{3}}V_{DC}e^{j0}$
110	1/3 V_{DC}	1/3 V_{DC}	-2/3 V_{DC}	$\overrightarrow{V}_{LL2} = \sqrt{\frac{2}{3}}V_{DC}e^{j\frac{1\pi}{3}}$
010	-1/3 V_{DC}	2/3 V_{DC}	-1/3 V_{DC}	$\overrightarrow{V}_{LL3} = \sqrt{\frac{2}{3}}V_{DC}e^{j\frac{2\pi}{3}}$
011	-2/3 V_{DC}	1/3 V_{DC}	1/3 V_{DC}	$\overrightarrow{V}_{LL4} = \sqrt{\frac{2}{3}}V_{DC}e^{j\frac{3\pi}{3}}$
001	-1/3 V_{DC}	-1/3 V_{DC}	2/3 V_{DC}	$\overrightarrow{V}_{LL5} = \sqrt{\frac{2}{3}}V_{DC}e^{j\frac{4\pi}{3}}$
101	2/3 V_{DC}	-2/3 V_{DC}	1/3 V_{DC}	$\overrightarrow{V}_{LL6} = \sqrt{\frac{2}{3}}V_{DC}e^{j\frac{5\pi}{3}}$
111	0	0	0	$\overrightarrow{V}_{LL7} = \vec{0}$

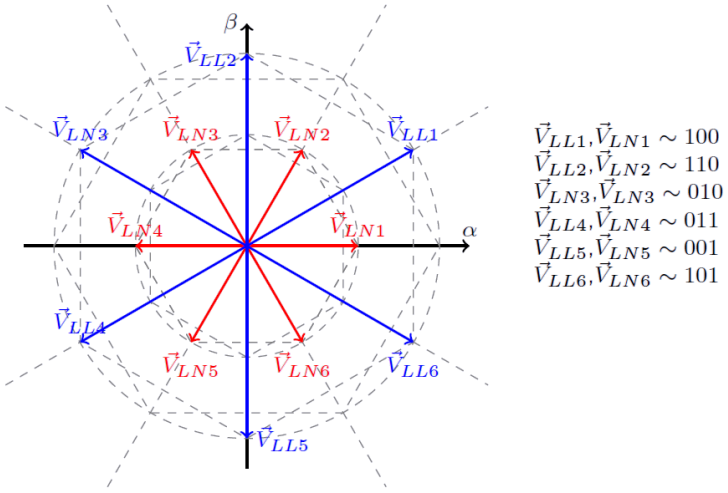

Figure 2.19: Graphical representation of the voltage vectors in each state

must be left turned on in each period ($T = \frac{1}{f_{sw}}$). As an example, consider that the control system generates a modulating signal of $V_{ref}\angle\alpha$ and α drops in the first section between V_{LL1} and V_{LL}. Therefore, projecting V_{ref} on these vectors:

$$V_{ref}\angle\alpha = (\tau_1 \times f_{sw}) \cdot V_{LL1} + (\tau_3 \times f_{sw}) \cdot V_{LL3} \tag{2.51}$$

τ_1 and τ_3 can be found accordingly.

The maximum obtainable voltage on the output happens when the resultant voltage vector (from the summation of the two vectors on boundaries of the selected section with the calculated weight amplitude) is placed exactly in the middle of the section with an angle of 30 degrees. Accordingly the voltage magnitude will be:

$$V_{LL,max_{RMS}} = V_{DC} \times \cos 30^\circ \times \frac{1}{\sqrt{2}} \tag{2.52}$$

The value of the output voltage is lower than the desired voltage (that was given as modulation signal). This happens because when adding the weighted voltage vectors, signals are averaged and in the process some of the voltage is diminished. Another problem with SVPWM is physical limitations, which limits the voltage and current drawn from the inverter. This issue can be tackled by injecting third harmonic before the PWM to the modulation signal. Although the third harmonic has to be canceled before entering the grid with a transformer.

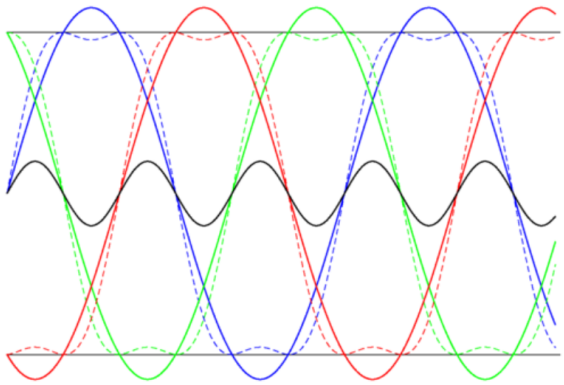

Figure 2.20: Third harmonic injection (dotted lines are the resultant signals)

2.4.7.4 Third harmonic injection

As mentioned, other than the lowered voltage due to the averaging, the limitations of design of components sets an even lower margin for the voltage output. To mediate this issue the third harmonic injection strategy is used. Third harmonic injection happens right before injecting the voltage reference modulator signal generated from the control system. Basically, the strategy involves adding another sine wave with three time the desired frequency. This also does not interfere with possible motors in the model, since the motors are grounded with a neutral point which oscillates with three times the fundamental frequency and therefore the motor will not be affected.

The third harmonic injection is used in this project and it is generated from equation 2.53. Figure 2.20 shows the effect of third harmonic injection. The peak of the signal will be reduced and limited.

$$V_{3f} = \frac{Max(V_f) - Min(V_f)}{2} \tag{2.53}$$

$$V_{mod} = V_f - V_{3f} \tag{2.54}$$

Next chapter provides a thorough examination of developed methods to provide virtual inertia and their control algorithms while highlighting their advantages and disadvantages.

Chapter 3

Existing Literature for Methods to Emulate Virtual Inertia

3.1 Introduction

One pf the most common control methods of wind turbines is maximising the output power generated. These control methods need to be designed with caution in order to prevent any instability issues in the system. With the aim of large integration of RES into the electricity grid, certain adaptations are essential in order to avoid stability issues. One of these issues as introduced in the previous chapter, arises from the concept of inertia of the system or more specifically, reduction of the inertia.

Multiple methods are introduced in the literature to emulate virtual inertia for generators. Before the advancements of the power electronic technology, reserved SG units at partial loads injected the kinetic energy in their rotating mass to the grid [10] (in case of power deficit in the system) or as condenser units drew energy from the grid (in case of power excess in the system) [26]. However, this method proved to be costly inefficient and impose high capital and operation costs on the grid operator [3]. Soon after expansion of the ESS technologies it was proposed that a solution to the power imbalances in the grid could be the spread of the ESSs in the grid in forms of battery, hydrogen storages and flywheels [27–29]. Nevertheless, the idea was not commercialised yet and similar to the reserved SG units, it was not the most convenient solution. Moreover, other disadvantages such as limit life-cycle,safety and noise, limited space and low round trip-efficiency of this technology was another downturn for industrial application at that time.

While the ESS cost has decreased in the recent years, subsequently with the advancements in the power electronic technology, new solutions emerged and currently, the state of the art methods to provide virtual inertia, incorporate a set of these solutions together. Some methods present a sophisticated modeling of the exact inertial response of the SGs while others provide less accurate models

with faster and simpler implementations. Figure 3.1 provides a set of different methods to provide virtual inertia. These methods operate on different principles such as modeling the exact behavior of SGs, simulating frequency-power response, swing equation. While most of these methods circulate on the basis of modeling SGs, some tend to model other rotating masses such as induction machines. This chapter investigates the various methods to provide virtual inertia for the grid.

Another categorization for the methods to provide virtual inertia was provided by Cheema [30] and based on the need for an external storage unit and details of modeling. This categorization is presented in figure 3.2.

3.2 SG Model Based Methods

3.2.1 Synchronverters

Synchronverters model the exact behaviour of the SGs from the grid point of view with heavy numerical calculations. Synchronverters are voltage sourced grid following converters and benefit from the inherent synchronisation mechanism. Although the initial synchronverter models required a dedicated synchronisation unit, such as PLLs to provide the phase and frequency of the grid voltage, the improved versions are completely self-synchronised [31].

A synchronverter consists of two parts, first part is the power part which includes all the components in the link between dc and ac side, and the second part is the electric part which includes control, sensing and protection circuits. Figure 3.3 and 3.4 present the control models developed by Zhong [24]. In figure 3.3, D_p, $1/Js$, $1/s$ and the blue highlighted block represent the Virtual Synchronous Motor (VSM) and implements the torque, active and reactive power calculations of a SG (similar but not identical to equations 2.19, 2.20 and 2.22 for a DFIG in section 2.3.3) and additionally, generates the signal for converter modulation (this signal would be the same as the voltage at the terminal of the virtual SG). J is the generator moment of inertia, T_e is electromagnetic torque (T_{em}), m_f magnitude of the mutual inductance between stator and field coils, θ is the angle between rotor axis and stator winding phase, e, P, Q are no-load generated voltage, reactive and active output powers, respectively. The emf (e) calculated form the VSM equations enters a PWM block to produce the driving signals for the converter. The output current of the converter that flows into the inductors are considered as stator current (i) and fed back to the VSM model. Meanwhile, the frequency and voltage must be regulated via controlling the active and reactive power, respectively. The proposed topology satisfies these conditions as the mechanical friction coefficient (D_p) can play the role of frequency droop coefficient, eliminating the need for an additional control loop by regulating the frequency/speed ($\dot{\theta}$) of the synchronverter and generating the phase angle θ for the emf. The field excitation

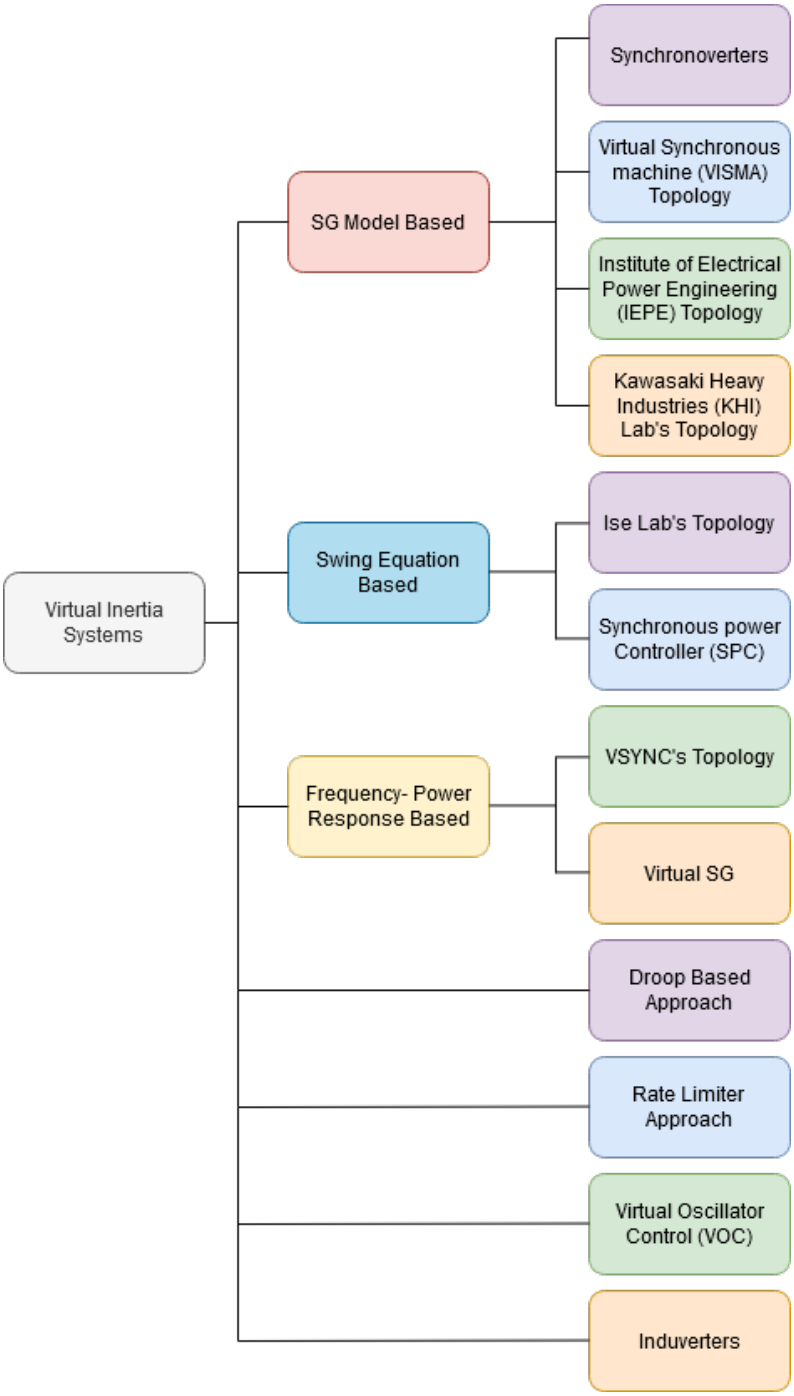

Figure 3.1: Methods to provide virtual inertia

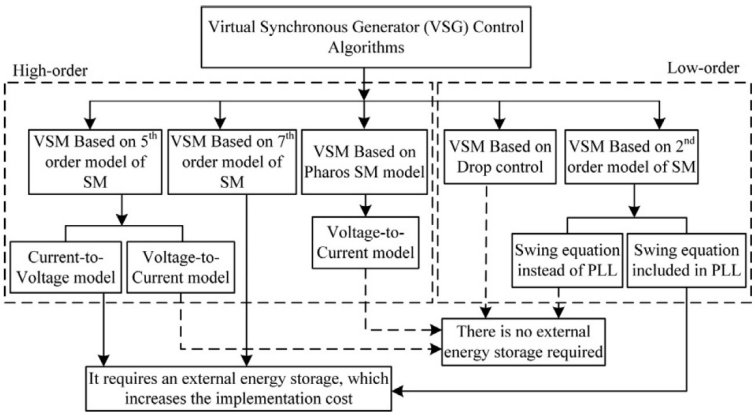

Figure 3.2: Methods to provide virtual inertia [30]

current $M_f.i_f$ is generated from the reactive power and a voltage droop control is added that controls the voltage with the voltage droop coefficient D_q. Satisfying all the conditions of the normal operation, the PLL is added to synchronise the converters with the grid before connection.

The upgraded version as shown in figure 3.4 removes the PLL and virtual current (i_s) is generated from the voltage difference of e and V_g and the current injected to the VSM can be either grid current (i_g) or i_s. Additionally, a PI controller regulates the output ΔT to be zero and generates the reference frequency $\dot{\theta}$ for the synchronverter. Moreover, the addition of the switches S_c, S_P and S_Q enables different modes of operation for the controller. S_C in position 1 while S_Q is off and S_P is on, allows the reference real and reactive power to be sent to the grid. If active and reactive power references (P_{set}, Q_{set}) are zero simultaneously, the synchronverter is self-synchronised. If i_s is zero, the voltage is synced. If S_C is set to position 2, other modes of operation are enabled. After the connection has been made, if S_P is in ON state, ΔT will be set zero by the PI controller. As a result, electromagnetic and mechanical torques will be equal and $P = P_{set}$. This mode is named the *set mode*. Active and reactive power have their own set modes called the P and Q mode. If S_P is OFF, the PI controller is bypassed and synchronverter is in frequency droop mode, called P_D mode. Correspondingly, the voltage droop mode is Q_D mode. Table 3.1 provides all the operational modes of the self-synchronised synchronverter.

The advantage of this model is the fact that the controller implements the exact natural inertial response of a SG during a contingency event. Additionally, the Voltage source implementation of this topology saves the topology from the grid transient currents, not to mention that this can be used as a grid forming unit to emulate virtual inertia. Moreover, the synchronverter technology is not dependant on the parameters of the wind turbine generator itself. Nevertheless,

Table 3.1: The operation modes of the self-synchronised synchronverter

Switch S_C	Switch S_P	Switch S_Q	Mode
1	ON	ON	N/A
1	ON	OFF	Self-synced
1	OFF	ON	N/A
1	OFF	OFF	N/A
2	ON	ON	P mode, Q_D mode
2	ON	OFF	P mode, Q mode
2	OFF	ON	P_D mode, Q_D mode
2	OFF	OFF	P_D mode, Q mode

the complexity of the model and numerical calculations is a disadvantage for this model.

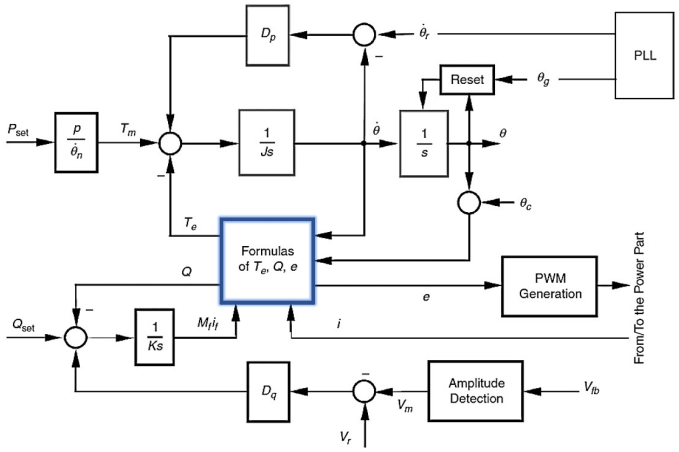

Figure 3.3: Synchronverter control model

3.2.2 Institute of Electrical Power Engineering (IEPE) Lab Topology

The Institute of Electrical Power Engineering (IEPE) lab topology named Virtual Synchronous Machine (VISMA), was introduced by Hesse [32] in 2009 and developed further on 2011 [33]. Figure 3.5 illustrates this model in general format. Similar to synchronverters, the model represents a SG while a notable difference between the two models is current source based topology of the VISMA, unlike synchronverter. A current source based converter essentially has the disadvantage of injecting current harmonics and unbalances of the grid into the control system. In order to alleviate these disturbances, a wideband compensation method is used. Figures 3.5 and 3.6 illustrate the VISMA model and its detailed subsystems in sequence. This topology, although more complex, has no evident advantages over the synchronverter topology.

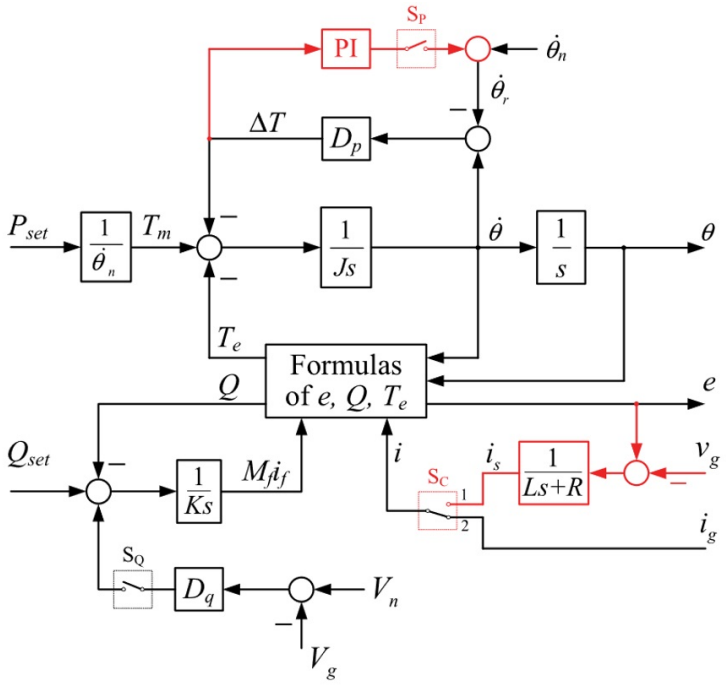

Figure 3.4: Self-synchronised synchronverter model

The compensation method is implemented by a Digital Signal Processing (DSP) unit and a hysteresis controller. First the PLL unit generates a normalized 2π angle ramp synced with the first phase of the grid. The integrated sum of the center frequency and controller results in an angle ramp. A modulo limiter is considered to avoid overflow. Due to the ramp shape of the signal, a sine function is required in the feedback signal for comparison. The resulting synced ramp signal then passes the phase generation subsystem to build the desired phase voltages of the grid. The amplitude of the voltage is then formed in the amplitude generation subsystem. Then the noise component is removed by subtracting the measured phase voltages and the synthesized values. The noise component is inverted and weighted with the Distortion Component factor (DCF) and in the end, fed to the hysteresis controller. This method is quite known in the noise cancellation methods and the imperative condition of correct operation of the method is a fast acting hysteresis controller.

The updated control model (IEPE lab topology) that produces the reference current signal for the hysteresis block is presented in figure 3.7. The control system in this topology is quite similar to the synchronverter topology. In this model, the output of the power output of the converter can be controlled by adjusting the value of mechanical power and the electromotive force (*emf*) sets the grid voltage. The upgraded model is more flexible since the inertia constant and the

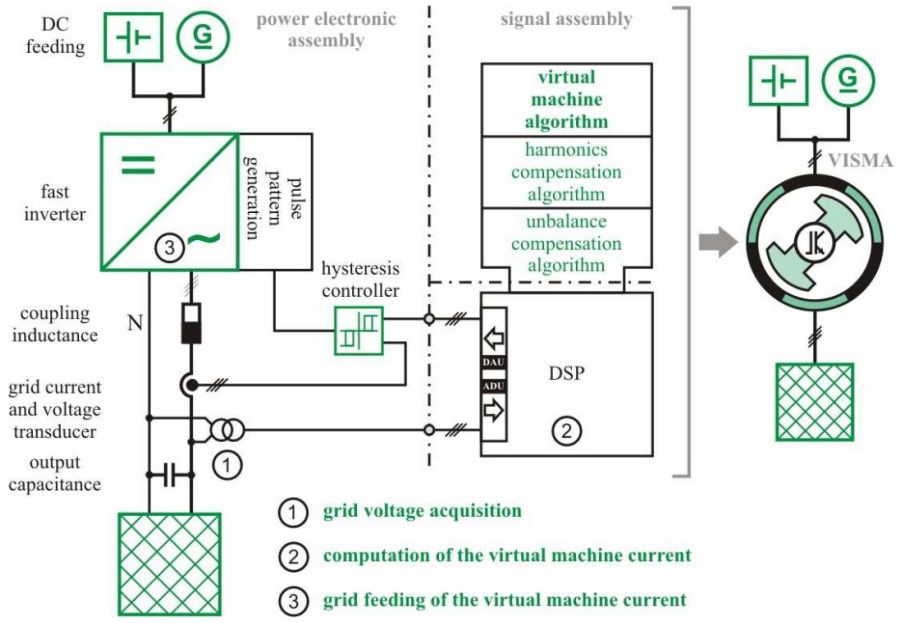

Figure 3.5: VISMA model

damping force can be adjusted easily in the SG model. In this model, the grid current is measured and the voltage reference value is calculated from the stator circuit analysis:

$$e_1 - u_1 = i_1 \cdot R_s + L_s \cdot \frac{di_1}{dt} \tag{3.1}$$

$$e_2 - u_2 = i_2 \cdot R_s + L_s \cdot \frac{di_2}{dt} \tag{3.2}$$

$$e_3 - u_3 = i_3 \cdot R_s + L_s \cdot \frac{di_3}{dt} \tag{3.3}$$

$$\vec{e} - \vec{u}_{grid} = \vec{i}_{ref} \cdot R_s + L_s \cdot \frac{d\vec{i}_{ref}}{dt} \tag{3.4}$$

where $\vec{e} = \begin{bmatrix} e_1 \; e_2 \; e_3 \end{bmatrix}^T$ is the induced emf in the stator winding, $\vec{u}_{grid} = \begin{bmatrix} u_1 \; u_2 \; u_3 \end{bmatrix}^T$ is the grid voltages at the Point of Common Coupling (PCC), R_s and L_s are the stator resistance and inductance respectively. Then the reference current can be calculated as:

$$\vec{i}_{ref}(s) = (\vec{e}(s) - \vec{u}_{grid}(s))/(R_s + L_s \cdot s) \tag{3.5}$$

Finally, the interaction between rotor and stator can be modeled by the electromechanical power balance equation:

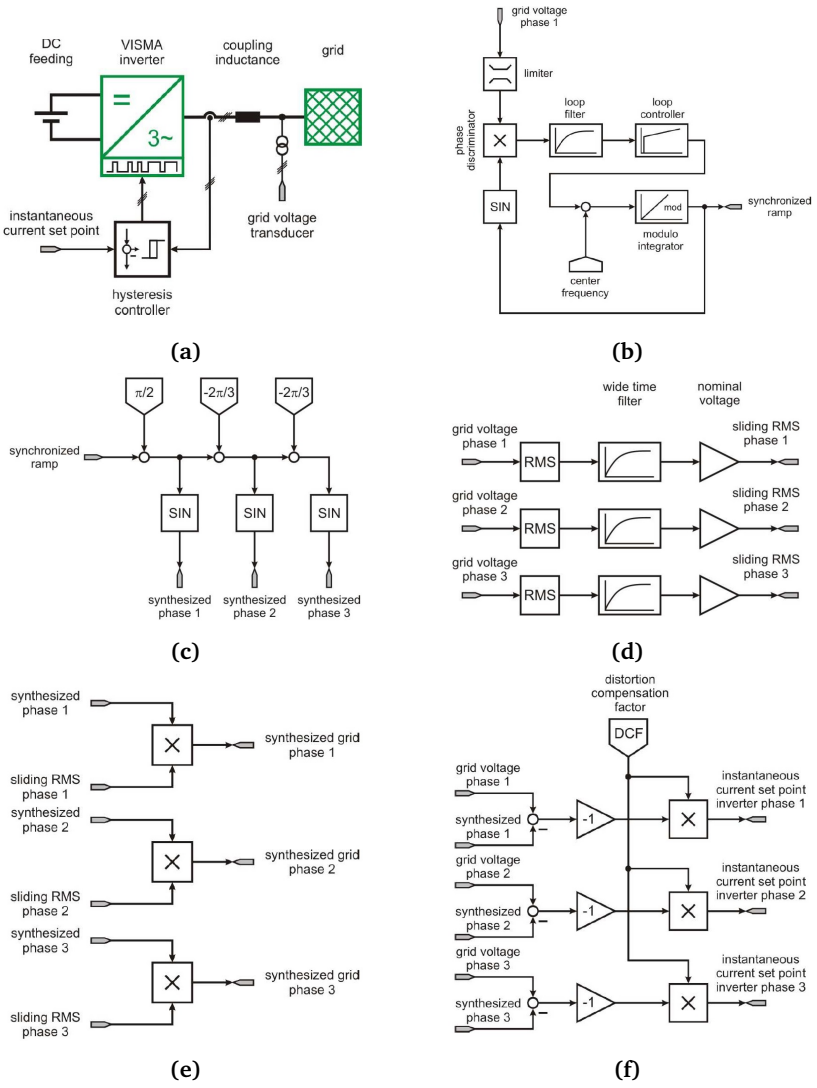

Figure 3.6: VISMA (a) hysteresis controller, (b) PLL, (c) phase generation, (d) amplitude generation, (e) grid synthesizing, (f) Distortion compensation subsystems

$$T_m - T_e = \frac{1}{J} \cdot \frac{d\omega}{dt} + k_d \cdot f(s) \cdot \frac{d\omega}{dt} \tag{3.6}$$

$$T_e = \frac{P_e}{\omega} \tag{3.7}$$

$$\theta = \int \omega \cdot dt \tag{3.8}$$

in which, J is the moment of inertia, k_d is the mechanical damping factor, $f(s)$ is the phase compensation function, ω is the angular speed of rotation, θ is the angular position of the rotor, T_e and T_m are the electrical and mechanical torque. The phase compensation term guarantees that damping force counteracts the possible oscillations of the rotor in the opposite phase. As mentioned previously, the induced *emf* can be adjusted and set to grid voltage:

$$\vec{e} = \begin{bmatrix} e_1 \\ e_2 \\ e_3 \end{bmatrix} = E_p \cdot \begin{bmatrix} \sin\theta \\ \sin\theta - \frac{2}{3} \cdot \pi \\ \sin\theta + \frac{2}{3} \cdot \pi \end{bmatrix} \tag{3.9}$$

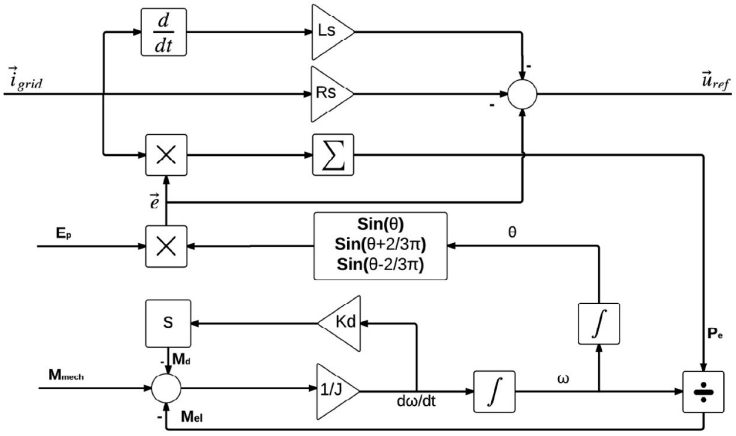

Figure 3.7: Updated IEPE Controller topology for SG

3.2.3 Kawasaki Heavy Industries (KHI) Lab's Topology

The Kawasaki Heavy Industries (KHI) topology is a Virtual Synchronous Generator (VSG) model that works on the basis of phasor diagrams of the SGs [34]. In this model the entire SG is not implemented and instead the equivalent Automatic Voltage Regulator (AVR) and governor are modeling the dynamics of the SG [35].

Figure 3.8 depicts the KHI topology [30]. The model is a current controlled based converter in *d-q* axis coordinates. The *d* axis is placed along the phase voltage of the generator and the *q* axis leads by 90°. E_F, V_g, V_d, V_q denote the internal *emf* and terminal voltage of the generator and the *d,q* axis voltages , respectively. Additionally, θ, x, r are the phase angle, reactance of the generator and armature resistance. The armature current in the *d-q* axis can be then calculated from the following equations:

$$\begin{bmatrix} I_d^* \\ I_q^* \end{bmatrix} = Y\left(\begin{bmatrix} E_d - E_q \end{bmatrix} - \begin{bmatrix} V_d V_q \end{bmatrix}\right) \tag{3.10}$$

$$Y = \frac{1}{r^2 + x^2}\begin{bmatrix} r & x \\ -x & r \end{bmatrix} = \begin{bmatrix} Y_{dd} & Y_{dq} \\ -Y_{dq} & Y_{dd} \end{bmatrix} \tag{3.11}$$

$$\begin{bmatrix} E_d \\ E_q \end{bmatrix} = \mid E_f \mid \begin{bmatrix} \cos\theta \\ \sin\theta \end{bmatrix} \tag{3.12}$$

This model consists of both governer and AVR and utilises a PLL unit for synchronisation, explained:

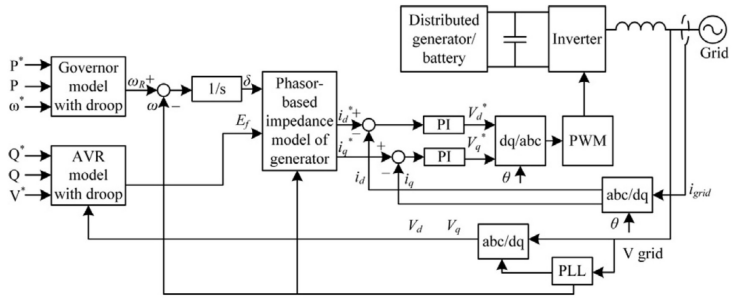

Figure 3.8: KHI SG topology

- Governer Model
  The governer model shown in figure 3.10 determines the angular speed of the rotor. The required angular speed ω_R is found by finding difference between the active power reference and its actual value. A first order delay is used and the rated angular speed is compared with the output of the delay subsystem.

- AVR Model
  A quadrature-current compensation is used for determining the internal *emf* as figure 3.10 illustrates. In real generators, the AVR and time constant of the field winding determine the gain of the voltage feedback. The proportional integral used does not have any phase delays or gain drops in the high frequencies.

- PLL Model
  The PLL used in this topology is presented in figure 3.10 and variables θ and ω denote the angle and angular velocity of the rotor. The error between ω and θ is find via the following equation:

$$\frac{2}{3}\sum_{n=0,1,2}\sin(\varphi - n\pi/3)\cos(\theta - n\pi/3) = \sin(\varphi-\theta) \simeq (\varphi-\theta) \quad if \quad |\varphi-\theta| \ll 1 \tag{3.13}$$

  As the equation shows, the angular error is the inner product of the output voltage of the inverter for each phase divided by peak values and a three phase vector with a phase lead of $\pi/2$. The angular error only occurs on the d-axis voltage component. Figure 3.9 presents this fact.

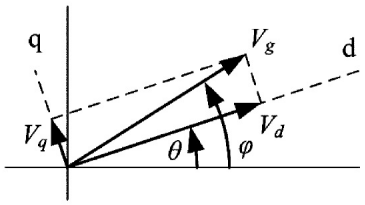

Figure 3.9: Angular deviation in the KHI PLL

The angular velocity ω can be find via the angular error:

$$\varphi - \theta \simeq V_q/V_g \tag{3.14}$$

$$\omega = (K_{PP} + \frac{K_{PI}}{s})\frac{V_q}{V_g} \tag{3.15}$$

3.3 Swing Equation Based Methods

3.3.1 Ise Lab's Topology

Ise topology utilises the swing equation 2.10 as the heart of the VSG model and was developed by the Ise Lab [18]. In each cycle, the swing equation is solved in VSG control block and the frequency ω is calculated as shown in figure 3.11. Then it is passed to an integrator to produce the phase angle, θ to feed the PWM generator[36]. The complexity of this model is quite less than models operating on the basis of modeling SG.

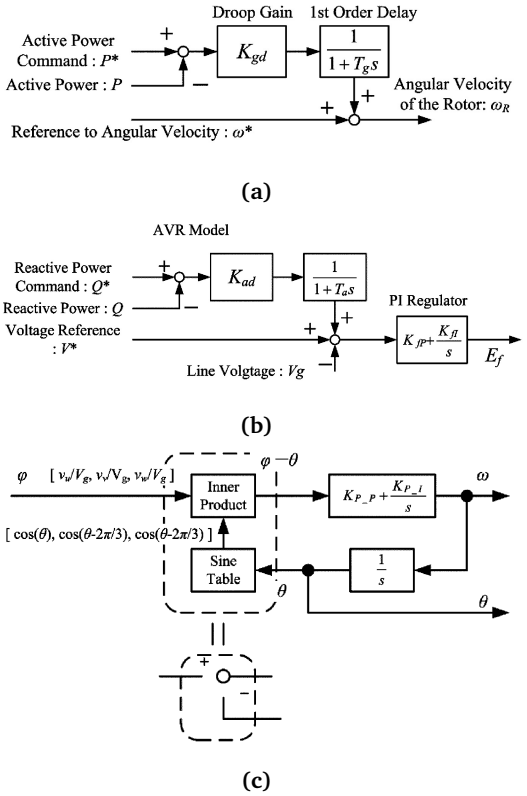

Figure 3.10: KHI topology (a) Governer, (b) AVR and (c) PLL circuits

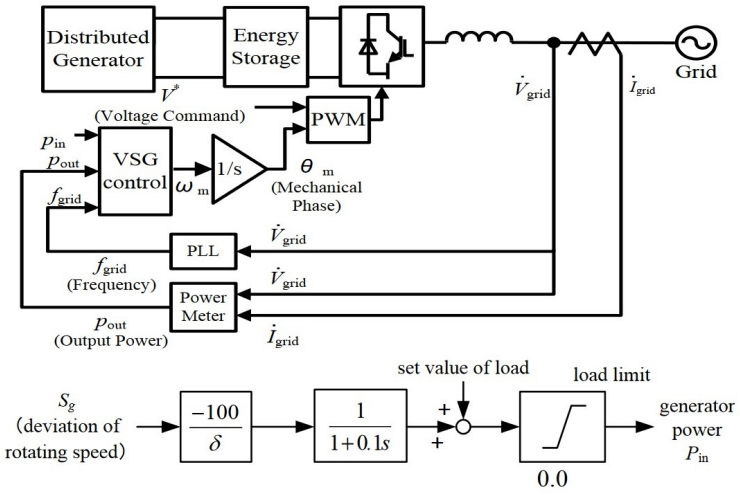

Figure 3.11: Ise topology

3.3.2 Synchronous Power Controller (SPC) Topology

Another swing equation based model is the Synchronous power Controller (SPC) model, developed by Rodriguez [37] for the control of PV generation systems. In this model, the converter is implemented as a cascaded control system. The model has a second order transfer function as shown in figure 3.12 to improve the damping and increase inertia of the system simultaneously. This method models the electrical admittance of the VSG enabling the control of the system without the need for additional filter. On the other hand, this robustness of the controller comes with the price of more difficulty in tuning the controller.

As mentioned, this model does not aim to mimic the behaviour of the SG but it models a second order overdamped response that in case of perturbations provides the satisfactory damping. The electromechanical transfer function of the SPC is developed as below:

$$\frac{P_{elec}}{P_{inp}} = \frac{\frac{P_{Max}}{J \cdot \omega_s}}{s^2 + \frac{k}{J \cdot \omega_s} s + \frac{P_{Max}}{J \cdot \omega_s}} \tag{3.16}$$

where $P_{Max}, P_{elec}, P_{inp}, J, k$ and ω_s represent the maximum value of the active power delivered to the SG, the actual delivered power, the input power, the inertia, the damping factor and the synchronous frequency of the generator respectively.

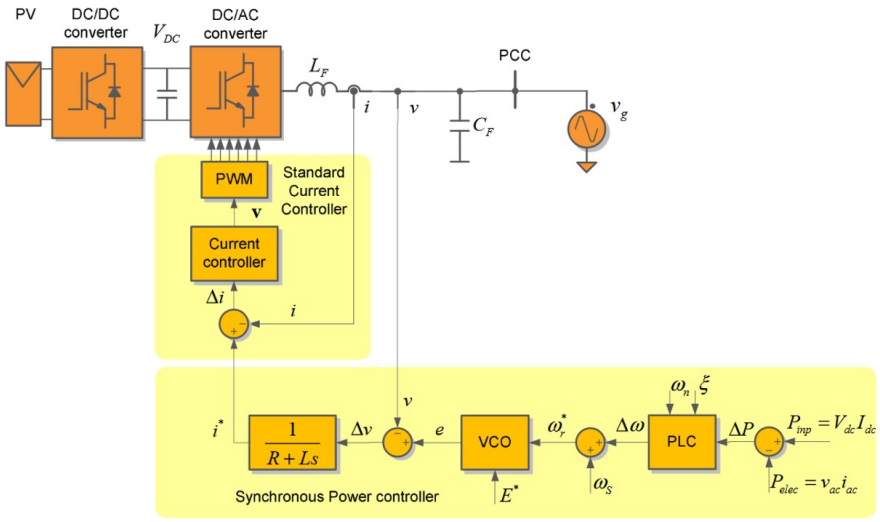

Figure 3.12: SPC topology

3.4 Frequency Power Based Methods

3.4.1 VSYNC Topology

The VSYNC research group introduced a topology that comprised a VSG model, an energy storage unit as source of power and an LCL grid filter [38]. The Eigen-frequency of the filter is positioned about halfway between the nominal power frequency and converter switching frequency. This model is current based and current reference is provided by the PLL circuit. Note that in this model, the PLL is not used as a synchronisation unit but rather as a tool to provide the current reference. The current reference is then used to drive the controller.

Figure 3.13 presents the VSYNC model and its current control block. The current reference block produces the error current signal (i_{dq}). K_{SOC} is assigned in such way that when the change in the State of Charge (SOC) of the ESS is at its maximum. the active signal (P) would be equal to the nominal VSG output power. Additionally, K_v is set accordingly to achieve the maximum reactive power output from the VSG for a specific voltage deviation. The frequency is estimated based on the zero-crossing methodand the set point for current is calculated from the following equation:

$$I_{sp} = \frac{K_I \frac{d\Delta\omega}{dt} + K_P \Delta\omega}{V_{DC}} \tag{3.17}$$

where $\frac{d\Delta\omega}{dt}$ is the ROCOF, K_P is expressed in kgm^2/s^2 and K_I is a dimensionless factor.

3.4.2 Virtual SG

Virtual SG was developed on the basis of modeling the frequency and power response [39] of a SG. The model is quite similar to the VSYNC topology. However, a dynamic frequency regulation is provided, enabling dispatch of the SG. The dynamics of the system can be presented as:

$$P_{SVG} = K_D \Delta\omega + K_I \frac{d\Delta\omega}{dt} \tag{3.18}$$

where P_{SVG} is the output power, K_D and K_I are the damping and inertial constants, respectively. The damping constant is similar to frequency droop, helping to reduce the frequency nadir, while the inertial constant provides fast dynamic frequency based on changes in the frequency. This characteristic is specially useful in the islanded microgrids where ROCOF can be extremely high. As shown in figure 3.14, the PLL measures the changes in the frequency and ROCOF. Then the active power is calculated using Eq. 3.18 and the current reference of of the controller is given by Eq. 3.19 and finally, the current controller produces the signals for the PWM generator.

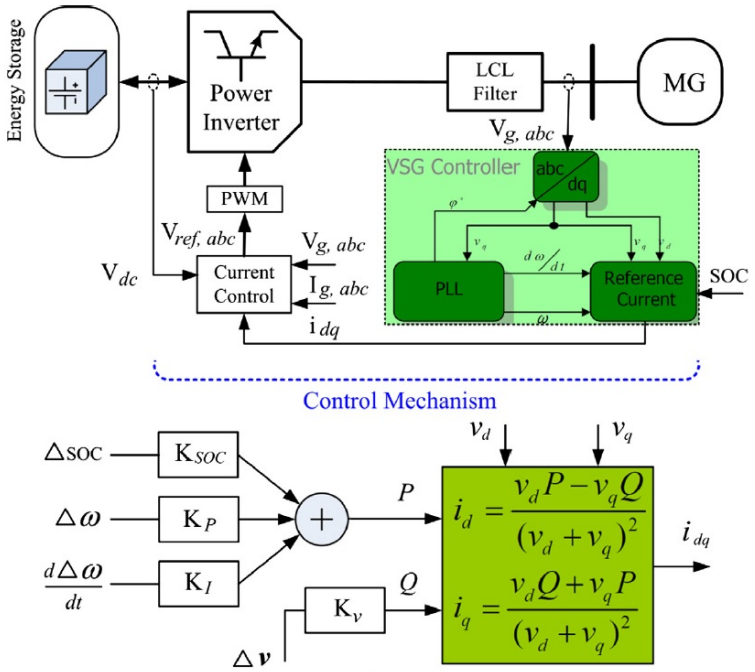

Figure 3.13: VSYNC topology and its reference current block

$$I_d^* = \frac{2}{3}\frac{V_d P_S V G - V_q Q}{V_d^2 + V_q^2} \tag{3.19}$$

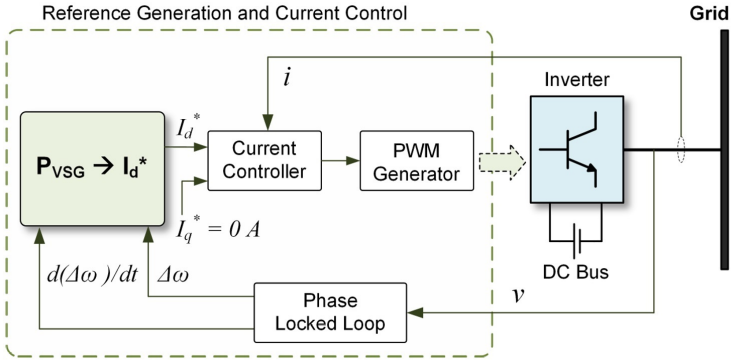

Figure 3.14: VSG topology

Although this topology has some advantages for the islanded mode, it can not be used as a grid forming for microgrids. Additionally, the system only provides inertial response to the frequency variations and not input power variations. Furthermore, the derivative term for ROCOF makes the system prone to noise and instability.

3.5 Uncategorized Methods

3.5.1 Droop Based Approach

The droop based method is mainly applied to autonomous operation of isolated microgrid systems [40, 41]. Assuming an inductive grid impedance, the frequency droop of the grid can be calculated from Eq. 3.20 [4]:

$$\omega_g = \omega^* - m_p(P_{out} - P_{in}) \tag{3.20}$$

where ω^* is the frequency of the local grid and P_{in}, P_{out} are reference and measured active power. The model developed from Eq. 3.20 is presented in figure 3.15. In this model, high-frequency components of the inverter are filtered out by a low-pass filter. The filter also introduces a delay in the measured value which can be interpreted as virtual inertia and although elementary, this model is quite usefeul as mentioned before. According to the developed model in figure 3.15, the frequency droop equation can be rewritten:

$$P_{in} - P_{out} = \frac{1}{m_p}(\omega^* - \omega_g) + T_f \frac{1}{m_p} s\omega^* \tag{3.21}$$

The disadvantage of this model is extremely slow transient response and the fact that the grid is not always inductive. However, adding a virtual impedance can alleviate this issue [42].

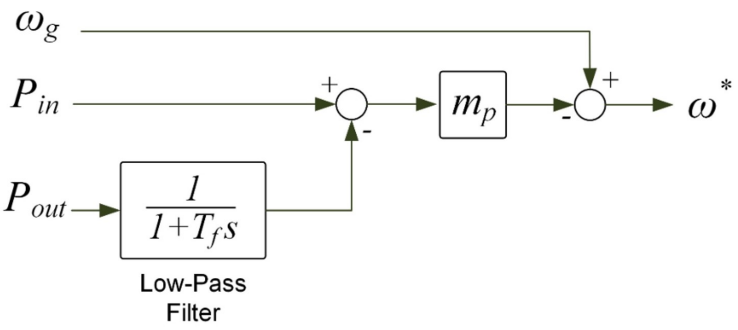

Figure 3.15: Droop-based topology

3.5.2 Rate Limiter Approach

The rate limiter approach was introduced by Zhang [43] in 2016. Similar to droop based approach, this model is not built on the idea of a complex modeling for controller but instead designing a simple, yet efficient controller to provide virtual inertia. This model utilizes a low-pass filter in its core. Figure 3.16 shows this model. In the model, the signal resulted from comparison of the nominal frequency and the power error is passed through a rate limiter function:

$$r = \frac{u(i) - y(i-1)}{t(i) - t(i-1)} \tag{3.22}$$

where $u(i), t(i)$ are the current input and actual time step of the limiter block while $y(i-1), t(i-1)$ are the output of the block in the previous time step and the previous time step. A non-linear function is then defined for the output of the block which is the reference frequency f_r:

$$y(t) = \begin{cases} \Delta t \cdot R + y(i-1) & \text{if} \quad r > R \\ \Delta t \cdot F + y(i-1) & \text{if} \quad r < R \\ u(i) & \text{otherwise} \end{cases} \tag{3.23}$$

in which R and F are rising slew rate and falling slew rate, respectively.

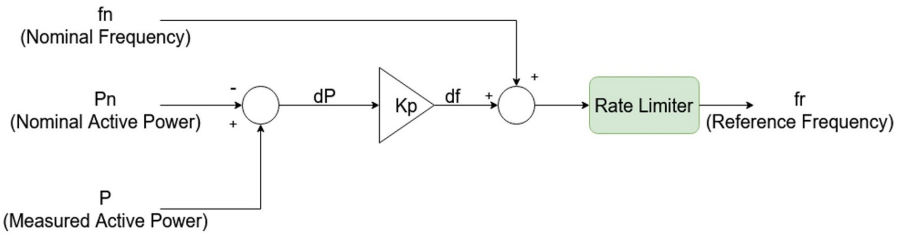

Figure 3.16: Rate limiter topology

3.5.3 Other methods

Methods to provide virtual inertia are abundant and a couple of other important topologies is introduced in this section. The VOC topology models a non-linear oscillator and is capable of maintaining synchronisation without any communication [44]. This topology although quite complex, is highly practical for grids with numerous Distributed Generation (DG)s.

Inducverters are one of the relatively new approaches and operate on the basis of mimicking the behaviour of induction machines instead of SG. An advantage of this model is the auto-synchronised PLL-less topology [45]. As figure 3.17 illustrates the model consists of a complex and detailed modeling of the induction machine, a block representing inertial response and an adaptive virtual impedance. The detailed model of the induction machine is out of scope of this thesis and is neglected.

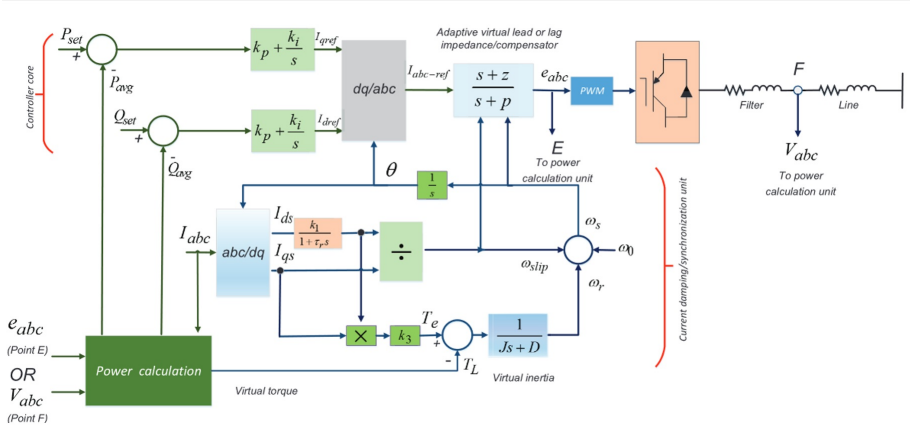

Figure 3.17: Inducverter control topology

Chapter 4

Proposed Methodology and Case Studies

4.1 Comparison Between the Existing Methods

The SG based models (synchronverter, IEPE, KHI and so on) are to some extent or entirely modeling the dynamics of the SG and most of these models require a PLL unit for synchronization with the grid. Although a derivative of the frequency is not required for these models, they have no over-current protection and this could cause numerical instability. On the other hand, the swing equation based models (ISE, SPC and so on) are simpler than SG based models. Similar to the previous category, these models do not require a frequency derivation, use PLL and have no over current protection. Additionally, power and frequency oscillations could be a problem in these models. The frequency power based model (VSYNC, virtual SG and so on) are mostly current source implementation and naturally have over current protection while the previous models were mainly voltage source based models. However, these models require frequency derivations, which can inject noise and cause instability problems in the system regardless of the possible instability problems of the PLL. The droop-based and rate limiter models are communication-less models that provide a slow transient response to contingency events naturally. Some of the novel models tend to implement the dynamics of induction machines or linear oscillators.

4.2 Selected Approach to Emulate Inertia

After analysing the literature of methods to provide virtual inertia, the aim was set to define a strategy that provides a response similar to the existing methods, while having the least possible complexity. Before selecting the method to provide virtual inertia in case of power deficit, the source of energy required for injecting additional energy to the grid of the platform must be determined. Since the case

scenarios defined later in this chapter are based on power deficit, this energy must be extracted form either (1) the available elements in the grid or (2) an external element. In the literature of case (1), as explained in the previous chapter, different methods suggested extracting energy from (i) the wind turbine or (ii) the capacitor in the DC link. In this project, the wind turbine is considered to run at nominal rotational speed and therefore, braking the turbine to extract the kinetic energy in the rotating mass of blades and generator in case of power deficit is not an option, not to mention the changes required in the converter controllers. Also, the DC link capacitor between the converters is practically not sufficiently large enough to provide the required energy for virtual inertia emulation and it has to carefully integrated in the control algorithm which increases the complexity of the system and can cause instability issues in voltage and power on its own. Furthermore, the gas turbines in the grid of the platform are only present to provide part of the loads that can not be supplied via the wind turbines and note that the ultimate aim of the project is to reduce the utilization of carbon emitting technologies such as gas turbines, which alternatively translate to limited use of gas turbines and investigating a solution in which the gas turbines do not participate in virtual inertia emulation. The analysis provided due to the characteristics of the understudy platform grid leads to one option, which is the addition of an external unit. Following the explanations in section 3.1 regarding addition of an external unit (case (2)) in a system, the installation and operation costs of the ESSs have decreased in a sense that they proved to be a feasible solution for the power deficit problem in near future. For all the reasons explained, a separate ESS unit was considered to be the provider of the energy required for emulation of the virtual inertia.

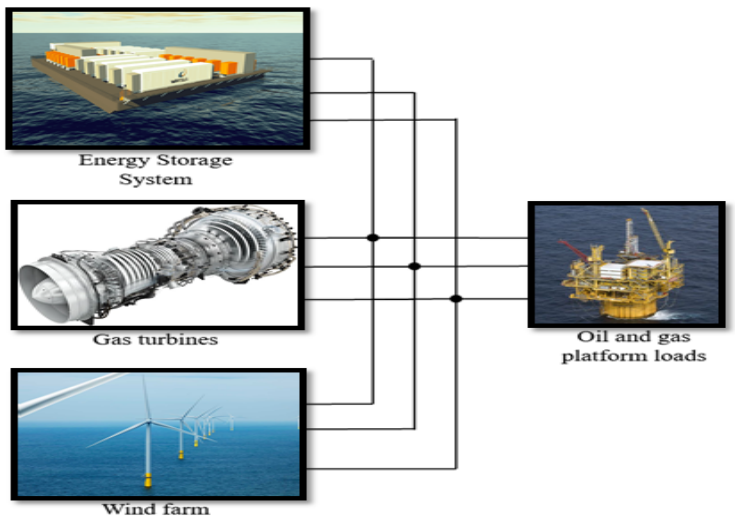

Figure 4.1: Project study case concept

The concept of the oil and gas platform is illustrated in figure 4.1. This concept is built from scratch and to make the project simpler, each component is designed separately, tested and then assembled to other components. In the end, the entire system is evaluated. The ESS is connected via a converter to the grid of the platform and the virtual inertia algorithm is embedded in the converter control. The complete model of the virtual inertia algorithm and the converter control with ESS unit, detailed model of the wind turbine and its converters, and the gas turbine are provided in the next chapter. Next section explains the cases defined during the project to build the concept model. Cases a, b, c are simply the progressions of the project in each step to built the final model, while cases d, e, f and g (actual case studies of the project) examine the effectiveness of virtual inertia algorithm during a power deficit scenario. The progressions were an essential part of the project analysis in order to better understand the dynamics of the platform and choosing the most suitable methods to model the the system. The progressions determined whether a choice was made correctly and in scope of the project or not and how each component must be altered to best achieve the final goal of the project which is emulating virtual inertia. After these progressions were made and satisfying results from the of the project model until that point were reached, the case studies were defined to test and analyse the effectiveness of the virtual inertia provision method.

4.3 Case studies

4.3.1 Case a

This case models the wind turbine and its drive train with pitch controller (wind turbine package). The aim is to build a wind turbine model that provides a constant torque for the input of the wind turbine generator. This case is defined for variable wind speeds and an optimum pitch angle for the wind turbine.

4.3.2 Case b

After modeling the wind turbine in the previous case, the DFIG is modeled in this section considering two different models for wind turbine (first model from case a, and second model from simplified wind turbine model of case a). Two control strategies for the Rotor Side Converter (RSC) are considered and tested, named direct speed control with PI controller and indirect control of speed for Maximum Power Point Tracking (MPPT) system. The RSC on the DC side is connected to a constant voltage source for testing the circuit.

4.3.3 Case c

The combination of the two control strategies and models in the previous case are tested in this case with a connection to the grid with GSC, with presence of DC link capacitor and grid side filters. The most stable design is chosen as the

representation for the wind farm in the concept model of the platform and it delivers the base load of the platform.

4.3.4 Case d

The developed wind farm model of the case c is connected to a gas turbine. The gas turbine is responsible for maintaining the grid and keeping the voltage and frequency constant while the wind farm supplies the base load of the platform. The gas turbine also supplies a small portion of the platform loads (certain loads that can not be supplied from the wind farm and need gas turbine). A step change in the load is considered to analyse the effect on frequency when ESS is not connected and virtual inertia algorithm is not present. At his point the grid platform is completely built and the frequency deviations should be evident in the simulation results. The next cases are expected to alleviate the frequency deviations of this case.

4.3.5 Case e

The virtual inertia is implemented from this case forward. In addition to the model in previous case, the ESS unit is modeled and the virtual inertia emulation algorithm is implemented on it in the form of a frequency droop control with a P controller. The effectiveness of the virtual inertia emulation method is analysed.

4.3.6 Case f

The same scenario as in case e but with a PI controller is designed and tested.

4.3.7 Case g

The same scenario as in case f but with an added dead band to the frequency in the ESS unit controller.

Chapter 5

Modeling

5.1 Introduction

The modeling of complex and detailed projects could be extremely confusing if not approached properly. In this study, in order to have a better analysing capability, the model is dismantled into different sections and then put back together in the end. In this chapter, the detail modeling and methodologies are explained. Different sections that are modeled separately are as followed:

- platform grid
- Wind turbines and their converters
- Virtual inertia provision unit

5.2 Platform grid

5.2.1 Loads

As mentioned in chapter 2, the detailed modeling of the platform grid is not essential for designing a virtual inertia algorithm. Therefore, the platform model was implemented with less detail and as a constant load. Nevertheless, some variations are considered in the load to analyse the efficiency of the virtual inertia algorithm. Based on the model presented in Annex 7.2, the total value of the loads in the platform are estimated around 45 MW. The parameters of the simulation of the electrical grid of the LEOGO platform are presented in Annex 7.2. The value of the load itself does not necessarily impact the modeling of the virtual inertia algorithm and therefore, the total loads of the platform are scaled down from 45 MW to 2 MW. The reason for scaling down is considering less capacity for the wind farm and less number of turbines. An additional 5 kW is considered for the loads that can not be supplied through the wind energy but supplied through the gas turbine. The model of the loads are considered as constant power loads.

5.2.2 Gas turbine

The platform also relies on three gas turbines and back up diesel generator that initially supplied the 45 MW loads of the platform. In the modeling of the system only one gas turbine is considered and the diesel generator is replaced by the ESS that provides the virtual inertia. To model the exact models, the wind turbines and gas turbines can be replicated (check appendix).

One gas turbine is modeled to support a portion of the loads that can not be supplied through wind. In addition, it helps to keep the voltage of the grid constant and contributes to maintaining the frequency at the nominal value. Table 5.1 provides the values for the salient pole gas turbine and the platform grid. The gas turbine is modeled as a SG with an AVR and governor.

Table 5.1: Gas turbine generator data

Parameter	Value	Description
f_n	50 [Hz]	Nominal grid frequency
V_n	690 [V]	Nominal grid voltage (LL_{RMS})
P_{load}	2.005 [MW]	Total loads on the platform
$P_{n_{gas}}$	10 [kW]	Nominal power of the gas turbine
X_d	2.24 [pu]	Steady state generator reactance (d-axis)
$X_{d'}$	0.17 [pu]	Transient generator reactance (d-axis)
$X_{d"}$	0.12 [pu]	Sub-transient generator reactance (d-axis)
X_q	1.02 [pu]	Steady state generator reactance (q-axis)
$X_{q'}$	0.13 [pu]	Transient generator reactance (q-axis)
$X_{q"}$	0.08 [pu]	Sub-transient generator reactance (q-axis)
$T_{d'}$	0.012 [s]	Transient time (d-axis)
$T_{d"}$	0.003 [s]	Sub-transient time (d-axis)
$T_{q"}$	0.003 [s]	Sub-transient time (q-axis)
R_s	0.037875 [pu]	Stator resistance
H	1.028 [s]	Inertia coefficient
F	0.02056 [pu]	Friction factor
P	2 [-]	Pole pairs
dw0	0 [%]	Initial speed deviation (% of nominal speed)
th0	0 [deg]	Initial angle of the rotor
ia0	1 [pu]	phase a initial current magnitude
ib0	1 [pu]	phase b initial current magnitude
ic0	1 [pu]	phase c initial current magnitude
pha0	0 [deg]	phase a initial phase
phb0	-120 [deg]	phase b initial phase
phc0	120 [deg]	phase c initial phase
Vf0	1 [pu]	Initial field voltage

5.2.2.1 AVR

AVR plays an important role in generation and in this project, it is used for generating the field voltage and maintaining the output voltage of the gas turbine. A typical AVR consists of five components [46]:

- Amplifier: amplifies the input reference voltage
- Exciter: generates the field voltage from the reference signal
- Generator: relation between the field voltage and the gas turbine voltage terminal
- Sensor: feedback for measuring the output voltage and comparing to the reference signal
- Additional controllers: for controlling the plant model of the first three components

Figure 5.1 illustrates the block diagram of an general AVR and its components. The first four components are usually modeled with a first order transfer function and the controller is typically a PID controller, while other control strategies can also be implemented.

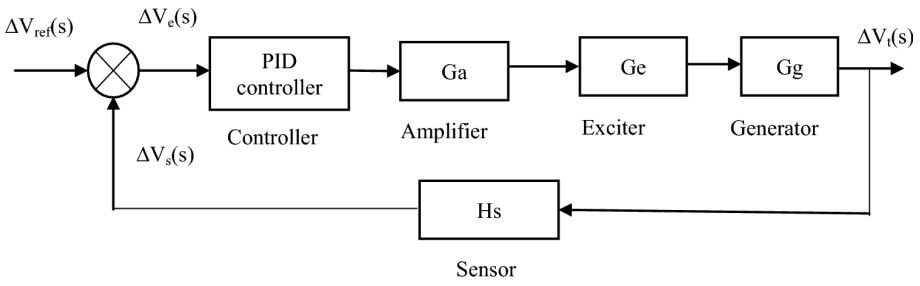

Figure 5.1: A typcial AVR model

AVR system can be extremely complicated but in this project to avoid complications, the IEEE type one topology for the AVR is used. The reference signal V_{ref} is given to the AVR along the stator voltage in d-q axis and zero input for stabilizer port (stabilizer port provides additional stabilization of the power system oscillations, which is neglected in the study). Table 5.2 presents the values used in the modeling of the AVR for the gas turbine.

5.2.2.2 Governor

Governors are used for controlling the rotational speed of generators and depending on the application and type of the generator, they will have different control systems. The generator speed is coupled with grid frequency and therefore,

Table 5.2: Gas turbine AVR data

Parameter	Value	Description
T_r	0.02 [s]	Low pass time constant
K_a	300 [-]	Regulator gain
T_a	0.001 [s]	Regulator time constant
K_e	1 [-]	Exciter gain
T_e	0 [s]	Exciter time constant
T_b	0 [s]	Transient gain reduction
T_c	0 [s]	Transient gain reduction
K_f	0.001 [-]	Damping filter gain
T_f	0.1 [s]	Damping filter time constant
Ef_{min}	-11.5 [pu]	Regulator output limit (min voltage)
Ef_{max}	11.5 [pu]	Regulator output limit (max voltage)
K_p	0 [-]	Regulator output gain
Et0	1 [pu]	Initial value of terminal voltage
Vf0	1.28 [pu]	initial value of field voltage
V_{stab}	0 [pu]	Stabilization reference signal
V_{ref}	1 [pu]	The desired stator terminal voltage

the governor is actually controlling the frequency. Some of the old and obsolete governor models are GAST, GAST2, GASTWD, GFT8WD, WESGOV and they are replaced with newer version such as GGOV1. For this project, a separate governor was designed with less complexity than the standard GGOV1 model.

A separate simple governor is designed modeling turbine delay and a droop control for turbine speed. Table 5.3 presents the values used in the modeling of the governor for the gas turbine. Figure 5.2 illustrates the schematic of the governor built for the gas turbine. The

Table 5.3: Gas turbine governor data

Parameter	Value	Description
K_{gov}	10 [-]	Governor delay gain
D_{gov}	0.05 [-]	Governor droop gain
Pm_{lim}	1 [pu]	Maximum output of the governor
Pm_{ref}	0.5 [pu]	Reference gas power
ω_{ref}	1 [pu]	Reference generator speed

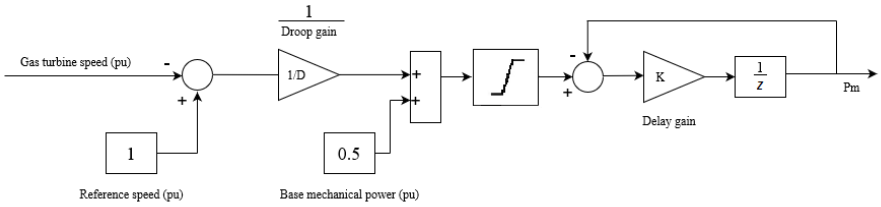

Figure 5.2: Governor model

5.3 Wind turbine and related converters

The wind turbine and its related converters consist of the following components ad they are tested separately first and assembled together later:

- Wind model
- Wind turbine, drive train and pitch controller
- Simplified wind turbine model
- DFIG
- RSC
- GSC

Table 5.4 contains parameters for modeling the wind profile, wind turbine, drive train and pitch controller and it has been continuously referenced during this chapter. Note that wind turbine is also scaled down according to the load and the nominal power of the wind turbine is 2.4 MW, while in practice, the offshore wind turbines have much higher power ratings. Since the idea for the wind farm is to only participate in supplying the base load and not getting involved in virtual inertia emulation, the size of 2.4 MW was selected.

5.3.1 Wind model

The aim of this section is to explain the wind model used in this project. The data for wind (average value, based value, cut-in, cut-out and turbulence of wind) are presented in table 5.4. The model that has been utilized in this study is the model developed by RISO National Laboratory of DTU based on Kaimal spectrum [47]. This model was accessed from an ongoing research, thanks to Daniel Mota- Ph. D. candidate at NTNU. The wind model considers both rotational turbulence and tower shadowing effect to on the wind speed. The model uses a built-in band-limited white noise generator that is explained in this section. As figure 5.3 illustrates, the inputs to the wind model are the rotor diameter (in this case radius of the rotor, extracted from equation 5.11), the length scale factor (L considered

Table 5.4: Wind turbine data

Parameter	Value	Description
V_{wind}	12 [m/s]	Average Speed of the wind and Base wind speed of the wind turbine
V_{cutin}	3 [m/s]	Cut in wind speed
V_{cutout}	20 [m/s]	Cut out wind speed
Tbl_{wind}	6 [%]	Turbulence intensity of wind
ρ_{air}	1.225 [kg/m^3]	Air density
β_{max}	45 [deg]	Maximum pitch angle
β_{opt}	0 [deg]	Optimal pitch angle
k_β	500 [-]	Proportional gain of the pitch controller
r_β	$\pm 2[-]$	Rate of change of pitch angle
H_{wt}	4 [s]	Wind turbine inertia constant
SS	0.3 [-]	Shaft stiffness of drive train
DC	1 [-]	Mutual damping coefficient of drive train
N	1 [-]	Gear ratio
λ_{opt}	8.1 [-]	optimal tip speed ratio of the wind turbine
$C_{p_{opt}}$	0.48 [-]	optimal performance coefficient of the wind turbine
C1	0.5176 [-]	Performance function coefficient
C2	116 [-]	Performance function coefficient
C3	0.4 [-]	Performance function coefficient
C4	5 [-]	Performance function coefficient
C5	21 [-]	Performance function coefficient
C6	0.0068 [-]	Performance function coefficient
$P_{n_{wt}}$	2 [MW]	Nominal power of the wind turbine
$P_{b_{wt}}$	$\approx P_{n_{wt}}[kW]$	Base power of the electrical generator ($P_{n_{DFIG}}$)
R_{wt}	42 [m]	Wind turbine radius
W_{base}	155 [rad/s]	Base rotational speed
$W_{b_{pu}}$	1 [pu]	Base rotational speed of the wind turbine (pu of base generator speed)
$P_{maxV_{wind}}$	1 [-]	Maximum power at base wind speed (pu of $P_{n_{wt}}$)

equal to $0.2R_{wt}$) which is used in calculating shadowing effect and finally, turbulence intensity. The model generates a random time series of wind speed with the average value of V_{wind}.

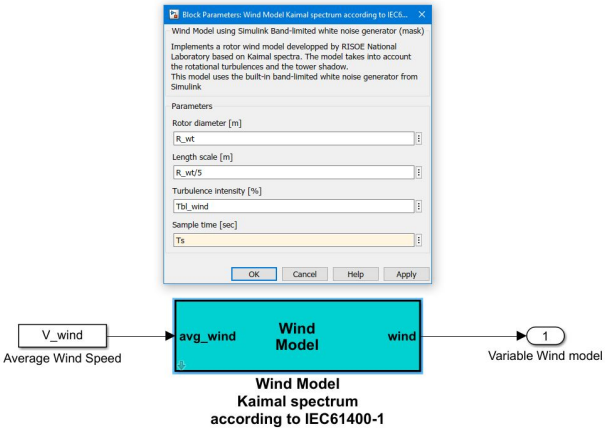

Figure 5.3: Wind speed model

Generally, wind speed can be defined with four components, named the average, gust, ramp and turbulence wind speeds [48]. Out of these four components only the turbulence is not given analytically and is yet the most challenging part to model. Researchers attempt to model wind turbulence with the assist of stochastic processes. One of these methods is the Spectral Representation Method (SRM), developed by Shinozuka and Jan [49]. SRM produces quite realistic samples according to Power Spectral Density (PSD). The presented wind model in this project, applies SRM to Kaimal PSD function [50] as shown in figure 5.4. The original Kaimal PSD is defined as:

$$s(f) = \frac{[\ln(h/z_0)^2]^{-1} \cdot l \cdot .V_{wind}}{(1 + 1.5(f \cdot l/V_{wind}))^{5/3}} \tag{5.1}$$

in which f, h, V_{wind}, l, z_0 are frequency $[Hz]$, height of the wind hub $[m]$, the average wind speed $[m/s]$, turbulence length scale $[m]$ and roughness length $[m]$. Equation 5.1 can be simplified as followed:

$$s(f) = \frac{c_1}{(1 + c_2 \mid \omega \mid)^{5/3}} \tag{5.2}$$

The model presented in this project, inspired from RISO model and based on Kaimal PSD function, consists of certain constants and function obtained from Equation 5.1. The function in figure 5.4 is:

$$f(u) = \frac{Tbl_{wind} \cdot \sqrt{L \cdot V_{wind}}}{100\sqrt{2}} \tag{5.3}$$

and the coefficients k, BD, CD, ED and FD in figures 5.5, 5.6 can be calculated as:

$$k = 0.0182/1.3463 \tag{5.4}$$

$$BD = \frac{1.3653}{1.3463(\frac{L}{2\pi V_{wind}})} \tag{5.5}$$

$$CD = \frac{0.9846}{1.3463(\frac{L}{2\pi V_{wind}})^2} \tag{5.6}$$

$$ED = \frac{3.7593}{1.3463(\frac{L}{2\pi V_{wind}})} \tag{5.7}$$

$$FD = \frac{1}{1.3463(\frac{L}{2\pi V_{wind}})^2} \tag{5.8}$$

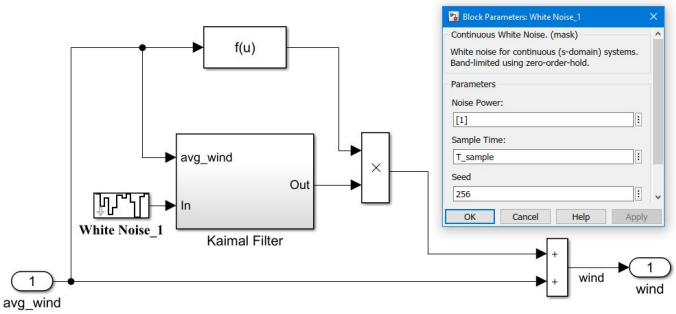

Figure 5.4: kaimal model for wind

The sample generated wind profile of the site was achieved with an average value of 12 m/s, presented in figure 5.7.

5.3.2 Wind turbine, drive train and pitch controller (Wind turbine package)

5.3.2.1 Wind turbine

The wind turbine chosen for study is a three bladed variable speed horizontal axis wind turbine with a two mass drive train. Figure 5.8 illustrates the model of the wind turbine, drive train and pitch controller and their connections referred to from now on as wind turbine package. In this section, the components of figure 5.8 are explained. The results of the simulation of this model are presented in chapter 6. The gains $k1$ and $k2$, are the nominal rotational speed and torque of the DFIG. The wind turbine package is implemented in pu but the inputs and

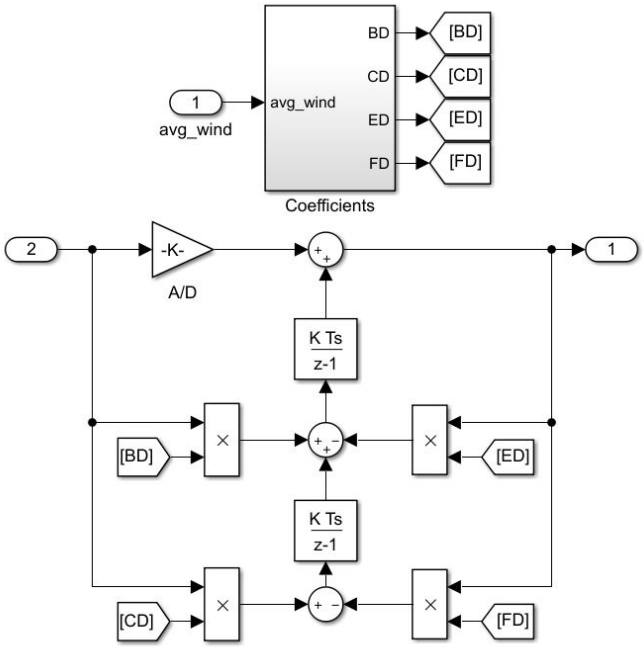

Figure 5.5: kaimal filter

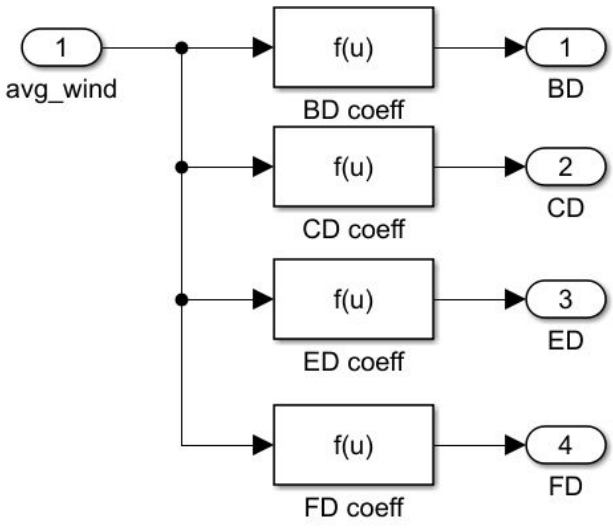

Figure 5.6: Kaimal coefficients

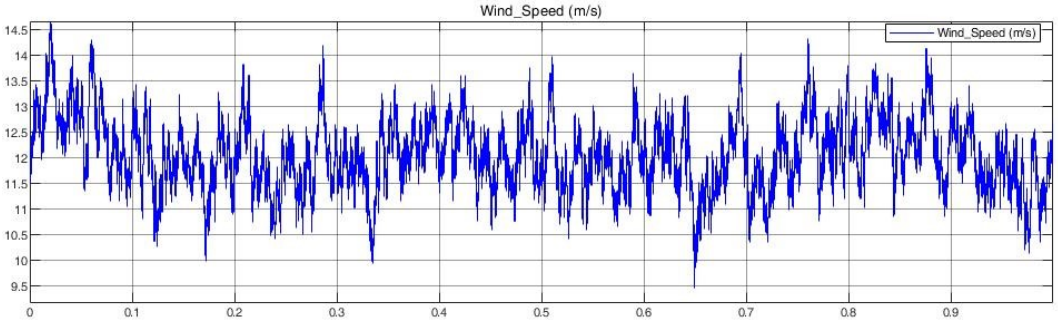

Figure 5.7: Wind speed profile of the site

outputs of the DFIG must be in physical units according to the Matlab model. DFIG model has been explained later on in this chapter and the data of the DFIG necessary to calculate $k1$ and $k2$ can be found in table 5.6. Note that since DFIG is operating in generator mode, the input torque ($T_{m_{in}}$) has to be negative, while the wind turbine package, produces a positive torque reference (T_m the output of the wind turbine is also negative, but the drive train model operates with positive values of input and output torque).

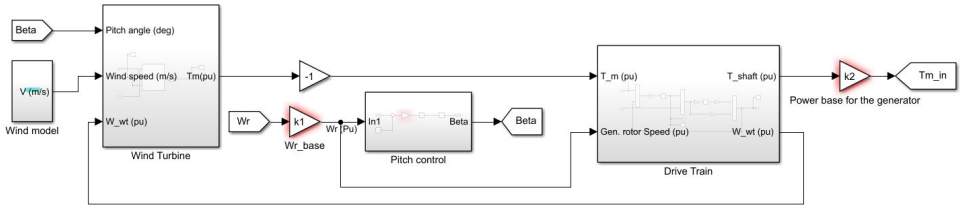

Figure 5.8: Wind turbine, drive train and pitch controller (wind turbine package)

$$k1 = \omega_{r_{base}} \tag{5.9}$$

$$k2 = -\frac{P_{n_{DFIG}}}{\omega_{r_{base}}} \tag{5.10}$$

The same wind turbine block of the Matlab was rebuilt for this project in order to have access to the parameters in the model such as C_P and λ that are not accessible in the wind turbine block of Matlab. Matlab description of the wind turbine model: "The block implements a variable pitch wind turbine and the performance coefficient (C_P) is implemented internally as the mechanical output power of the turbine over wind power. C_P is a function of wind speed, rotational speed and pitch angle (β) with maximum value at $\beta = 0$". The model parameters are depicted in figure 5.9 and the values assigned to them are provided in table 5.4. However, as mentioned in the description by Matlab, this model does not include the drive

train. Hence, a separate drive train was developed according to the model in [51]. The pitch control is also a simple proportional gain based on the same reference.

According to the values assigned, the turbine characteristic curve can be plotted for different wind speeds. Figure 5.10 is sketched from the default values of the Matlab model as in table 5.5, while figure 5.11 is sketched from the data of the rebuilt model provided in table 5.4. According to the set values for the turbine parameters, both wind turbine and DFIG have the same nominal speed and output mechanical power. Although practically, the values are not the same and the default values set by Matlab are preferred, for simplicity and convenience these values have been set the same. However, this assumption does not affect the performance of the developed model and it could be operated with unequal value for the mentioned parameters.

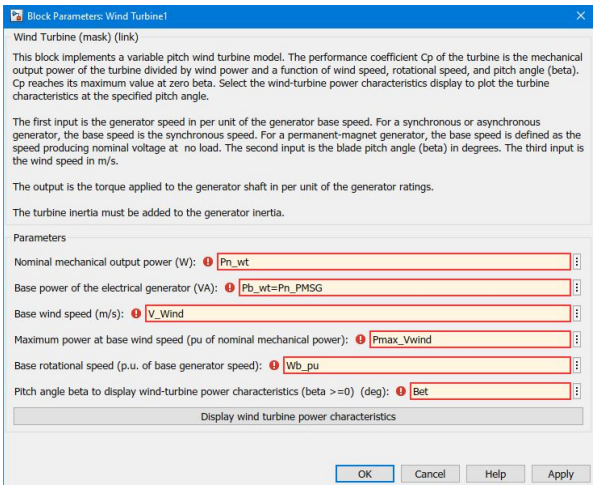

Figure 5.9: Wind turbine block parameters

Table 5.5: Default wind turbine data of Matlab

Parameter	Value
P_{nwt}	1.5 [MW]
P_{bwt}	1.5/0.9 [MW]
V_{wind}	12 [m/s]
W_{bpu}	1.2 [-]
$P_{maxV_{wind}}$	0.73
β	0 [deg]

The wind turbine model is presented in figure 5.12. The model inputs are wind speed profile (coming from the kaimal model $[m/s]$), Generator speed (coming from drive train [pu]) and pitch angle (coming from pitch controller [deg]) and

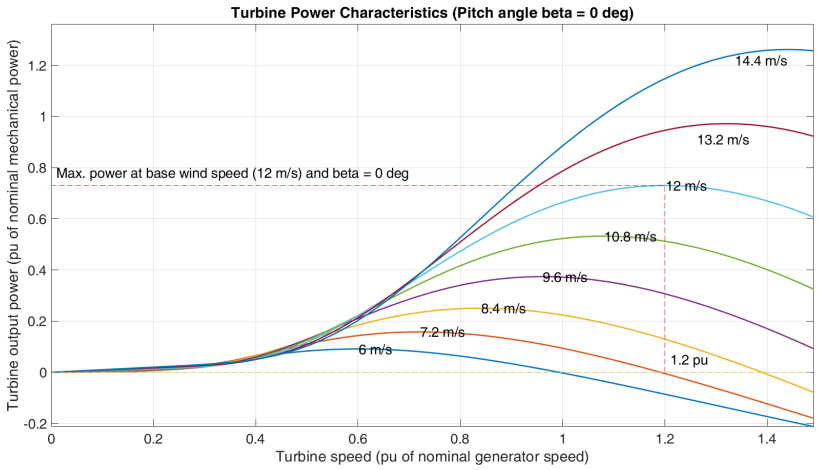

Figure 5.10: Wind turbine power characteristics for default MATLAB values

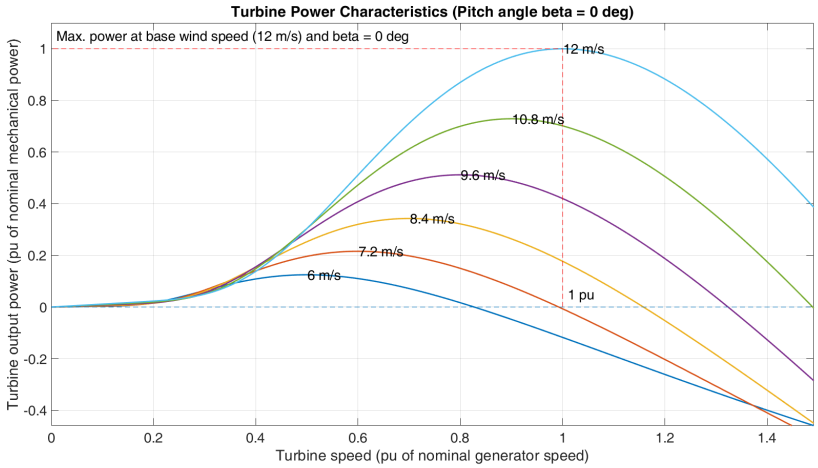

Figure 5.11: Wind turbine power characteristics for the modeled wind turbine

the output of the wind turbine is mechanical torque load on the shaft (which is the input to the drive train [pu]). This model develops the known wind turbine power and torque equations:

$$P_{wind} = 0.5_{air} \cdot (\pi \cdot R_{wt}^2) \cdot V_{wind}^3 \tag{5.11}$$

$$C_P(\lambda, \beta) = \frac{P_m}{P_{wind}}; C_P < 1 \tag{5.12}$$

$$T_m = \frac{P_m}{W_{wt}} \tag{5.13}$$

and the gains highlighted in red are calculated as followed:

$$k1 = \frac{1}{V_{W_{base}}} = \frac{1}{V_{wind}} \tag{5.14}$$

$$k2 = \frac{1}{W_{bpu}} \tag{5.15}$$

$$k3 = \lambda_n \tag{5.16}$$

$$k4 = \frac{1}{C_{P_n}} \tag{5.17}$$

$$k5 = \frac{P_{max V_{wind}} \cdot P_{n_{wt}}}{P_{b_{wt}}} \tag{5.18}$$

These gain values are directly affected by the parameters defined in figure 5.9 and presented in table 5.4. Note that $k1$ is one over the base wind speed considering the same values for both average wind speed and base wind speed, the output of the gain would be in per unit of the average wind speed. The performance coefficient function C_P depends on both Tip Speed Ratio (TSR) (λ) and pitch angle (β). C_P is calculated in the subsystem highlighted in blue in figure 5.12 from the following equations:

$$C_P(\lambda, \beta) = C_1(c_2/\lambda_i - C_3\beta - C_4) \cdot e^{(-C_5/\lambda_i)} + C_6\lambda \tag{5.19}$$

$$\frac{1}{\lambda_i} = \frac{1}{\lambda + 0.08\beta} - \frac{0.035}{1 + \beta^3} \tag{5.20}$$

in which C_1 to C_6 are the performance coefficients parameters defined in table 5.4. Accordingly, the nominal value of C_P and λ are set to the optimum values derived from this function. The maximum C_P is calculated at $\beta = 0$ & $\lambda = 8.1$ and equal to 0.48. Furthermore, since the power needed from the wind farm is known previously, the blade radius can be designed for the optimum values and the desired power. Note that R_{wt} is essential as an input parameter to the wind profile modeling with Kaimal spectrum as it is related to the length scale.

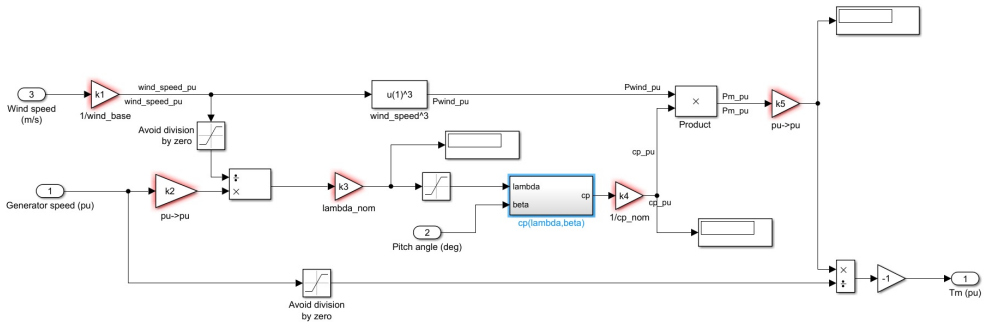

Figure 5.12: Wind turbine model

5.3.2.2 Drive train

Drive trains in wind turbines are responsible to transfer the energy from the wind turbine blades to the generator and they consist of gearboxes. Two types of common gearboxes for wind turbines are planetary and parallel type. The number of the gearboxes rotating together in the drive train depends on the speed of the shaft. Higher speeds require more and bigger gear and usually planetary or a combination of planetary and parallel are used. The term of mass is also used to indicate the complication of the drive train [52].

As mentioned, the output torque calculated from the wind turbine goes through the drive train (Figure 5.13). A two mass drive train [51], models the shaft stiffness, mutual damping (second part) and the inertia (first part) of the wind turbine (Note that the wind turbine model in figure 5.12 does not incorporate the turbine inertia). The initial values of the discrete integrators are defined such that the steady state value is calculated faster. The gains highlighted in red are gains $k1 = 0.5/H_{wt}$ and $k2 = \omega_{r_{base}}$ and gear ratio is considered as one for convenience ($N = 1$). The governing equations behind the drive train model are as followed:

$$2H_{wt}\frac{d\omega_{wt}}{dt} = T_m - T_s \tag{5.21}$$

$$\frac{\theta_{sta}}{dt} = \omega_{wt} - \omega_r \tag{5.22}$$

$$T_s = SS \cdot \theta_{sta} + DC \cdot \frac{\theta_{sta}}{dt} \tag{5.23}$$

Equations 5.21, 5.22, 5.23 model the inertial response of the wind turbine, shaft twist angle and the shaft torque , respectively, where,

H_{wt} = Inertia constant of the wind turbine $[s]$
θ_{sta} = Shaft twist angle $[deg]$
ω_{wt} = Wind turbine speed $[pu]$

ω_r = DFIG rotor speed $[pu]$
T_s = Shaft torque $[pu]$
SS = Shaft stiffness [-]
DC = Damping coefficient [-]

and the values for SS, DC and H_{wt} can be found in table 5.4.

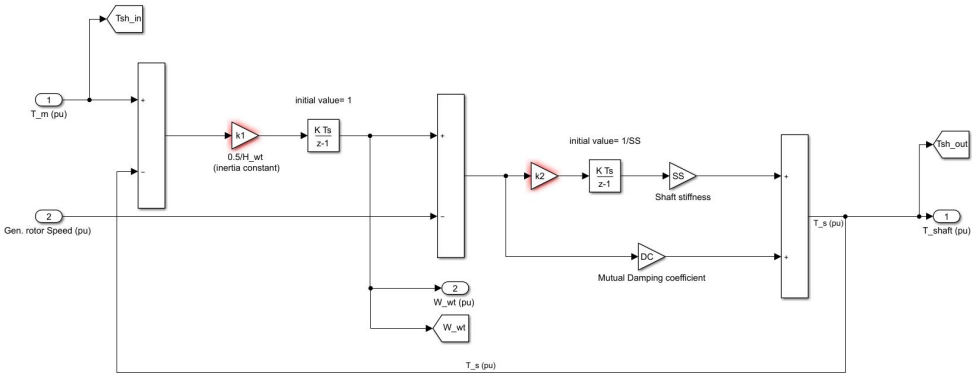

Figure 5.13: Two mass drive train model

5.3.2.3 Pitch control

Multiple pitch control strategies have been introduced in the literature. Pitch control is used to reduce/increase the angle of the wind turbine blades with the incoming wind such that the power output of the turbine is controlled. The pitch controller is commonly used for MPPT purposes with a wide variety of simple to complex algorithms. The idea of using pitch control instead of stall control is crucial specially in high wind speeds and offshore wind farms. Pitch controls fall into categories of conventional, collective, individual, electric, robust and soft controllers [53].

In this project a conventional pitch control system is used. The pitch controller [51] presented in figure 5.14 compares the rotor speed of the connected generator to the shaft of wind turbine (DFIG) with the reference speed of 1 pu and the error is multiplied by a gain ($k_\beta = 500$) and given as the pitch signal to the wind turbine in figure 5.12. The pitch is limited to the values is table 5.4 with β_{opt}, β_{max}, and r_β.

5.3.3 Simplified wind turbine model

The wind turbine model explained in section 5.3.2 can be simplified without loosing valuable information for the purpose of the project. The simplified version is analysed against the detailed model. The reason for developing an additional

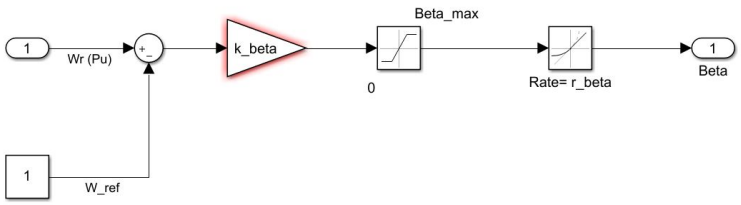

Figure 5.14: Pitch controller

model for the wind turbine is that details of the model of section 5.3.2 do not directly affect the virtual inertia algorithm or system response to a contingency event. Therefore, an additional model for the wind turbine has been developed with less detail and presented in this section. Figure 5.15 demonstrates the model. In this model, first TSR is calculated and the value is used in a look up table to find the corresponding C_t. The value of C_t is then used to calculate the input torque signal for the DFIG. C_t is the torque coefficient and $f1$ and $f2$ are the TSR and torque equations (in figure 5.15).

$$C_t = \frac{C_P}{\lambda} \tag{5.24}$$

$$f1 = \lambda \tag{5.25}$$

$$f2 = 0.5\rho_{air} \cdot R_{wt}^3 \cdot V_{wind}^2 \cdot C_t \tag{5.26}$$

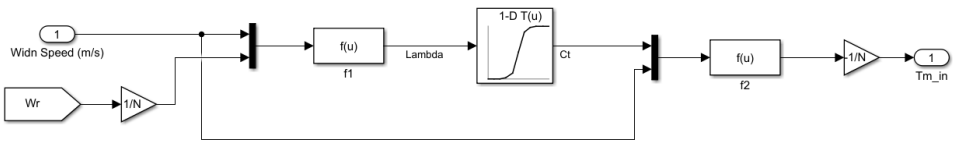

Figure 5.15: Simplified wind turbine model

In the simplified model the pitch angle is considered to be constant ($\beta = 0$) and a gear ratio of 1:100 is selected. The look up table reads the data from the figure 5.16.

5.3.4 DFIG

DFIGs are the conventional design for the wind turbines and in this project, the wind turbine is coupled with a DFIG. The DFIG has a wound type rotor, three phases and rotor is set as reference frame. No saturation is considered for the model and the initial conditions are all set to zero. This generator is mainly responsible for supporting the main load of the platform with a connection through

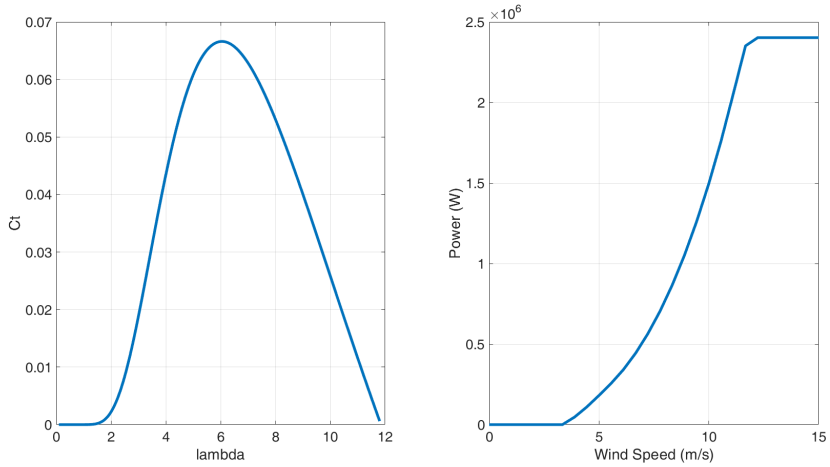

Figure 5.16: (left) Torque coefficient-λ, (right) Power-V_{wind}

back-to-back converters (type 3). This enables the control of DC link voltage, generator speed, active and reactive power delivered to the platform. The converters used in the model are ideal with switching frequency of $16kHz$. The value for switching frequency although not in accordance with the size of the converters, does not affect the general performance of the system. The generator data are presented in table 5.6.

Table 5.6: DFIG data

Parameter	Value	Description
P_n	2 [MW]	Nominal power of the DFIG
$\omega_{r_{base}}$	155 [rad/s]	Base rotational speed
f_n	50 [Hz]	Nominal frequency
V_n	690 [V]	Nominal three phase-to-phase voltage
u	1/3	Stator/rotor turn ratio
s_{max}	1/3	Maximum slip
R_s	0.0026 [Ω]	Stator resistance
R_r	0.0029 [Ω]	Rotor resistance
L_{ls}	0.087 [mH]	Leakage inductance
L_m	2.5 [mH]	Linkage inductance
J	127 [kg.m^2]	Moment of inertia
P	2 [-]	Pole pairs

The model of the DFIG used is the original block of the Matlab and in order to implement the control strategies for the RSC and GSC, the model explained in [14] and chapter 10 of [15] are implemented.

5.3.5 Rotor Side converter (RSC)

The control of RSC differs according to the goal of the converter (Zero D-axis Current (ZDC), Unity power Factor (UPF), Constant Stator Voltage (CSV)) but the majority of the control methods implement the following procedure:

- Define parameters of interest that are desired to be controlled such as generator speed, active or reactive power and so on
- implement (an outer layer) controller for the parameters of interest and generate reference signals for currents or voltages depending on the control strategy
- implement (an inner layer) controller for currents/voltages
- implement any additional calculations to generate the desired PWM signals for the converter.

In this project, the ZDC method is selected. For convenience of the design and control, the converter controllers are not implemented in the abc reference frame but in dq0. Therefore, while modeling all the vectors on d and q reference frames, one can separate the controllers in each reference frame with decoupling terms. In the ZDC control strategy, the d-axis reference for current is set to zero, resulting in all the power being controlled by the q-axis vectors. Figure 5.17 illustrates the RSC control strategy to generate the PWM signals.

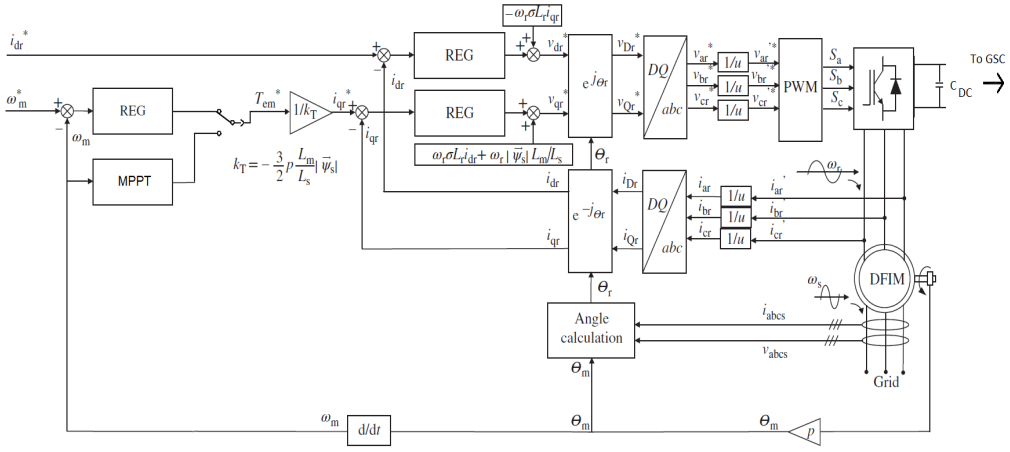

Figure 5.17: Vector control of the RSC

The d-axis current reference is set to zero as mentioned and the q-axis current is generated from the outer layer controller for the rotor speed. Two controller are

designed for the outer controller and they are evaluated against each other. First controller follows the speed reference and the other one, implements an indirect speed control with a MPPT scheme. The output of the outer layer controller is the torque reference, which then is multiplied by a gain to give the current reference for the q-axis. The current references are then regulated with the inner layer controllers and after adding the decoupling terms, the d and q-axis voltage references are generated and sent to the PWM generator. In this method, the three phase rotor currents are sampled and sent as a feedback to the inner layer controllers of the current. A 3rd harmonic injection algorithm (section 2.4.7.4) is also implemented before all the PWM inputs on the reference voltages. The PWM model implements the SVPWM technique explained in section 2.4.7.3 for all the converters in this project. PLL is developed for extracting the frequency and angle of the line voltages.

5.3.5.1 PLL circuit

The PLL circuit used in this model was inspired by [54]. The operation of the model is quite similar to the explanations given in section 2.4.4. Sampled voltage is transformed to d-q reference frame and the angles are calculated. The rest of the procedure is illustrated in figure 5.18. The data used for the PLL are also available in figure 5.19. This design outputs the frequency, the angle and the sin and cos of the angle. This PLL is used in all the cases where a PLL is needed.

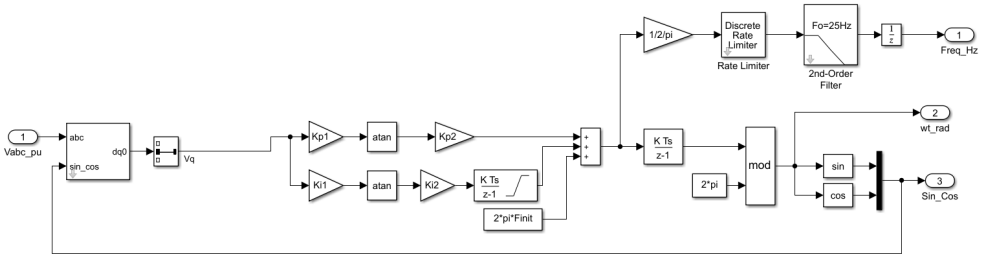

Figure 5.18: PLL circuit

5.3.5.2 Angle calculation for RSC

The angle used in calculating the park transformations can be calculated from equation 5.27 and 5.28.

$$\theta_s = \theta_{PLL} - \frac{\pi}{2} \tag{5.27}$$

$$\theta_r = \theta_{PLL} - P \cdot \theta_m \tag{5.28}$$

in which θ_m, θ_r, θ_s, θ_{PLL} and P are the mechanical angle of the shaft, electrical angle of the rotor, stator and PLL.

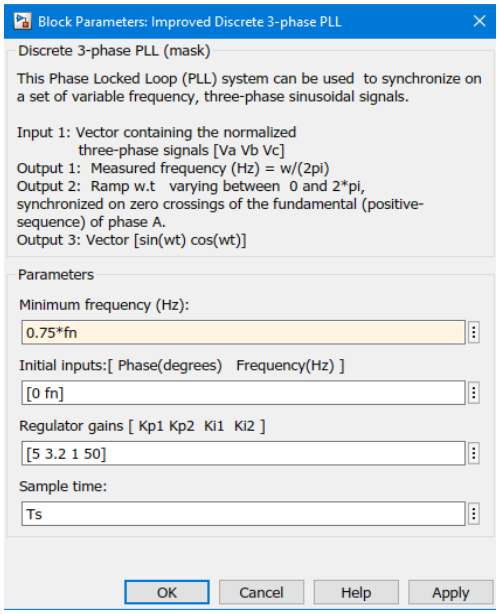

Figure 5.19: PLL data

5.3.5.3 Decoupling terms in RSC

To consider the effect of compensation for coupling between d and q axis the decoupling terms are used after the current controllers from Eq 5.29 and 5.47 while neglecting the effect of the converter and possible delays in the system:

$$V_{dr} = e_{dr} - \omega_r \sigma L_r i_{qr} \tag{5.29}$$

$$V_{qr} = e_{qr} + \omega_r \sigma L_r i_{dr} + \omega_r \frac{L_m}{L_s} \mid \vec{\psi}_s \mid \tag{5.30}$$

in which e_{dr} and e_{qr} are the outputs of the current regulators and V_{dr} and V_{qr} are the reference voltage signals for the SVPWM and ψ_s is the approximated stator flux [15] calculated as followed:

$$\mid \vec{\psi}_s \mid = \frac{\sqrt{\frac{2}{3}} V_n}{2\pi f_n} \tag{5.31}$$

$\mid \vec{\psi}_s \mid$ is also used to generate the q axis current reference from the torque (figure 5.17).V_{dr} and V_{qr} are then transformed to abc reference frame with inverse park transformation and fed to the SVPWM block. The decoupling of the d and q axis enables the separate control for the d and q axis currents to generate e_{dr} and e_{qr} separately with equal controllers for both d and q axis.

5.3.5.4 Current regulators

The conventional method for controlling dq currents is using a PI controller tuned by modulus optimum criterion [55]. The modulus optimum is selected for cases in which the system has one dominant time constant along several minor one. The idea of this method is to cancel the largest time constant of the system with the controller. Assuming the controller has no time delay from switching of the converter, sampling/measurements and other calculations in the controller, the plant model of the DFIG on the rotor side can be written as:

$$G_{plant} = \frac{1}{R_r} \cdot \frac{1}{1 + \tau_i \cdot s} \tag{5.32}$$

where $\tau_i = \dfrac{\sigma \cdot L_r}{R_r}$ and $\sigma = 1 - L_m^2 / L_s L_r$ as defined in section 2.3.3. Considering that the inner loop controllers (current controllers) must be faster then the outer loop controllers (speed controller), while slower than the switching frequency of the converter, the natural frequency of the current controller is set to one decade lower than the switching frequency:

$$\omega_{ni} = 0.1 f_{sw} = 1.6 kHz \tag{5.33}$$

Therefore, the proportioanl and integral gains of the current controller are:

$$k_{pi} = (2\omega_{ni} \cdot \sigma \cdot L_r) - R_r = 0.5771 \tag{5.34}$$

$$k_{ii} = \omega_{ni}^2 \cdot L_r \cdot \sigma = 491.5995 \tag{5.35}$$

Note that the exact same controllers are used for both d and q axis currents.

5.3.5.5 Speed regulator

The conventional method for controlling outer loop parameter (speed/ voltage and so on) is using a PI controller tuned by symmetrical optimum criterion [55]. The reason is that adding another pole to the system transfer function, builds a third order transfer function that can not be tuned with modulus optimum. Although assuming that the inner layer controller is much faster than the outer layer controller, the transfer function of the inner layer controller can be simplified to a constant gain, resulting in a reduce order of the third order transfer function [56]. Hence modulus optimum can be applied again. the plant model of the DFIG speed can be found from the inertial response of the DFIG:

$$G_{plant} = \frac{P_{DFIG}}{J_{DFIG} \cdot s} \tag{5.36}$$

Considering that the inner loop controllers (current controllers) are faster then the outer loop controllers (speed controller), the natural frequency of the speed

controller is set approximately three decade lower than the switching frequency and two decade lower than the current controller natural frequency:

$$\omega_{n\omega} \simeq 0.01\omega_{ni} = 20Hz \tag{5.37}$$

Therefore, the proportioanl and integral gains of the current controller are:

$$k_{p\omega} = (2\omega_{n\omega} \cdot J_{DFIG})/P_{DFIG} = 2540 \tag{5.38}$$

$$k_{i\omega} = \omega_{n\omega}^2 \cdot J_{DFIG}/P_{DFIG} = 25400 \tag{5.39}$$

5.3.5.6 MPPT

For designing the MPPT algorithm an indirect speed control [14] is considered. While the wind speed changes, the algorithm adapts the reference torque signal of the DFIG in order to extract the maximum power from the wind turbine. Figure 5.20 illustrate MPPT on general power and torque charts. While working in maximum power point, the turbine characteristics are as followed:

$$\lambda_{opt} = \frac{R_{wt} \cdot W_{wt}}{V_{wind}}; \quad C_P = C_{Pmax}; \quad C_t = C_{tmax} \tag{5.40}$$

According to the optimal values torque is calculated as:

$$T_{opt} = K_{opt} \cdot \omega_{wt}^2 \tag{5.41}$$

$$K_{opt} = 0.5\rho_{air}\pi \frac{R_{wt}^5}{\lambda_{opt}^3} C_{Pmax} \tag{5.42}$$

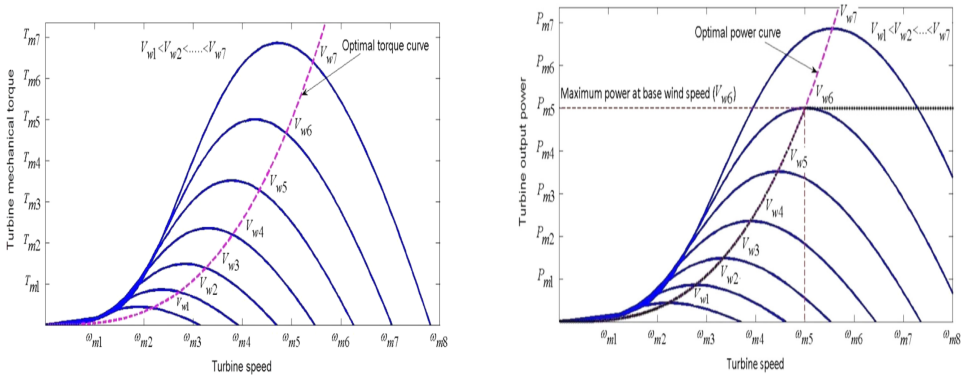

(a) **(b)**

Figure 5.20: MPPT graph on (a) $P - \omega$, (b) $T - \omega$ charts for different wind speeds

The speed of the generator is sent as feedback to the MPPT algorithm and after applying Eq 5.41, the reference torque signal is generated. The value for K_{opt} according to wind turbine parameters in 5.4 is calculated 2.96×10^5. Figure 5.21 demonstrates the implemented algorithm.

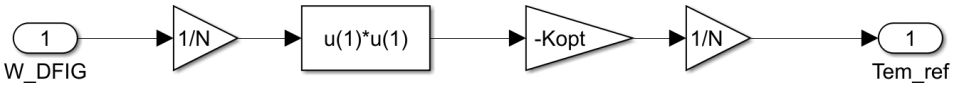

Figure 5.21: MPPT algorithm

5.3.6 Grid Side Converter (GSC)

A similar approach is taken for designing the GSC. Figure 5.22 illustrates the GSC controller. Instead of d axis, the q axis current reference is set to zero and the d axis reference is generated by the DC link voltage controller. The rest of the strategy is quite similar.

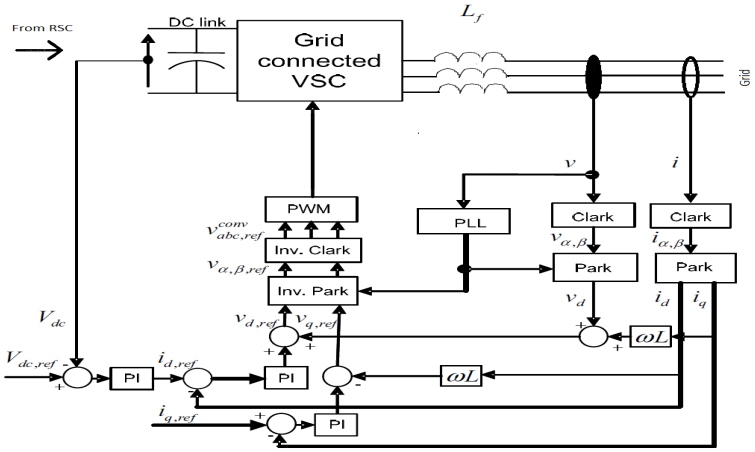

Figure 5.22: Vector control of the GSC

5.3.6.1 DC link capacitor

The Dc link capacitor [57–59] is sized in the industry according to three criteria named, ripple voltage/current rating, DC voltage rating, resonant frequency rating. The KCL for the DC link:

$$i_{dc} = C_{DC} \cdot \frac{dV_{DC}}{dt} + i_L \tag{5.43}$$

where i_{DC} and i_L are the DC current (connected to the RSC) and the load currents (connected to the GSC). In the back to back converters, the most important criteria for the design of the DC link capacitor is the voltage ripple. A typical value for the voltage ripple is 0.01 to 0.02 pu. Accordingly, $C_{DC} = 80mF$ is selected to satisfy this condition with parameters of table 5.6 and a DC voltage level of 1150 V.

5.3.6.2 GSC filters

The addition of power converters in power systems causes injection of harmonics. These harmonics have to be limited in order for the grid components to function appropriately. In the back to back converter strategy, usually a filter is designed to filter the harmonics and output a smoother signal with low ripple. In this project a simple RL filter is designed to rectify this issue and placed between the GSC and PCC as shown in figure 5.22. The parasitic resistor is usually in the range of 0.001 to 0.01 pu and as a general criteria, the inductance of the filter considered must limit the current limit to maximum 10% of the rated current amplitude [60]. The value of the inductance typically can be calculated from Eq 5.44.

$$L_{fl} = \frac{(V_{DC} - D \cdot V_{DC}) \cdot D}{2\Delta i_{max,p-p} \cdot f_{sw}} \tag{5.44}$$

$$\Delta i_{max,p-p} = 0.1\sqrt{2} I_{base} \tag{5.45}$$

The maximum current ripple occurs for duty cycle of $D = 0.5$. The values of the filter selected for the system are $R_{fl} = 0.02m\Omega$ and $L_{fl} = 0.4mH$.

5.3.6.3 Decoupling terms in GSC

The decoupling terms for compensation in the GSC that generate the dq reference voltage signals(V_{dg}, V_{qg}) for the inverter are as followed:

$$V_{dg} = e_{dg} - (2\pi f_n) L_{fl} \cdot i_{qg} + u_{dg} \tag{5.46}$$

$$V_{qg} = e_{qg} + (2\pi f_n) L_{fl} \cdot i_{dg} + u_{qg} \tag{5.47}$$

where e_{dg} and e_{dg} are the output signals of the current regulators, u_{dg} and u_{qg} are the feed-forward of the sampled grid voltage.

5.3.6.4 Current regulators

The design of the current regulators of the GSC are similar to the design of the RSC current regulators explained in section 5.3.5.4. The difference is that the plant transfer function is calculated from Eq 5.48:

$$G_{plant} = \frac{1}{R_{fl}} \cdot \frac{1}{1 + \tau_i \cdot s} \tag{5.48}$$

where $\tau_i = \frac{L_{fl}}{R_{fl}}$. The natural frequency of the current controller:

$$\omega_{ni} = 400Hz \tag{5.49}$$

Therefore, the proportioanl and integral gains of the current controller are:

$$k_{pi} = (2\omega_{ni} \cdot L_{fl}) - R_{fl} = 0.3016 \tag{5.50}$$

$$k_{ii} = \omega_{ni}^2 \cdot L_{fl} = 56.8489 \tag{5.51}$$

5.3.6.5 DC voltage regulator

The voltage regulator for the GSC is tuned according to the same method in section 5.3.5.5.

$$k_{pv} = 1.2 \tag{5.52}$$

$$k_{iv} = 360 \tag{5.53}$$

5.4 Virtual inertia provision unit

The Virtual Inertia Converter (VIC) control strategy is quite similar to the GSC control strategy with adaptations for implementing the inertial response. Instead of extracting energy form the DC link (as in back to back converter), the energy is supplied via an ESS. The ESS used in this project is a controlled current source. The voltage of the ESS is kept constant at V_{ESS} with a very fast PI controller and the output of the controller is the current reference for the controlled current source. The current is passed through a switching converter which is controlled with the VI algorithm. Figure 5.23 depicts the VIC controller. The q axis current reference is set to zero, while the d axis current reference is generated from the frequency controller, which is responsible for the inertial response for the frequency. The ac side filters are designed with the same method as in section 5.3.6.2. The decoupling terms are also the same as section 5.3.6.3. The current references of the current regulators are calculated from the reference active and reactive powers of the inverter:

$$P = V_d \cdot id + V_q \cdot i_q \tag{5.54}$$

$$Q = V_q \cdot id - V_d \cdot i_q \tag{5.55}$$

Considering zero q axis voltage and zero reactive power reference:

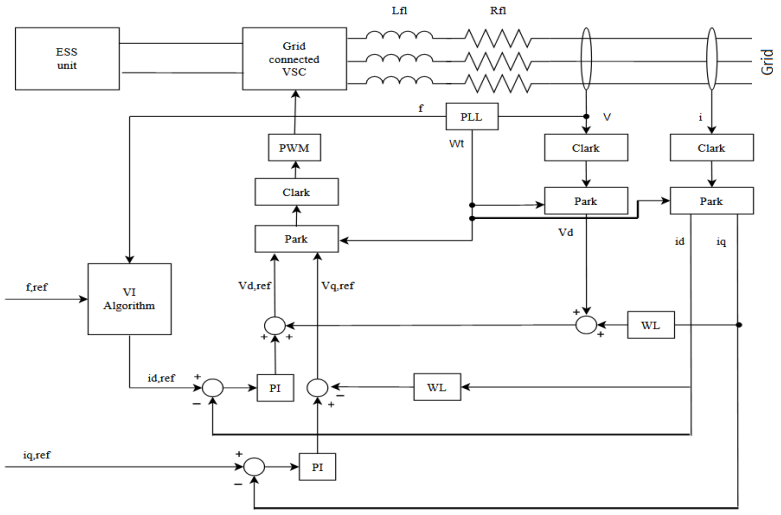

Figure 5.23: Vector control of the VIC

$$id_{d,ref} = \frac{P}{V_d} \tag{5.56}$$

$$i_{q,ref} = 0 \tag{5.57}$$

where P is the active power reference (output of the frequency controller, VI algorithm). Table 5.7 demonstrates the VIC data for simulation.

Table 5.7: VIC data

Parameter	Value	Description
f_n	50 [Hz]	Nominal frequency of the grid
V_n	690 [V]	Nominal line to line RMS voltage
V_{ESS}	1150 [V]	ESS DC voltage
f_{sw}	15 [kHz]	Switching frequency
R_{fl}	0.5290 [Ω]	Filter resistance
L_{fl}	33.37 [mH]	Filter inductance

The strategy for VI in this project is on the same base as frequency power based methods explained in section 3.4. The frequency variation is controlled and dq reference currents are generated. This method although not having the derivative term, still has the issues incorporated with methods of section 3.4. The VI algorithm is developed in three cases, named case e, f, and g:

5.4.1 Case e

In this case, the VI is implemented with a P controller. Figure 5.24 demonstrates the model:

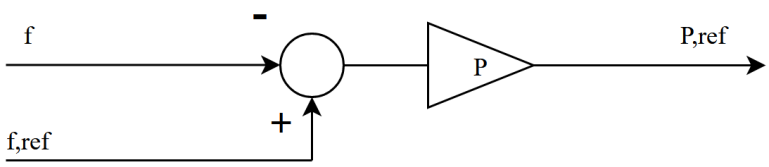

Figure 5.24: Case e- Virtual inertia provision with P controller

where, k_P is the proportional gain equal to 1000.

5.4.2 Case f

In this case, the VI is implemented with a PI controller. Figure 5.25 demonstrates the model:

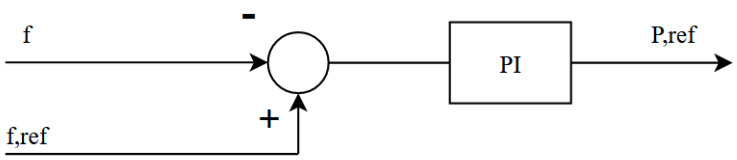

Figure 5.25: Case f- Virtual inertia provision with PI controller

where, k_P and k_i are the proportional and integral gain equal to 1000.

5.4.3 Case g

In this case, the VI is implemented with a PI controller alongside a dead zone for reacting to frequency. Figure 5.26 demonstrates the model:

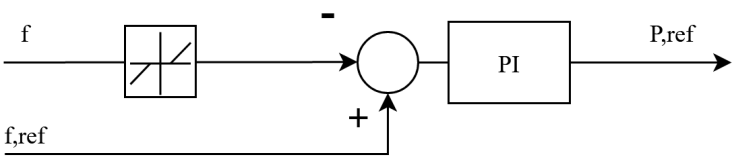

Figure 5.26: Case g- Virtual inertia provision with PI controller and dead zone

where, k_P and k are same as previous case and dead zone is 0.005 pu.

Chapter 6

Simulation Results

In this chapter, the progressions of the model and the case studies (as explained in section 4.3 cases a to c are the progressions and cases d to g are the case studies) developed for the project are presented.

6.1 Case a: Wind turbine drive train and pitch controller (Wind turbine package)

In this section, the simulation results for the wind turbine package are presented separately to validate its operation. All the values are calculated in pu and the operation is tested via changing the feedback rotor speed (W_r) of DFIG as step inputs of 1, 0.9 and 1.1 pu at $t = 0, 20, 55$ seconds. The same model as figure 5.8 is presented below:

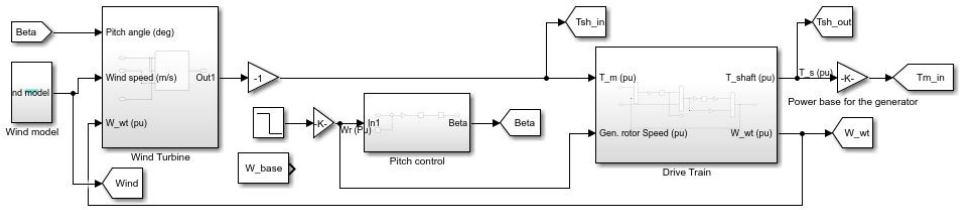

Figure 6.1: Wind turbine package simulation model

The results of the simulation indicates that the wind profile oscillates randomly with an average value of 12 m/s (figure 6.3). The turbine successfully tracks the DFIG rotor speed (figure 6.5) and its oscillations are damped according to damping designed in the drive train. The pitch angle (figure 6.4) changes and at first accelerates the turbine (as expected and seen in figure 6.5) by increasing the pitch angle and reducing the output torque/power of the turbine. If the speed reference would have remained at 1.1 pu for a longer period, the pitch angle would continue to increase until maximum pitch angle of 45 degrees and after that the turbine

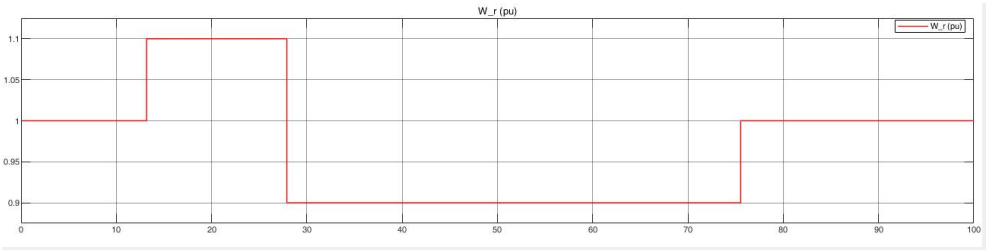

Figure 6.2: DFIG rotor speed reference (Wind turbine package simulation model)

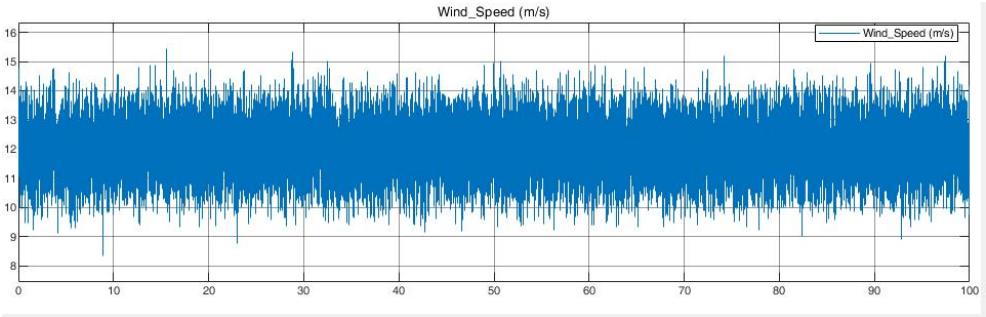

Figure 6.3: Wind profile, (Wind turbine package simulation)

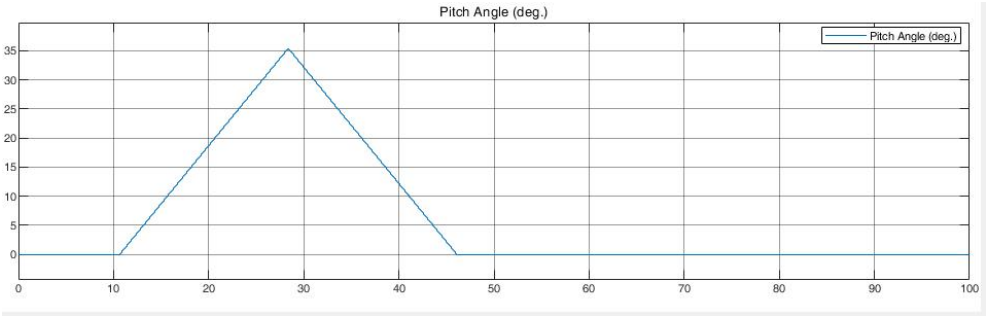

Figure 6.4: Pitch angle, (Wind turbine package simulation)

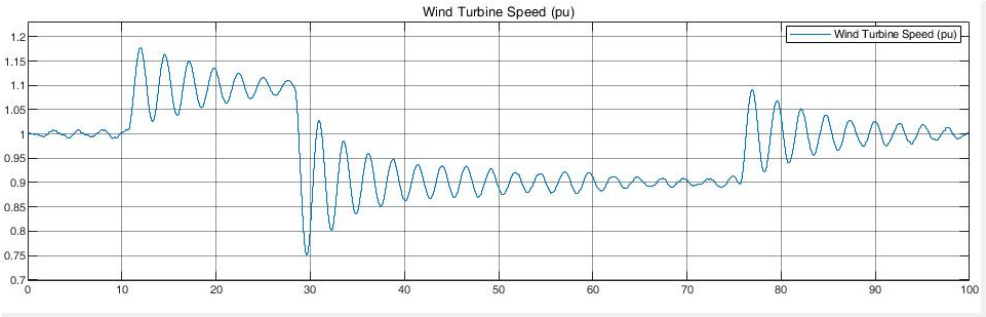

Figure 6.5: Wind turbine speed, (Wind turbine package simulation)

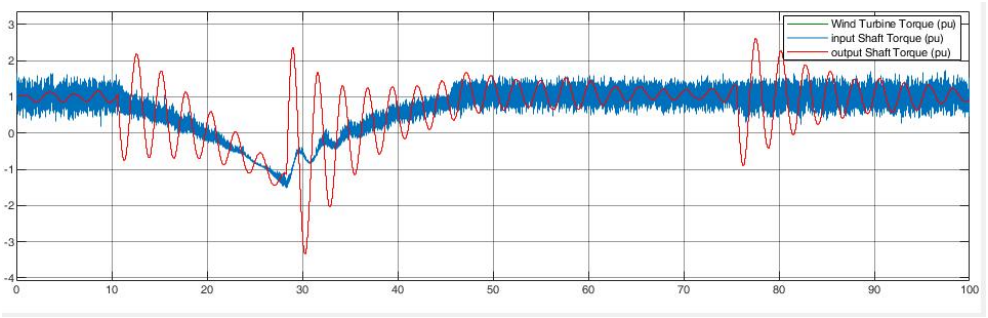

Figure 6.6: Shaft input and output torque, (Wind turbine package simulation)

would be unable to track the reference signal. After lowering the rotor reference speed to 0.9 pu, the pitch controller starts braking the turbine (figure 6.4) and increasing the toque/power. Note that in figure 6.6 the input shaft torque and wind turbine torque are the same signals (wind turbine torque is sketched from internal signal in wind turbine package). The output shaft torque has some oscillation which are damped in the drive train.

Note that in reality, according to the pitch control, nominal value of the wind turbine and restrictions of safety and manufacturing (considering both wind turbine and DFIG have the same nominal power), the wind turbine is unable to produce power which exceeds its nominal value for a long time but it is capable of braking to reduce its output power. Additionally, if the DFIG is exceeding its nominal rotor speed, the wind turbine coupled with the generator should not inject more power, since it will speed up the generator even more and makes it unstable.

The results of the simulation shows that the wind turbine follows the DFIG not the other way around while at the same time, the DFIG rotor speed is controlled with the power converters. Additionally, figure 6.6 shows that with this designed turbine the input mechanical torque signal of the DFIG system will be oscillatory even if the reference speed is constant. This might cause oscillatory output power for the DFIG and depending on the accepted ripple for the output (if accepted at all), the design of the wind turbine should be changed. This issue is investigated further after simulation of the DFIG and examining the output power.

6.2 Case b: DFIG only with RSC

6.2.1 Case b1: PI controller and wind turbine package

The DFIG is loaded with the shaft torque (output of case a) coupled with the wind turbine and the electrical load of the platform. To simulate the model, a three phase voltage is connected directly to the output terminals of the DFIG. The PI controller is responsible for controlling the speed of the DFIG and generating the current reference as explained in subsection 5.3.5.5. Figure 6.7 illustrates model of case b1. The simulation aims to test the capability of the controllers to control the dq currents and speed of the DFIG for the nominal values of the DFIG.

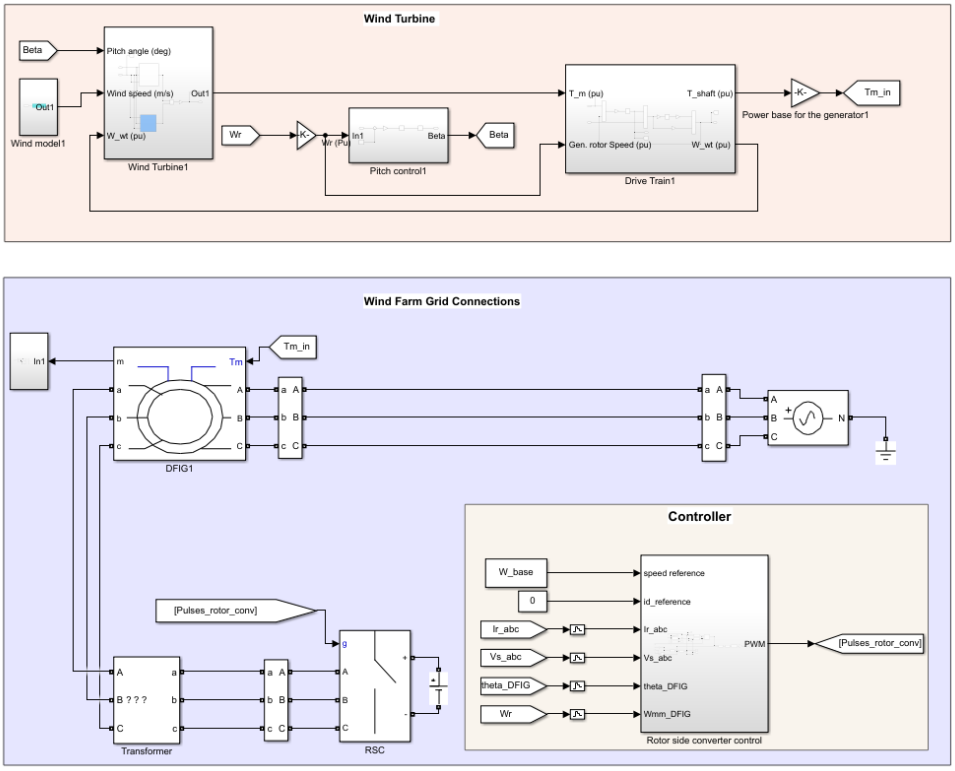

Figure 6.7: Case b1 simulation model

Figure 6.8 shows that the wind speed is successfully generated with random distribution and an average value of 12 m/s. Figure 6.9 illustrates the speed of the wind turbine which is approximately 1 pu with minor oscillations and figure 6.10 shows how the pitch controller is functioning in respond to changes from the DFIG rotor speed. The changes in the pitch angle are not substantial and is in accordance with the wind turbine speed that does not change much. Figure 6.11 shows that the output torque of the shaft which is the input signal of the DFIG is oscillating around 1 pu. Note the wind turbine and input shaft torques are the same (it is trivial because the same wind turbine package of case a is used) but they os-

cillate considerably due to the nature of the variable wind speed. The drive train is successfully damping these oscillations and giving a much smoother signal as the output. Fig 6.12 is the same signal of the output shaft torque but in physical units (N.m). This almost constant torque enables the DFIG to provide an output power with presumably low oscillations. It has to be checked that if the power oscillations are acceptable with this design or not.

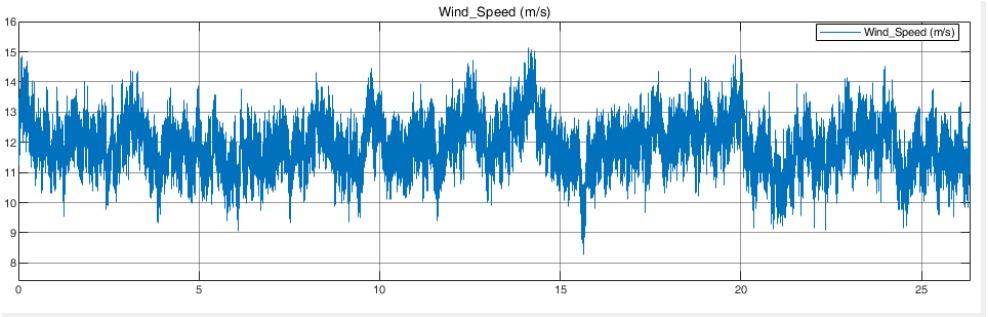

Figure 6.8: Case b1- Wind speed (m/s)

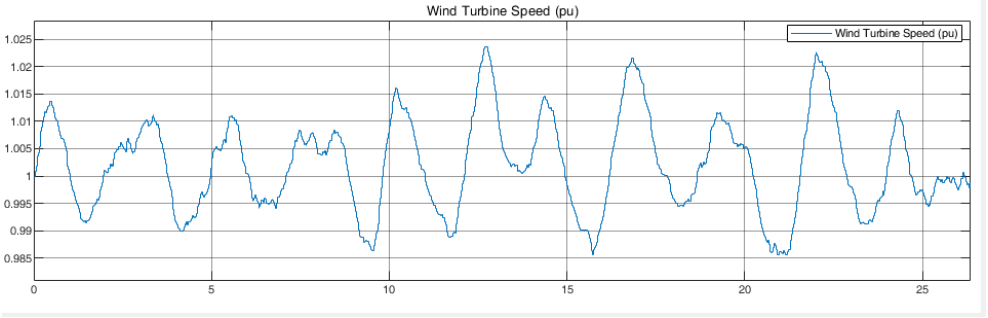

Figure 6.9: Case b1- Wind turbine speed (pu)

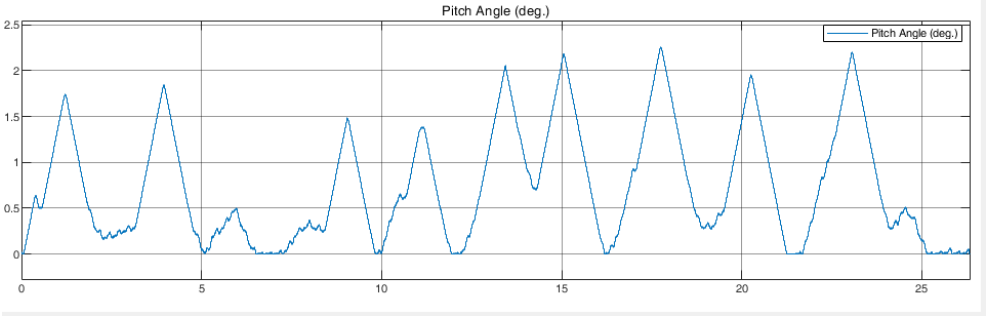

Figure 6.10: Case b1- Pitch angle (deg)

Figure 6.13 shows the rotor speed of the DFIG with a desired nominal value

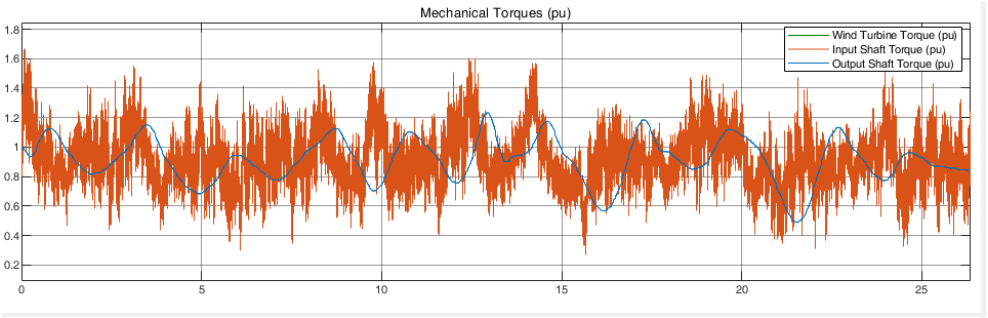

Figure 6.11: Case b1- shaft torque (pu)

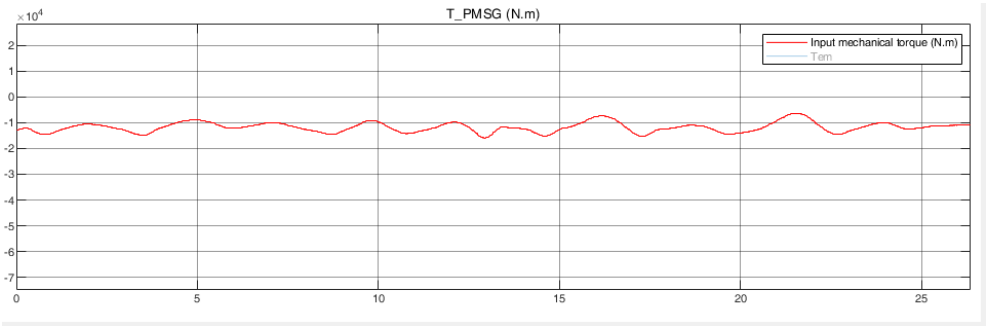

Figure 6.12: Case b1- Mechanical input torque of generator (N.m)

of 155 rad/s. The PI speed regulator tracks the 155 reference signal quite acceptable with minor deviations that do not exceed 5 rad/s. These deviations occur as the input mechanical torque signal of the DFIG is not constant and has small oscillations. Since the PI speed regulator functions correctly, the current regulators have the correct reference signals as depicted in figure 6.14 and 6.15 in red colors (note that d axis reference current was set to zero). These figure also indicate that the designed PI controllers for currents are also preforming well. Although the design could have been changed to have lower ripples which is a trade off in design between the costs and the performance. The stator and rotor current are presented in figures 6.16 and 6.17 which indicate that with the given sinusoidal voltage at the PCC, the DFIG produces almost sinusoidal currents, which again correspond to the current regulators and their performance. A filter can also be added to the system which is considered from case c forward.

With these performances, the DFIG output the electromagnetic torque of figure 6.18 which is following its reference. This fluctuating torque was expected as the input torque of the DFIG was also oscillatory and the reason for that was mainly the variable wind speed. In practice, the grid codes force the power quality attribute to the wind farm operators and the fluctuations are compensated by the grid because the grid is considerably stronger. With the recent advancements in the offshore wind turbine technology and increased size of the turbines the shaft

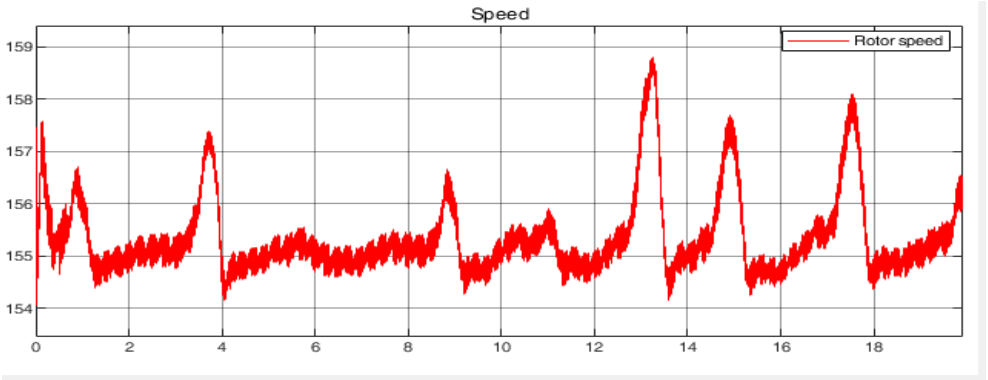

Figure 6.13: Case b1- Rotor speed (rad/s)

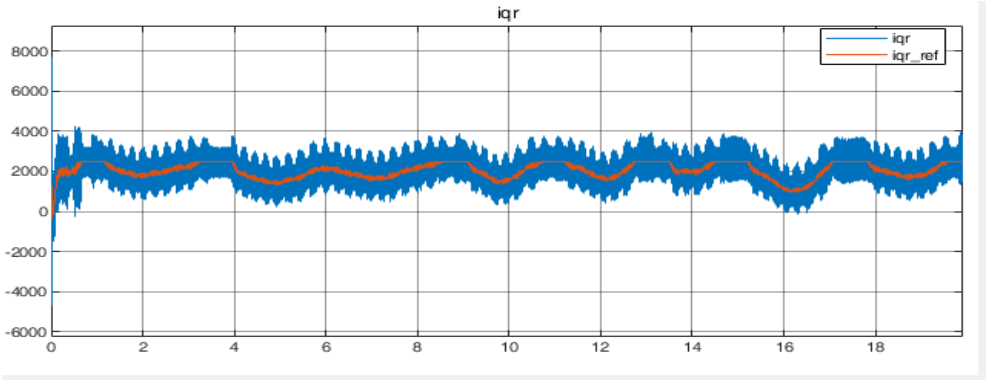

Figure 6.14: Case b1- q axis RSC current (A)

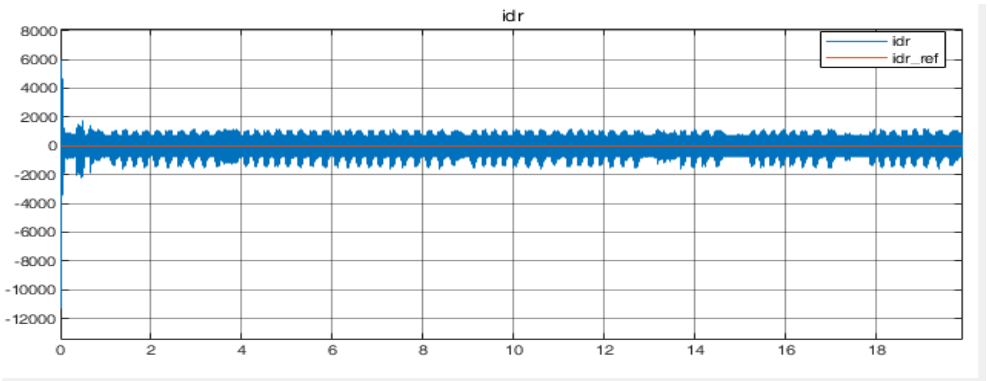

Figure 6.15: Case b1- d axis RSC current (A)

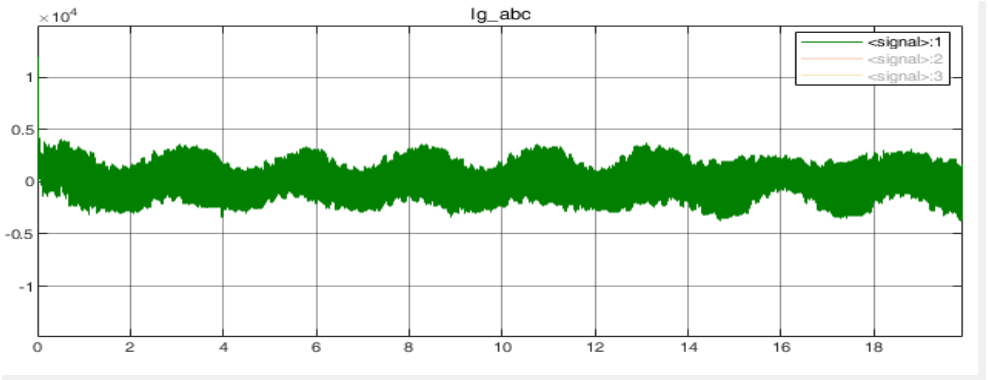

Figure 6.16: Case b1- stator current (A)

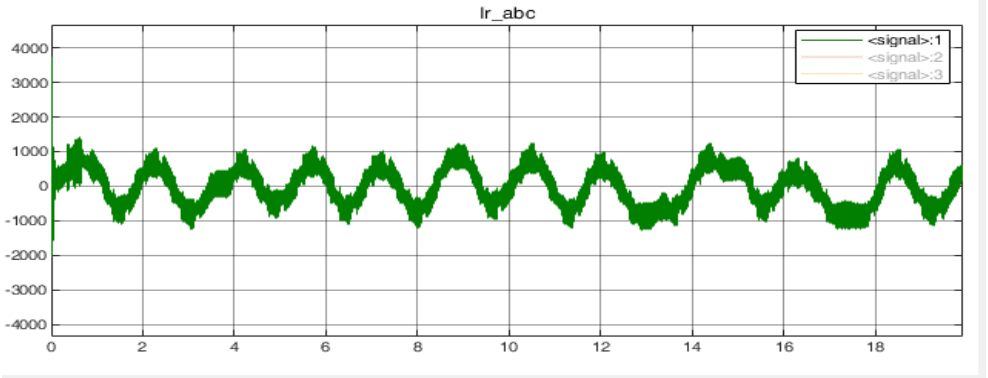

Figure 6.17: Case b1- rotor current (A)

toque is even less oscillatory because of the high mass and inertia of the turbine which enables the turbine to operate at the nominal values and nullifying the effect of the variable wind speeds.

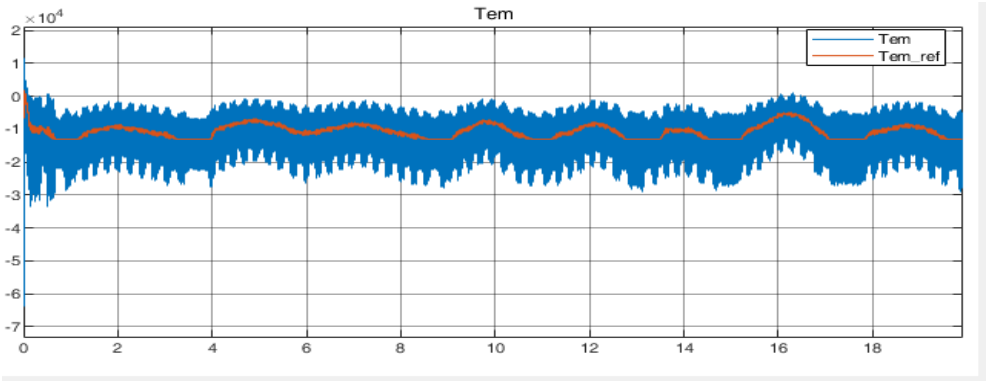

Figure 6.18: Case b1- Electromagentic torque (N.m)

6.2.2 Case b2: MPPT and Simplified wind turbine model

The same scenario as in case b1 with some changes is tested. Instead of the PI speed regulator the MPPT algorithm of subsection 5.3.5.6 is used on the simplified wind turbine model of subsection 5.3.3. The controller focuses on extracting maximum power form the generator while the wind speed is constantly changing and the rotor speed is controlled indirectly. Additionally, the nominal power of the wind turbine and DFIG are considered to be 2.4 MW instead of 2MW and the nominal rotor speed is 200 m/s instead of 155 rad/s (these changes are explained in the next paragraph). The simulation aims to test the effectiveness of the MPPT algorithm in comparison with the PI speed regulator. The model developed in this case is presented in figure 6.19.

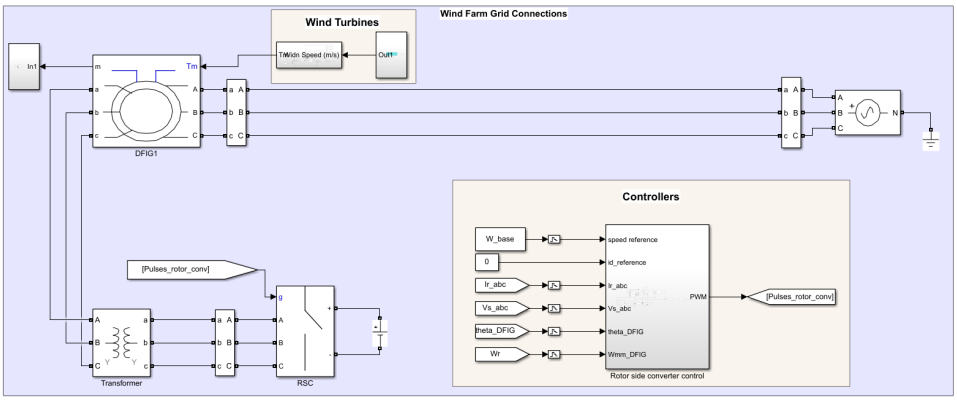

Figure 6.19: Case b2 simulation model

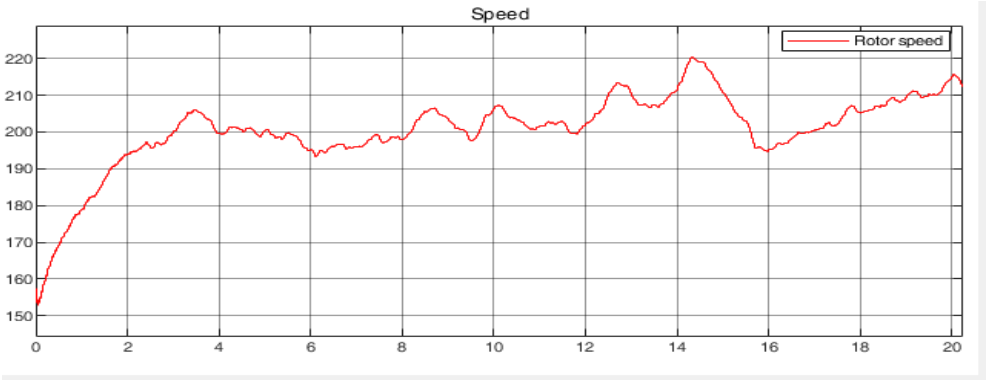

Figure 6.20: Case b2- Rotor speed (rad/s)

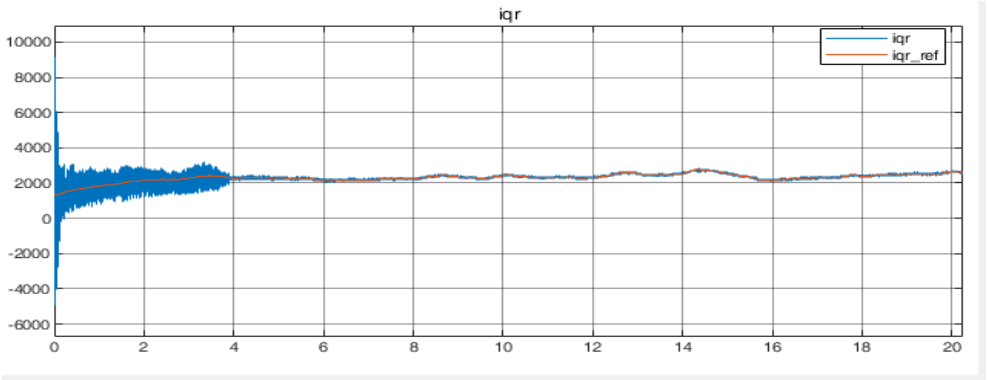

Figure 6.21: Case b2- q axis RSC current (A)

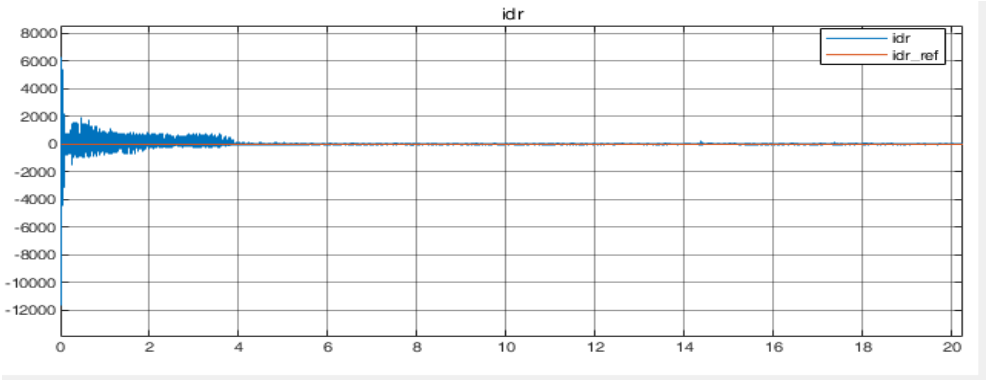

Figure 6.22: Case b2- d axis RSC current (A)

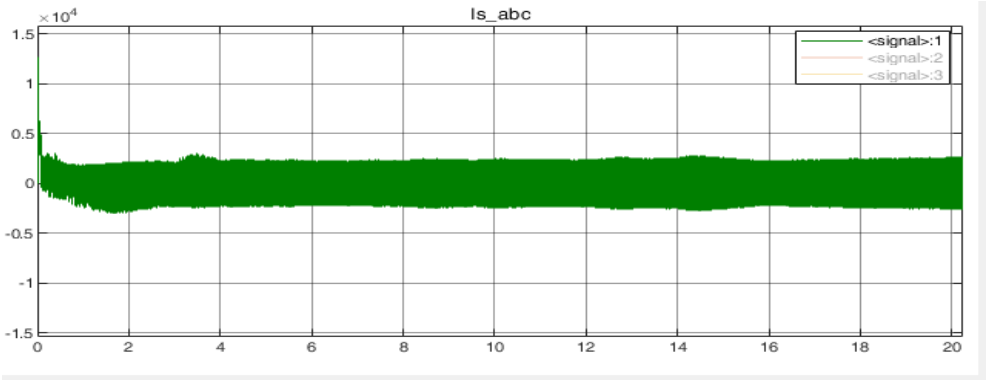

Figure 6.23: Case b2- stator current (A)

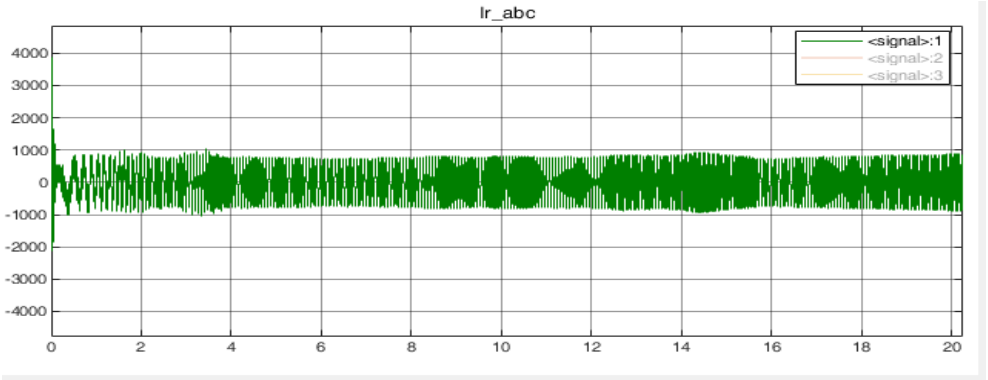

Figure 6.24: Case b2- rotor current (A)

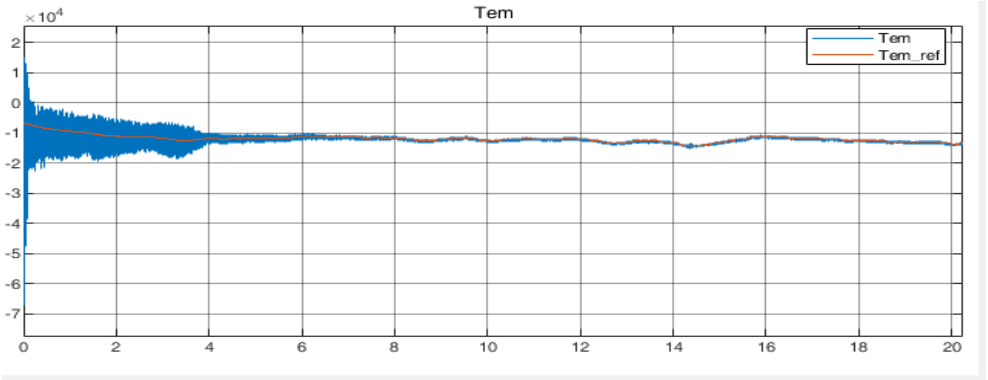

Figure 6.25: Case b2- Electromagentic torque (N.m)

Figure 6.20 shows the rotor speed of the DFIG and it takes about 4 seconds for the simulation transients to finish and the system operate around its nominal values after 4 seconds. The reason for these transients is that the initial rotor speed of the DFIG was set to 155 rad/s from previous simulation and it was not changed in this case, while the nominal speed in this case is 200 m/s. This is because the simplified wind turbine model of case b2 has a 2.4 MW nominal power at an average wind speed of 12 m/s (because the power curve data for a 2 MW was not found while the data of a 2.4 MW was found as shown in figure 5.16), however the wind turbine package in case b1 has the nominal power of 2 MW at the same wind speed. Therefore, the DFIG rotor speed reaches a higher value in case b2 compared to case b1 (These transients and higher nominal rotor speed would not have happened if the initial condition of the DFIG and the rated power of the wind turbine were kept the same but they were not kept the same because the MPPT was aimed to be tested even if the initial rotor speed was not the nominal value. It is evident that the DFIG was not started from zero speed because with the design values it would have taken a considerable amount of time for it to reach nominal values and the computational restrictions of the PC in which the model was built, would not allowed it). The simplified wind turbine model of case b2 with MPPT which has a nominal power output of 2.4 MW at an average wind speed of 12 m/s, gives 2 MW power at average wind speed of 11 m/s. Hence, if the wind profile is generated with average value of 11 m/s and given as input to the wind turbine model instead of 12 m/s, the problem is solved. Other then the the explained issue, after 4 seconds of transients in the beginning of the simulation, the rotor speed oscillates around its nominal value of 200 rad/s with minor changes of up to 20 rad/s and the reason for these oscillations is the variable wind speed profile.

The PI regulators for dq currents were the same as previous case and they have the correct reference signals as depicted in figure 6.21 and 6.22 in red colors (note that d axis reference current was set to zero). These figure also indicate that the designed PI controllers for currents are also preforming well and in fact much better than the case b1. The stator and rotor current are presented in figures 6.23 and 6.24. The MPPT directly changes the input torque of the generator to extract maximum power at each wind speed. Figure 6.25 shows that the reference for electromagnetic torque is followed with less deviations compared to the previous case. In a nutshell, cases b1 and b2, in case b1 a wind turbine of 2 MW was used, while in case b2, wind turbine has 2.4 MW rated power. The difference is also reflected in rotor speed. in case b2 the MPPT track the maximum power at each wind speed and controls the torque directly and rotor speed indirectly while case b1 is the opposite. Case b2 shows a more promising result than case b1 and has a more stable electromagnetic torque.

6.3 Case c: DFIG with RSC and GSC

The previous cases b1 and b2 analysed the difference of each control strategy for DFIG RSC. In cases c1, c2 and c3 the effect of these control methods are investigated while interacting with GSC, its controller and the other added elements in the system and after the simulation, the final model for wind turbine is selected. Note the replacement of the DC voltage source with the DC link capacitor.

6.3.1 Case c1: PI controller with variable wind speed and wind turbine package

For this analysis, the same structure as in case b1 (average wind speed of 12 m/s, wind turbine size of 2 MW) is used while adding the GSC and its controller, the DC link capacitor and the GSC filters as shown in figure 6.26.

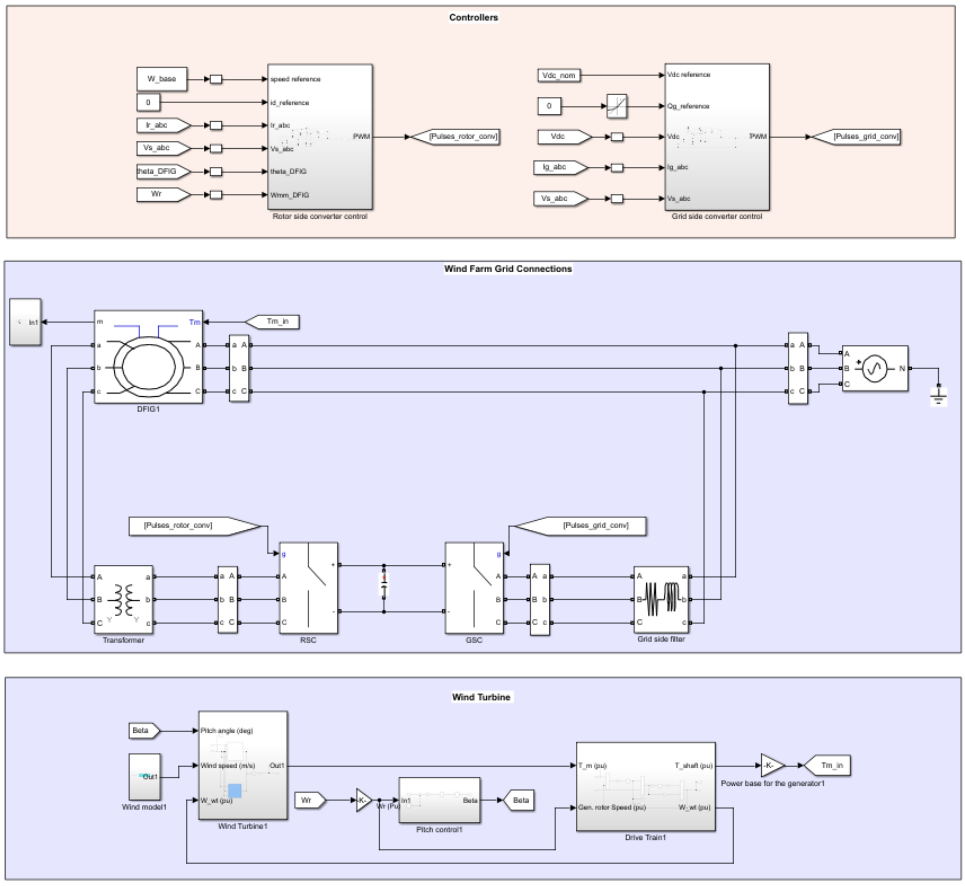

Figure 6.26: Case c1 simulation model

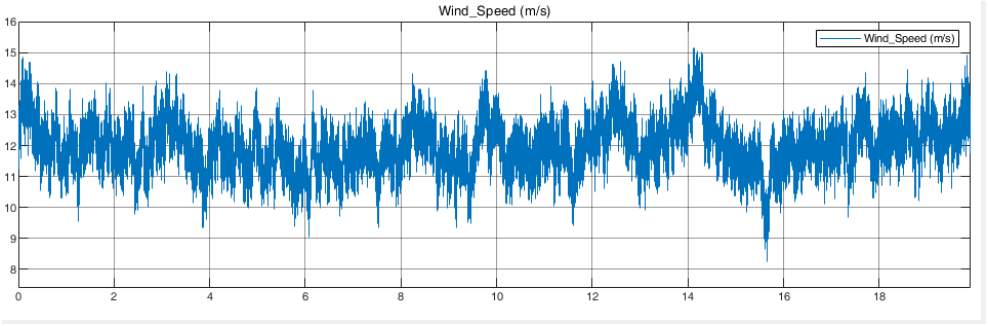

Figure 6.27: Case c1- Wind speed (m/s)

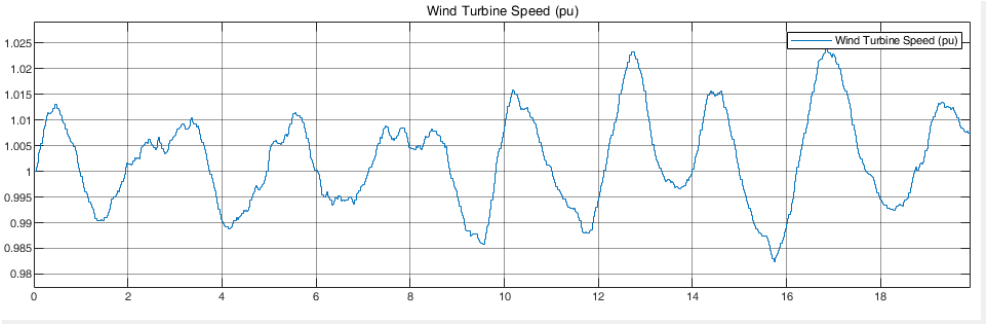

Figure 6.28: Case c1- Wind turbine speed (pu)

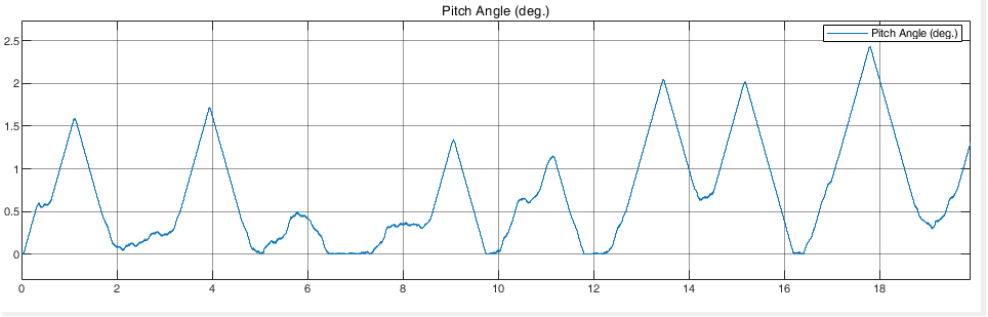

Figure 6.29: Case c1- Pitch angle (deg)

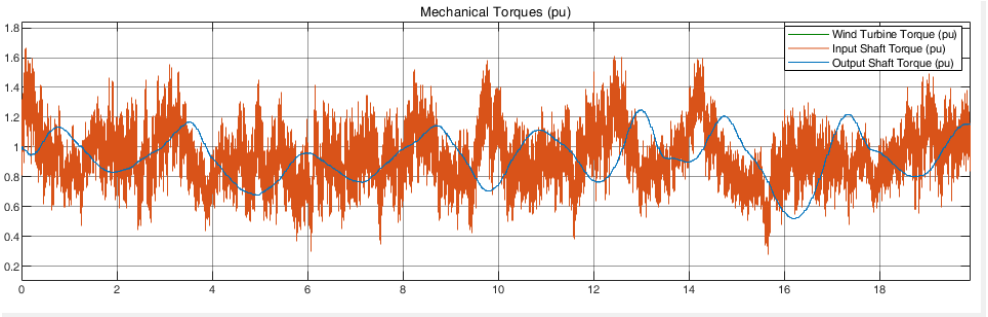

Figure 6.30: Case c1- shaft torque (pu)

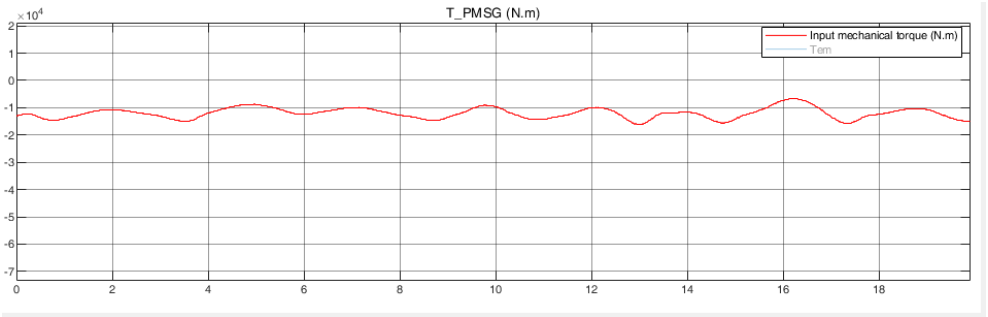

Figure 6.31: Case c1- Mechanical input torque of generator (N.m)

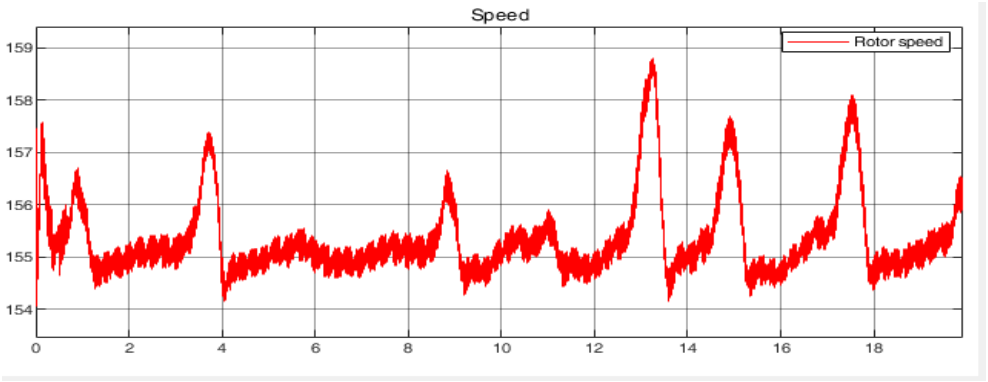

Figure 6.32: Case c1- Rotor speed (rad/s)

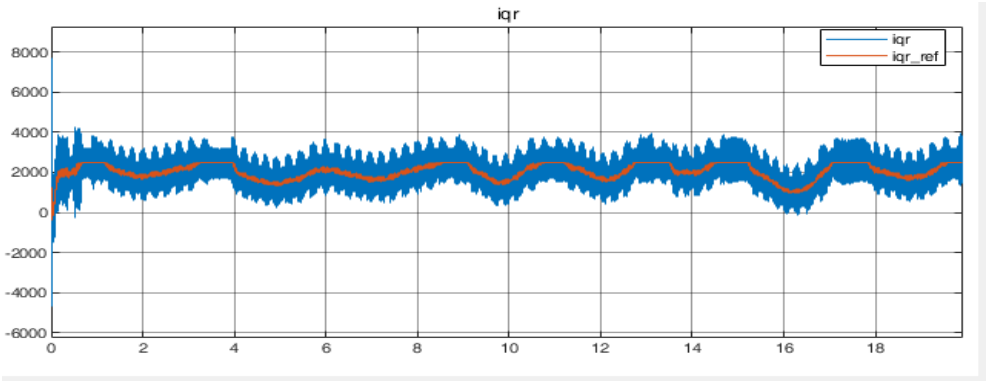

Figure 6.33: Case c1- q axis RSC current (A)

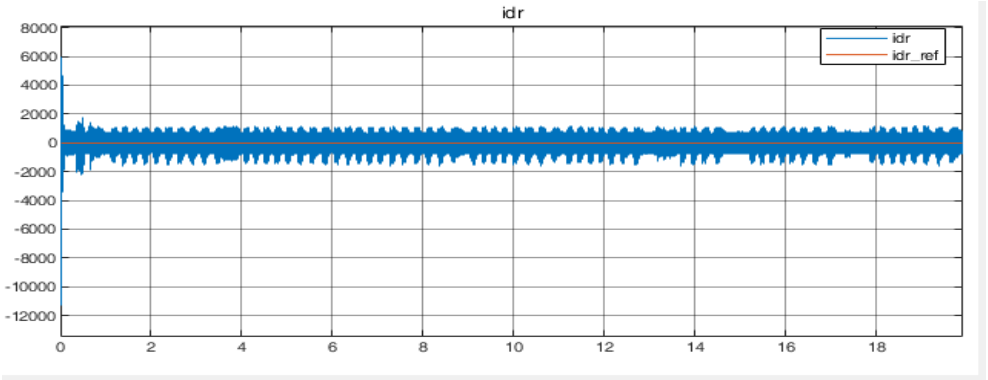

Figure 6.34: Case c1- d axis RSC current (A)

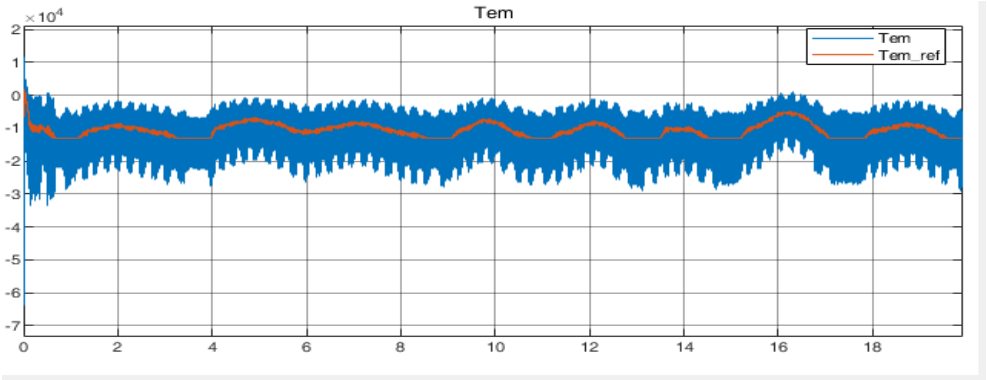

Figure 6.35: Case c1- Electromagentic torque (N.m)

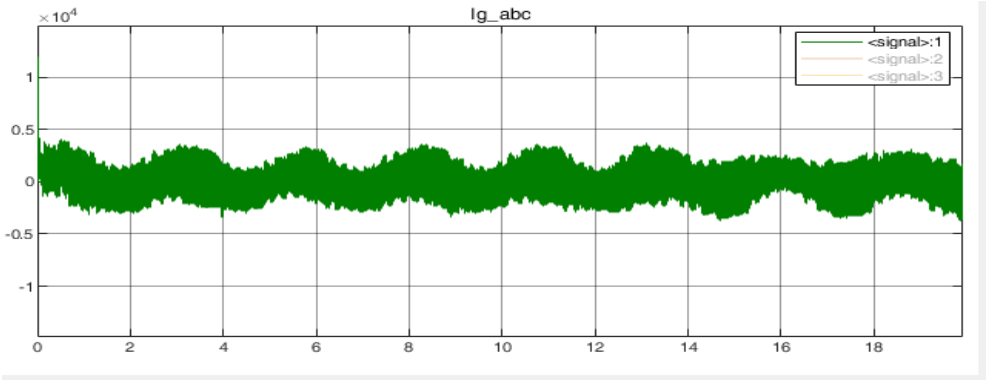

Figure 6.36: Case c1- stator current (A)

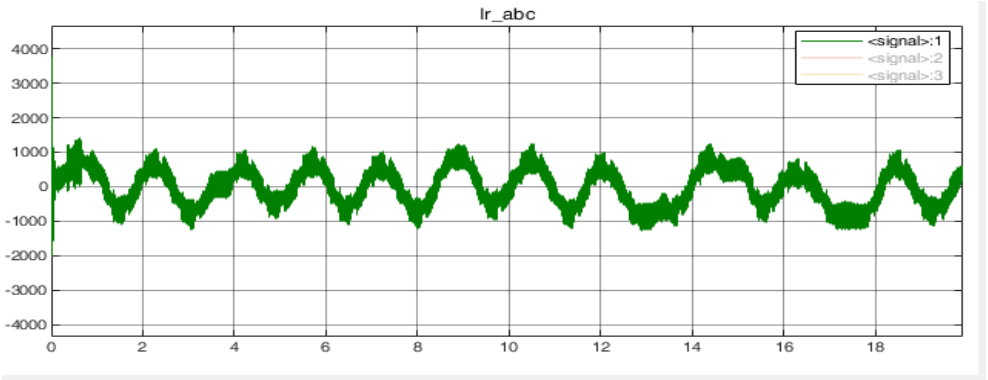

Figure 6.37: Case c1- rotor current (A)

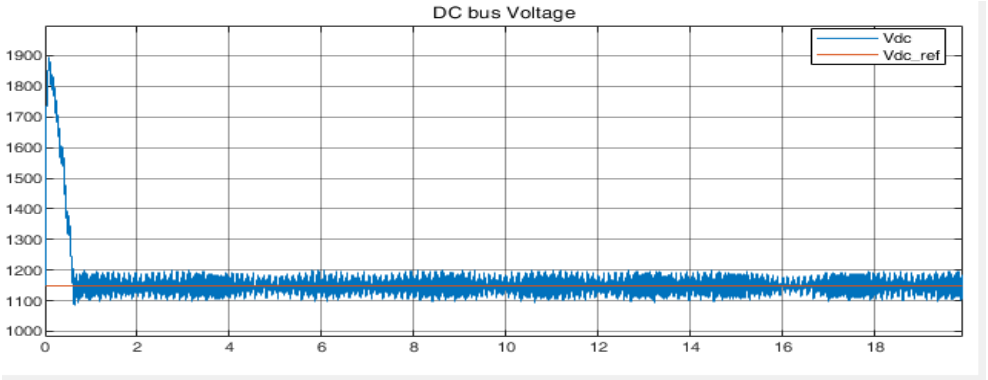

Figure 6.38: Case c1- DC link voltage (V)

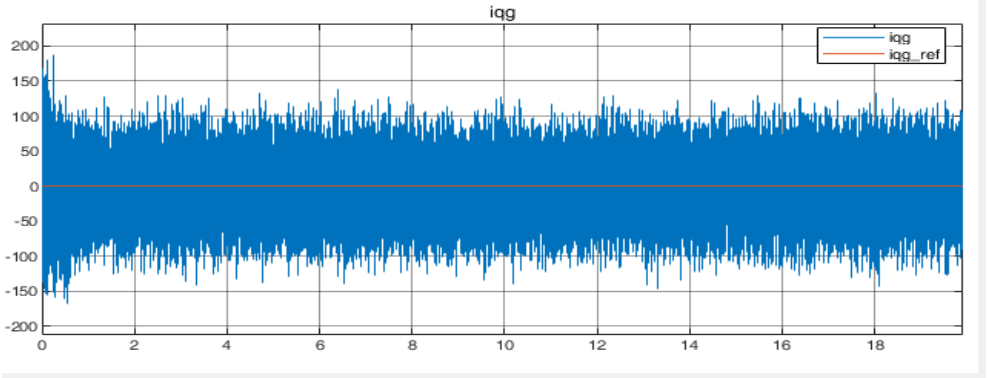

Figure 6.39: Case c1- q axis GSC current (A)

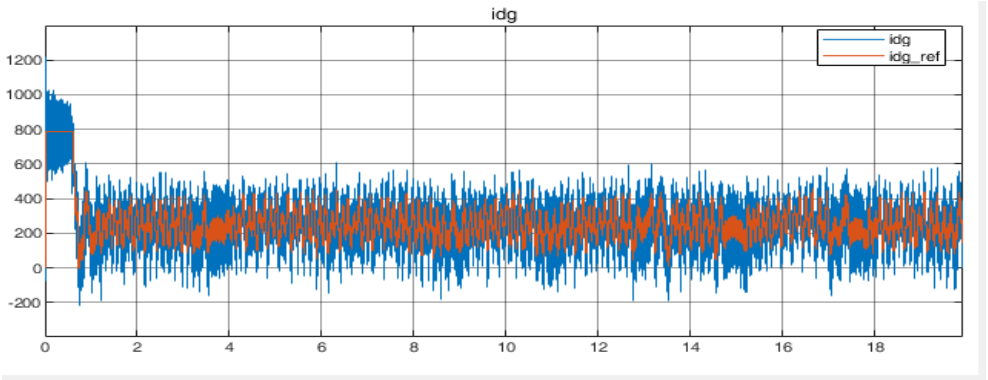

Figure 6.40: Case c1- d axis GSC current (A)

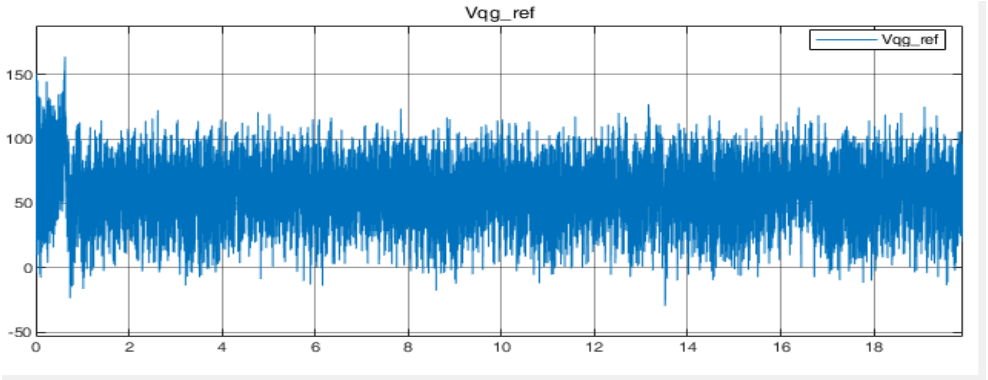

Figure 6.41: Case c1- q axis GSC voltage (V)

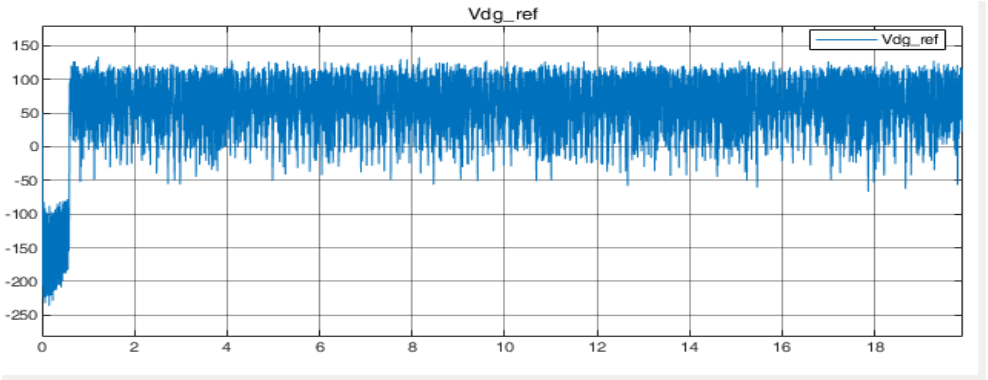

Figure 6.42: Case c1- d axis GSC voltage (V)

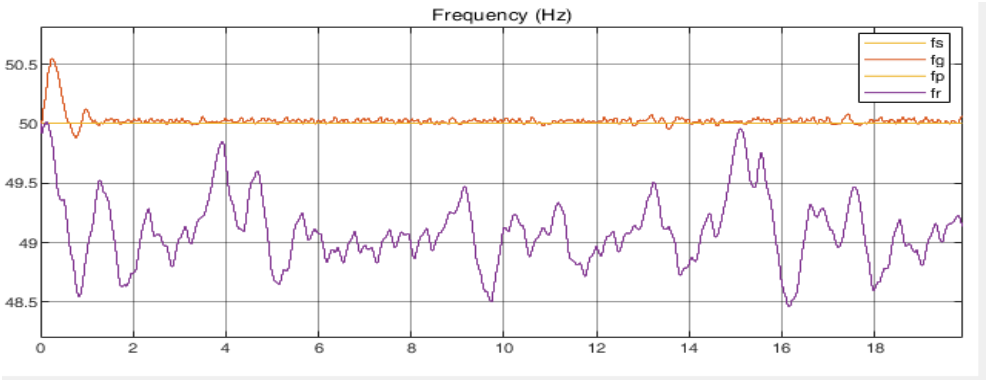

Figure 6.43: Case c1- rotor (purple), stator (red), and grid (yellow) voltage frequency

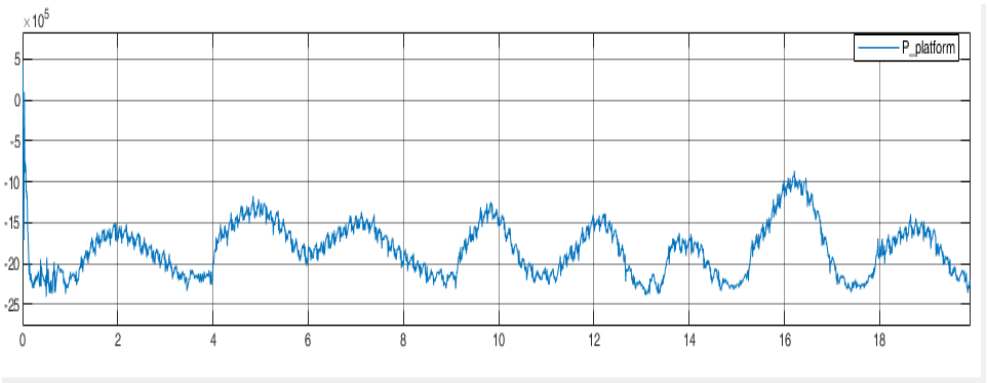

Figure 6.44: Case c1: power delivered to the load (W)

Figures 6.27 to 6.37 indicate the exact same results as of in case b1. These figures are sketched for the RSC controller parameters and only are presented to show the correct interaction of the RSC while connected to GSC and therefore, require no further explanation. The RSC controller is able to perform correctly only when the GSC controller is operating well and provides it with the suitable DC link voltage. This DC link voltage must be almost constant around the operating designed value. Hence, the RSC controller sees this DC link capacitor as a constant voltage source. Figure 6.38 illustrates the DC link voltage. After the initial simulation transients of around 0.75 seconds the DC voltage regulator, which is a PI controller, tracks the reference value of 1150 V with ripples no more than 100 V. Figures 6.39 and 6.40 illustrate the d and q axis currents of the GSC. The currents have the correct references because the outer layer controller (Dc voltage controller) operates correctly. Figures 6.41 and 6.42 show the voltages generated after the decoupling terms which will be given to the PWM generator after conditioning. Figure 6.43 depicts the frequency of the rotor, stator, grid and platform frequencies. The stator and platform frequencies are measured form the same signal and they are identical. The grid frequency is the frequency of the GSC voltage whcih is equal to the stator and platform frequencies. The rotor frequency is the RSC voltage frequency which is lower then the stator frequency and in accordance with the DFIG slip.

This control model as speculated, can not provide constant output power (figure 6.44) and more complications will have to be added to the project to compensate the power and fix it for the 2 MW needed for the load. The reason for irregular power output is the input torque of the generator, as the wind turbine is not operating at its nominal wind turbine speed of 1 pu, the output torque of the shaft which will be the generator input torque, is not constant and therefore, the generator speed can not settle at its nominal value. The results proves that MPPT algorithm might be a better option. Next case examines if the MPPT algorithm gives results in accordance with the aim of the project.

6.3.2 Case c2: MPPT in variable wind speeds and simplified wind turbine

For this analysis, MPPT with simplified wind turbine algorithm is used (average wind speed of 11 m/s, wind turbine size of 2.4 MW) in order for the generator to output 2 MW (according to figure 5.16) and the rest of the elements are similar to case c1 as shown in figure 6.45.

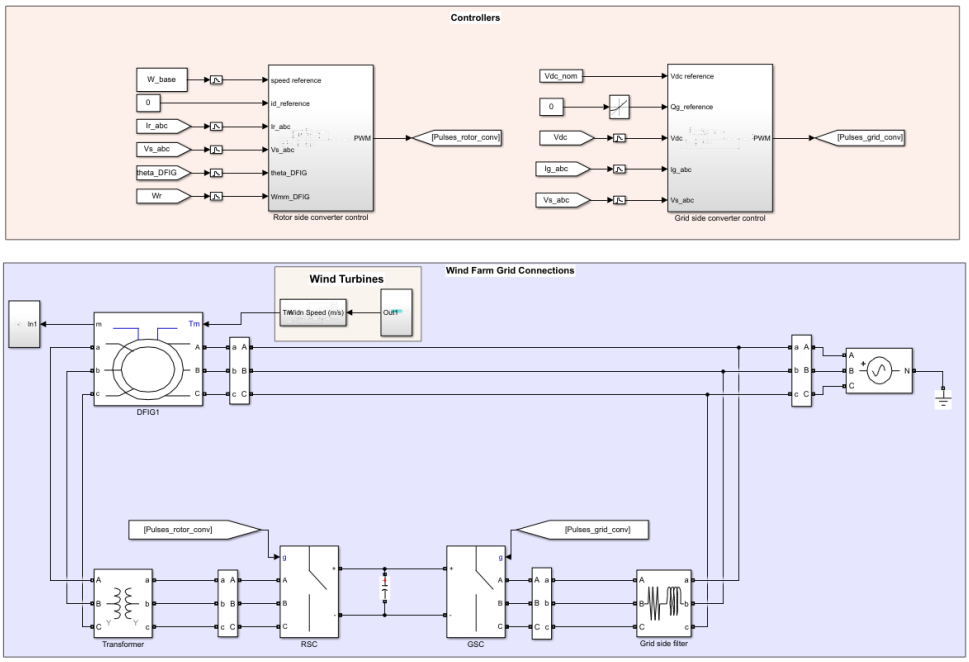

Figure 6.45: Case c2 simulation model

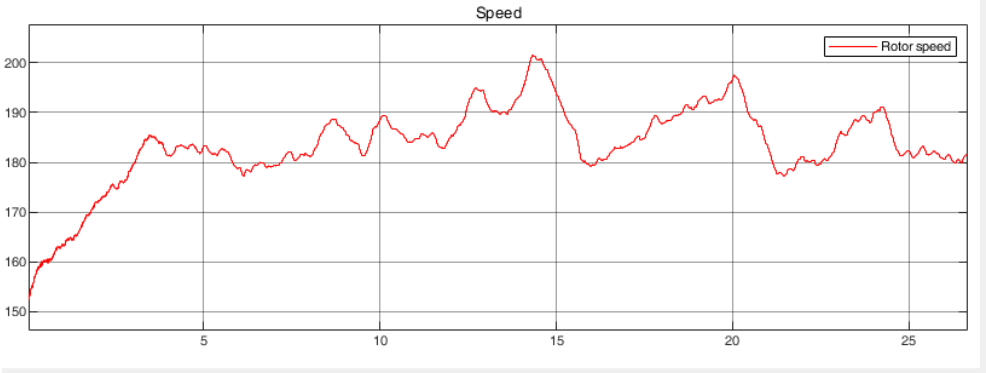

Figure 6.46: Case c2- Rotor speed (rad/s)

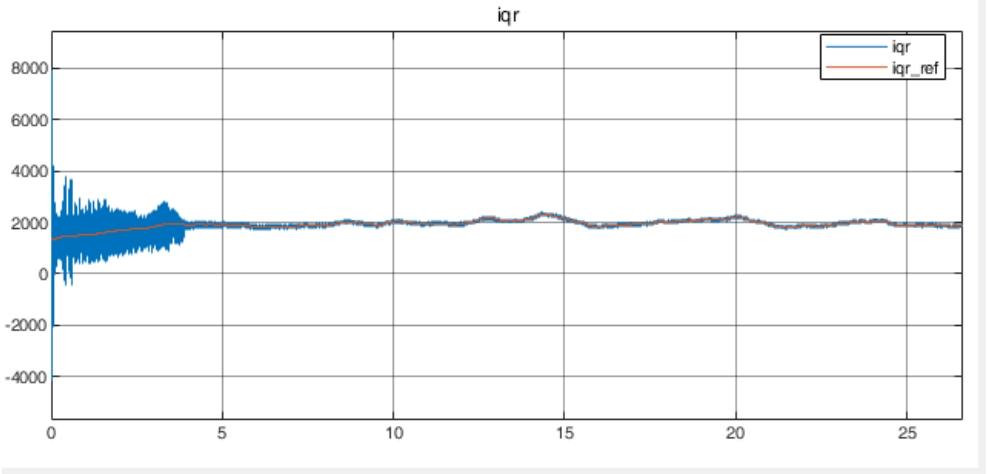

Figure 6.47: Case c2- q axis RSC current (A)

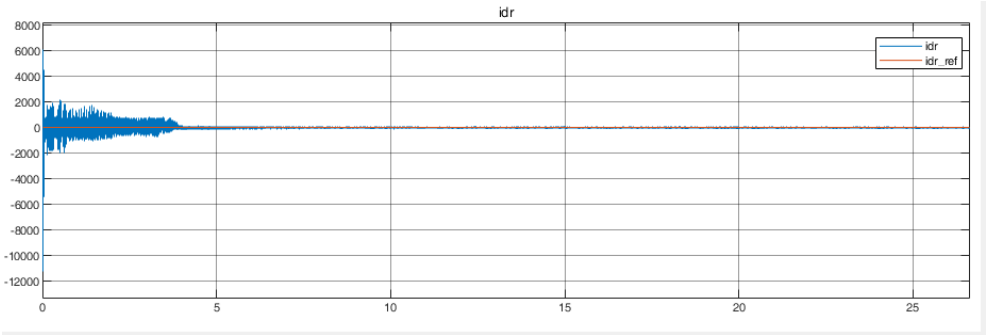

Figure 6.48: Case c2- d axis RSC current (A)

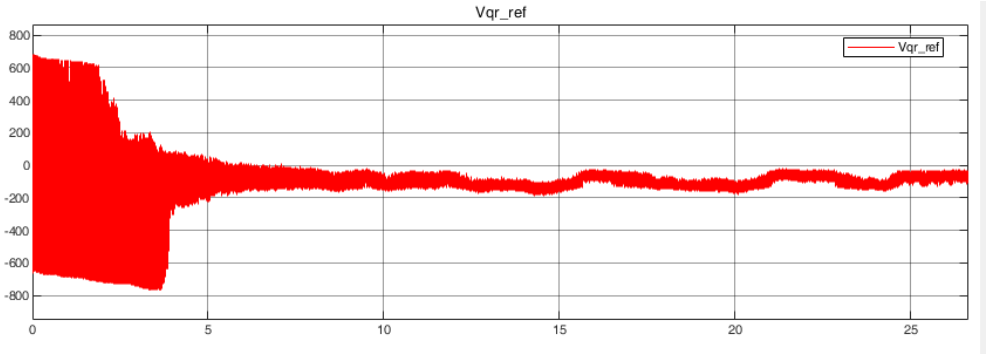

Figure 6.49: Case c2- q axis RSC voltage (V)

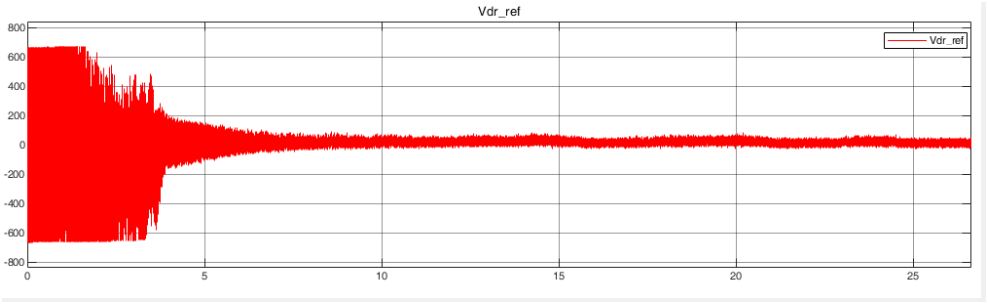

Figure 6.50: Case c2- d axis RSC voltage (V)

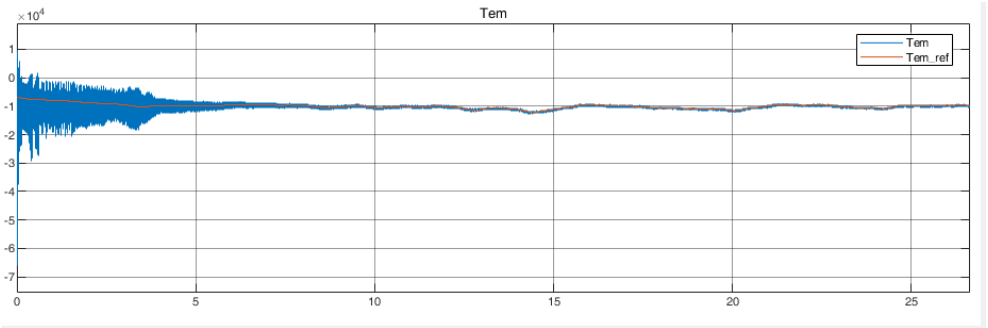

Figure 6.51: Case c2- Electromagentic torque (N.m)

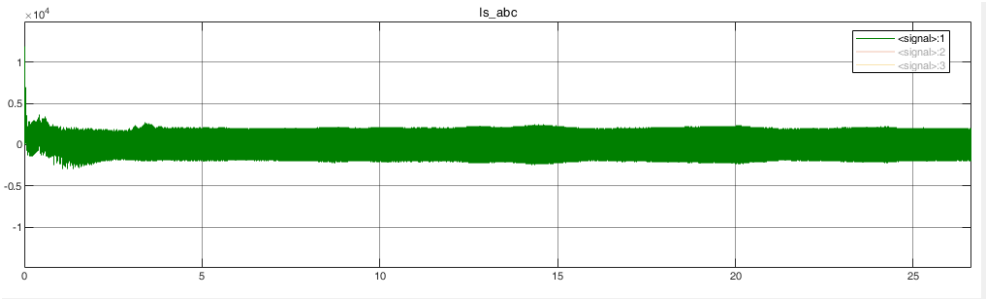

Figure 6.52: Case c2- stator current (A)

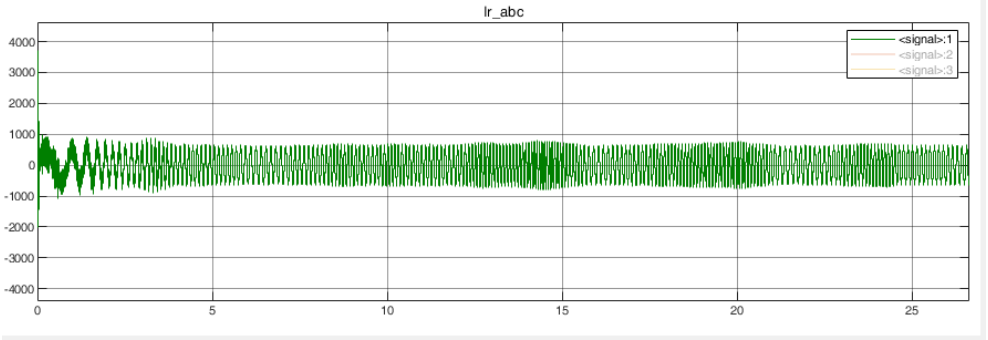

Figure 6.53: Case c2- rotor current (A)

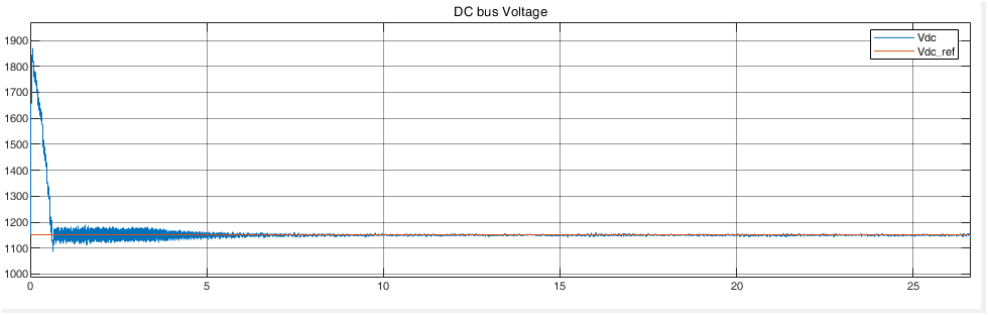

Figure 6.54: Case c2- DC link voltage (V)

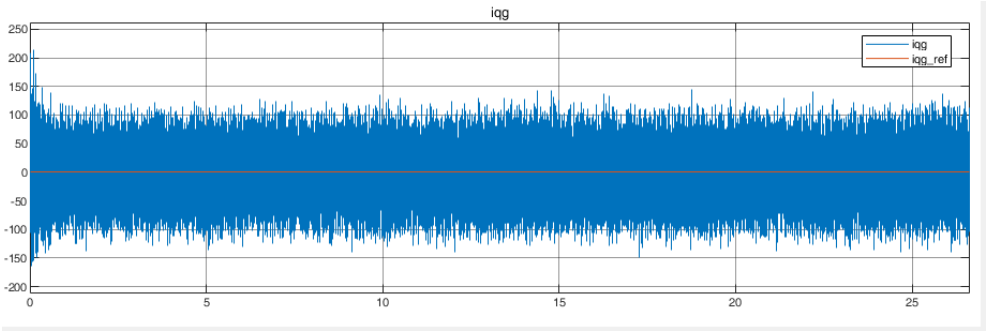

Figure 6.55: Case c2- q axis GSC current (A)

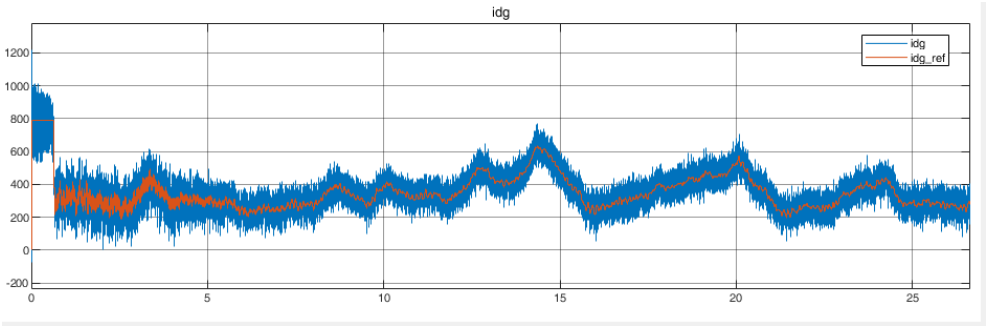

Figure 6.56: Case c2- d axis GSC current (A)

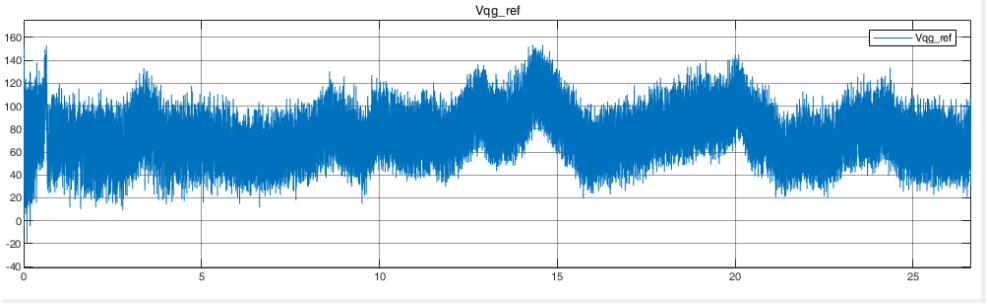

Figure 6.57: Case c2- q axis GSC voltage (V)

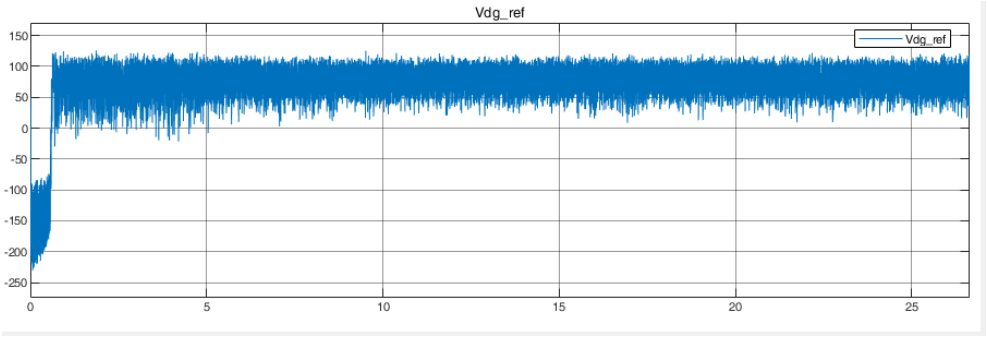

Figure 6.58: Case c2- d axis GSC voltage (V)

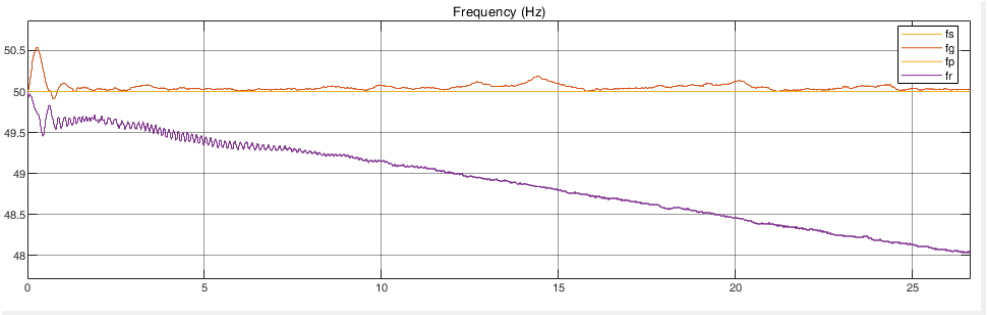

Figure 6.59: Case c2- rotor (purple), stator (red), and grid (yellow) voltage frequency

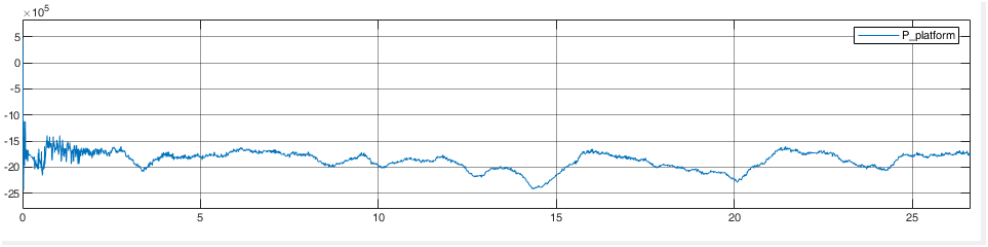

Figure 6.60: Case c2: power delivered to the load (W)

Figures 6.46 to 6.53 indicate achieving similar results as in case b2. These figures are sketched for the RSC controller parameters and only are presented to show the correct interaction of the RSC while connected to GSC and therefore, require no further explanation. Similarly, figures 6.54 to 6.58 show results for the GSC controller which is the same controller in case c1. Hence, the results of the simulation are similar. Although note that the DC link voltage fluctuates quite less than the previous case. For this reason the reference signal for the d axis controller is also less oscillatory and therefore, the current has better quality. Figure 6.59 depicts the frequencies in the system. Similar terminology is used as previous case. The much notable difference is that the fluctuations are less and the rotor speed is decreasing continuously which should settle eventually but due to computational power problems was was not pursued.

The power delivered to the platform fluctuates around the 2 MW desired value (figure 6.60). This was expected as the input wind speed is changing around 11 m/s. Therefore, the MPPT algorithm is continuously changing the input torque signal of the generator leading to generator speed always fluctuating around its steady state value. Therefore, the RSC current references will also fluctuate. It is speculated that if the wind speed is considered constant, the fluctuation are substantially lower and the power output would be much smoother. Next case, examines the effect of constant wind speed.

6.3.3 Case c3: MPPT in constant wind speed and simplified wind turbine

For this analysis MPPT wind simplified wind turbine algorithm is used along constant wind speed input of 11 m/s in order for the generator to output 2 MW (according to figure 5.16). The model is presented in figure 6.61.

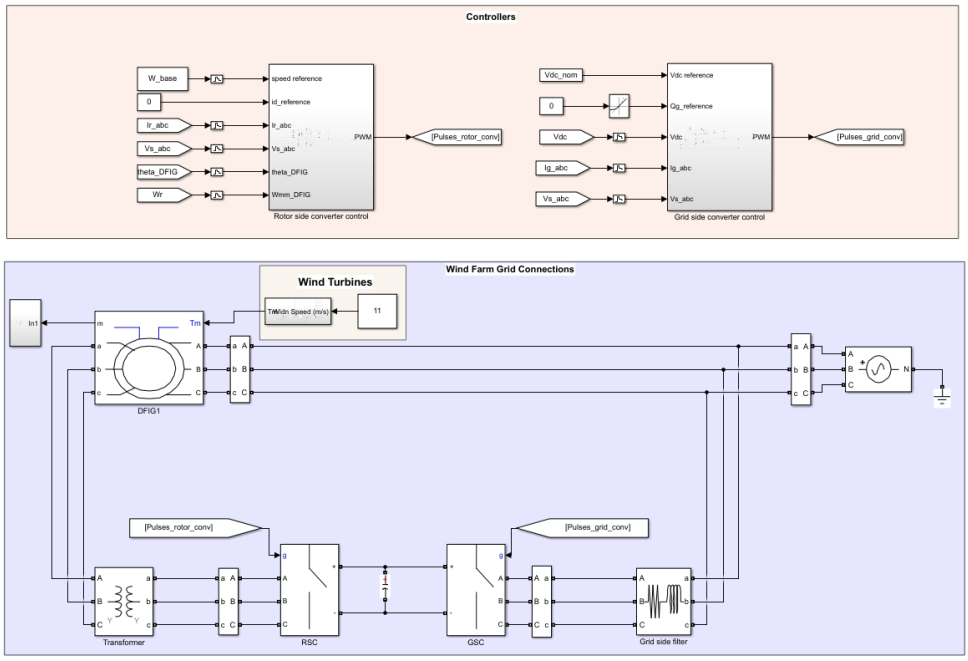

Figure 6.61: Case c3 simulation model

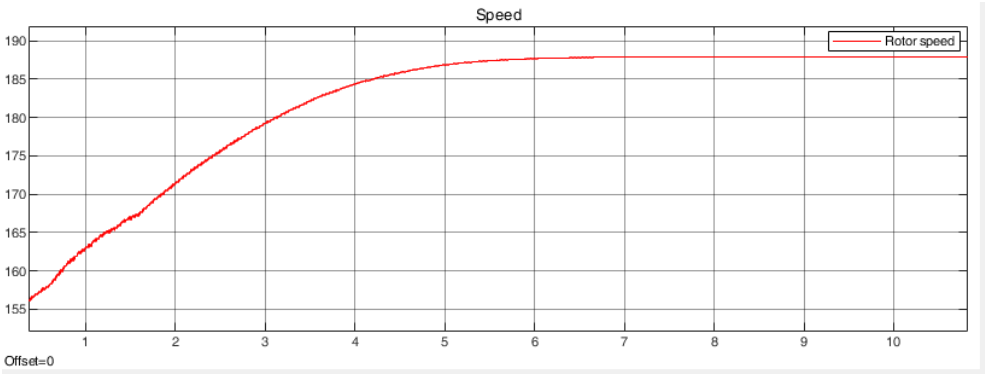

Figure 6.62: Case c3- Rotor speed (m/s)

Figures 6.62 shows that the rotor speed reaches the steady state value after approximately 6 seconds. Note that the initial speed was set to 155 rad/s which in order to check the capability of the MPPT to track the speed indirectly and

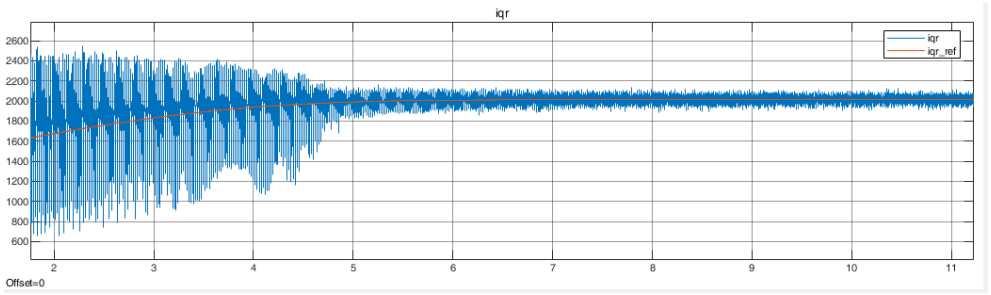

Figure 6.63: Case c3- q axis RSC current (A)

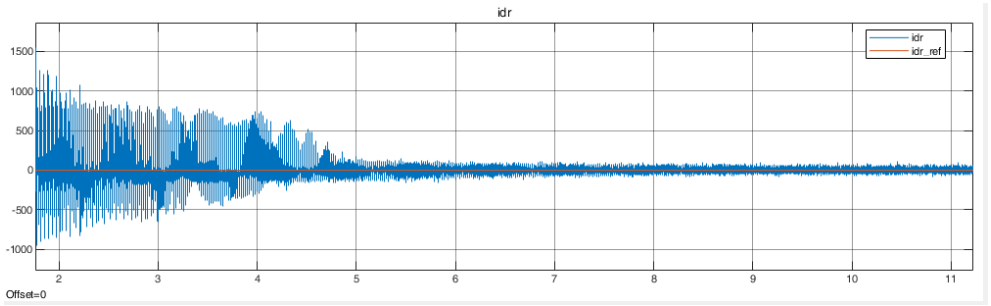

Figure 6.64: Case c3- d axis RSC current (A)

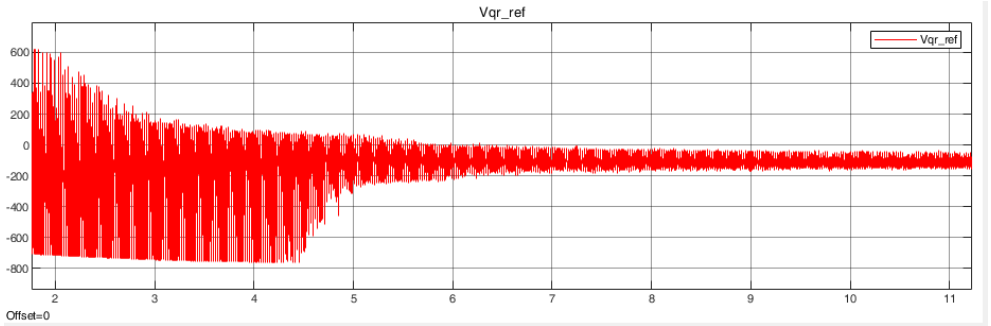

Figure 6.65: Case c3- q axis RSC voltage (V)

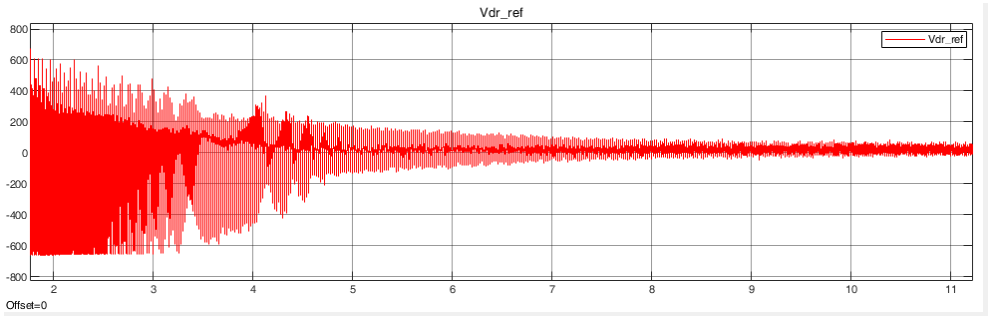

Figure 6.66: Case c3- d axis RSC voltage (V)

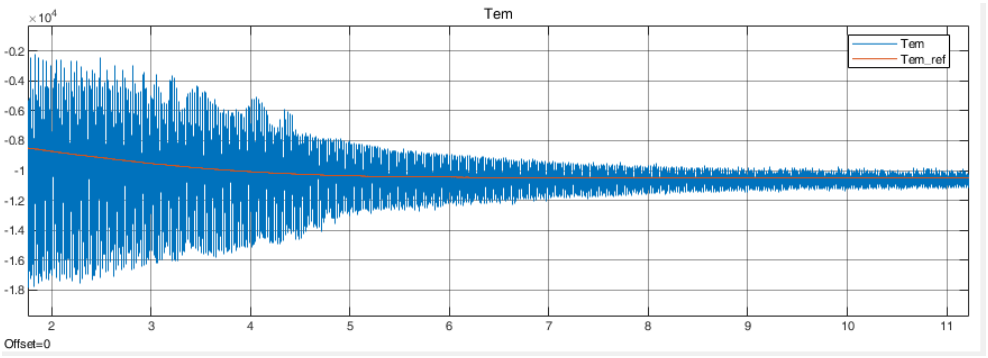

Figure 6.67: Case c3- Electromagentic torque (N.m)

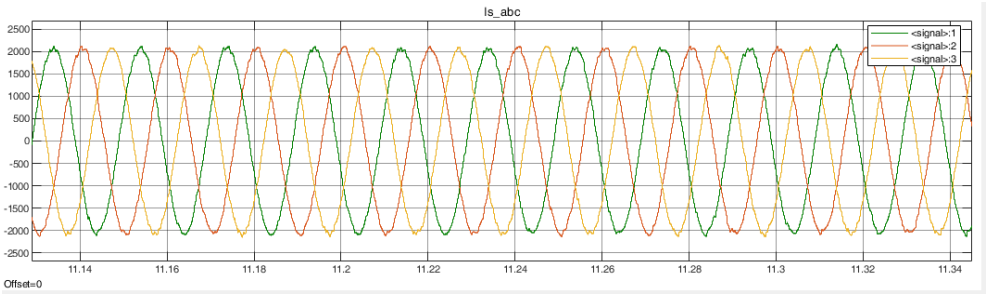

Figure 6.68: Case c3- stator current (A)

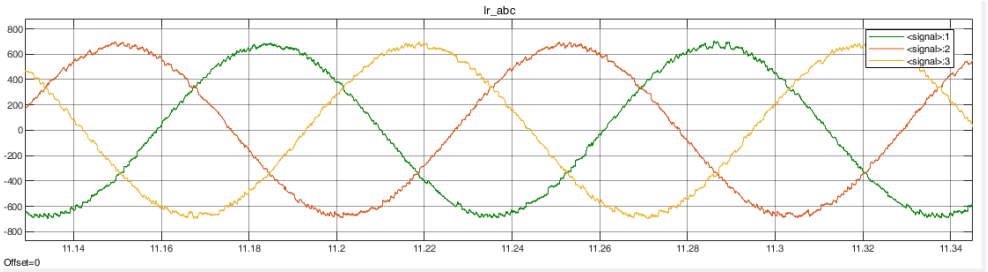

Figure 6.69: Case c3- rotor current (A)

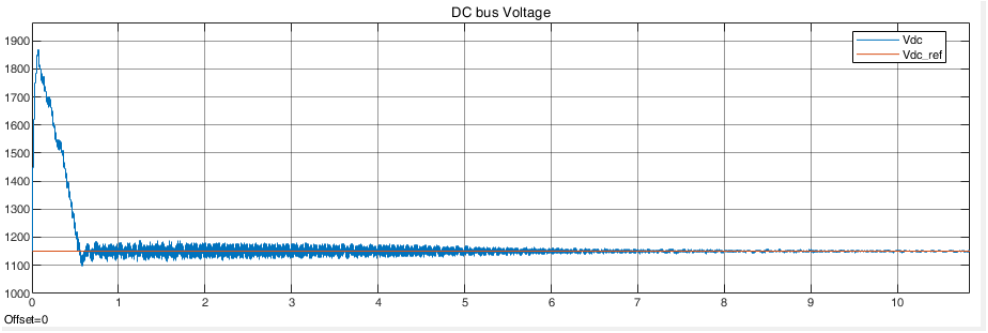

Figure 6.70: Case c3- DC link voltage (V)

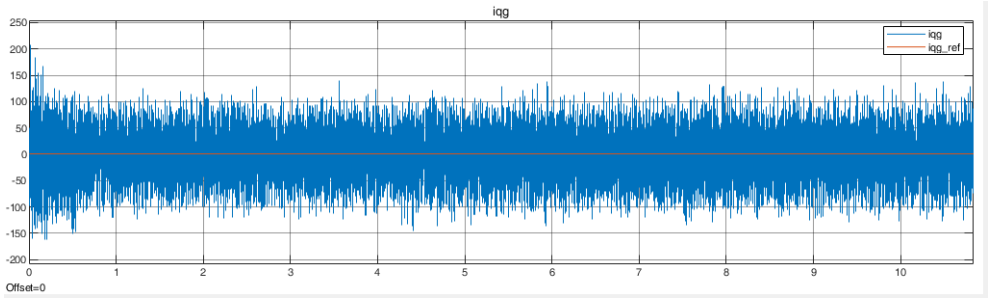

Figure 6.71: Case c3- q axis GSC current (A)

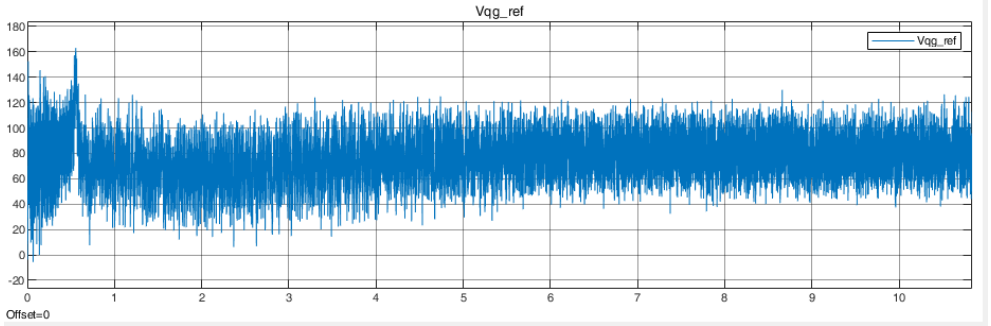

Figure 6.72: Case c3- q axis GSC voltage (V)

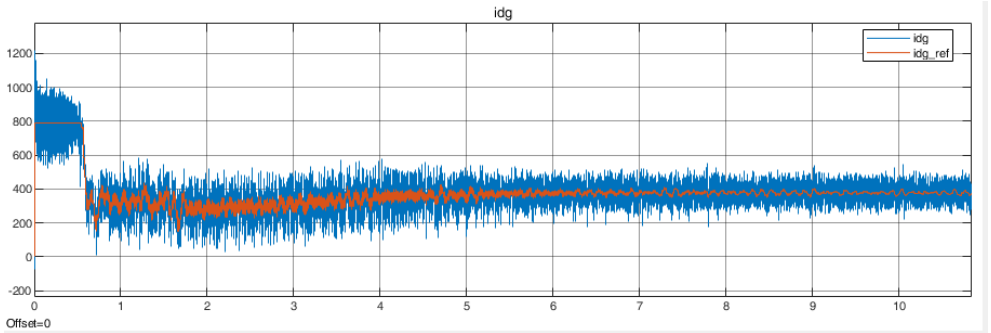

Figure 6.73: Case c3- d axis GSC current (A)

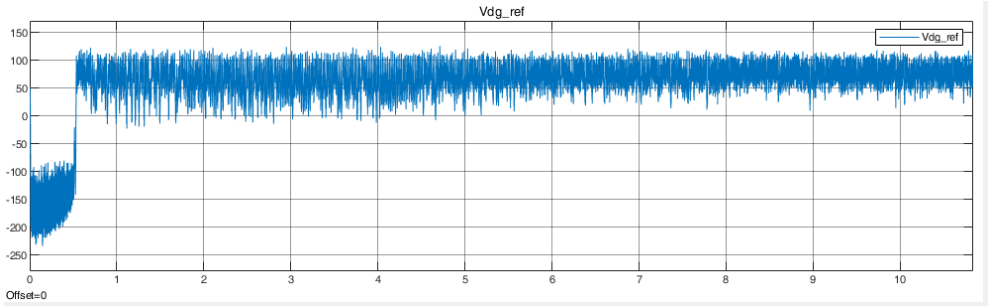

Figure 6.74: Case c3- d axis GSC voltage (V)

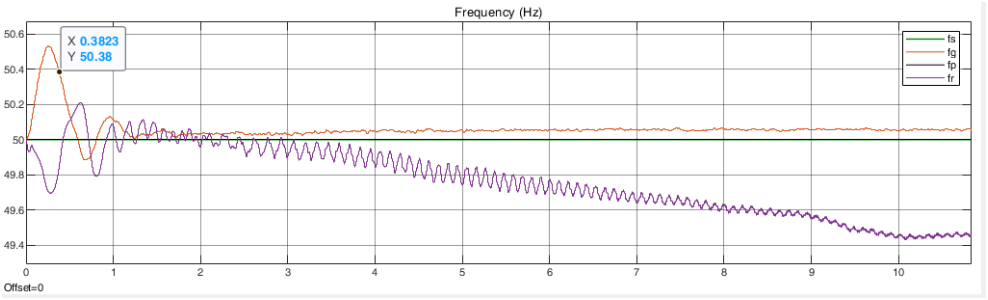

Figure 6.75: Case c3- rotor (purple), stator (red), and grid (yellow) voltage frequency

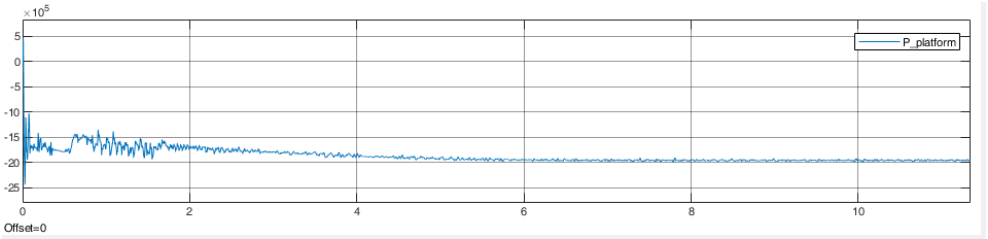

Figure 6.76: Case c3: power delivered to the load (W)

as explained before in case b2. Figures 6.63 and 6.64 illustrate the correct reference tracking of the PI controllers and in figure 6.65 and 6.66 the voltage signals for the PWM algorithm are presented. The electromagnetic torque settles quite nicely after the initial 6 seconds transients (figure 6.67). The stator and rotor current are much better than the previous cases because of less fluctuations in the currents of the PI controllers (figure 6.68 and 6.69). The GSC controller is unchanged and therefore, the results of figures 6.70 to 6.74 are quite similar to previous case (although with lower transients an a much better steady state result). Figure 6.75 shows the frequency of different voltage signals in the system. As the figure depicts, the frequency of the rotor settles after 10 seconds because the current references, the DC link voltage and rotor speed almost settle. Most importantly, figure 6.76 shows that the power measured at the PCC is settling at 2 MW, which was the aim of this whole progression so far. Case c3 is selected for further analysis and simulation of other components of the platform.

6.4 Case d: Gas turbine and wind turbine

In this scenario, first case c3 is connected to the gas turbine and loads and then the additional load of 5 kW is switched in and out at $t = 13, 14$ seconds as shown in figure 6.77. With this setup the gas turbine is initially supplying 5 kW and during the contingency has to provide 10 kW alongside the 2 MW coming from the wind turbine. Since the gas and wind turbines are the only sources of energy, having a constant output from wind turbine and not having the virtual inertia in place, the frequency drops down to 46.8 Hz. This is because all the stress is placed on the gas turbine to provide the load power.

Figure 6.78, 6.79 and 6.80 show the response of the system in this case. In figure 6.78 the yellow waveform shows the change in the active power demand of the load, the red waveform is the output power of the gas turbine and the green waveform is the output power of the ESS which is disconnected with a large impedance (it is still drawing some current, I forgot to solidly disconnect it but it does not affect the results). Note that from this scenario forward, load power is shown with a DC gain of -2MW in order to illustrate the share of gas turbine and ESS.

Figure 6.79 shows the frequency response of the system. As it can be seen, the frequency drops substantially to almost 46.8 Hz due to the added load but it will recover after the load is set back to its initial value. Figure 6.80 shows that the magnitude of the peak ac voltage at PCC remains constant and it will keep its three phase sinusoidal waveform and the current drawn from the gas turbine increases in the period of excess power. Notice the saturation of the input mechanical power of the gas turbine (due to the governor saturation) after 0.6 seconds and decrease of the gas turbine rotor speed at the same time. If this contingency were to continue more than one seconds, the speed would have reached even lower values. Similar scenario would have happened to the frequency. After the load is set back to initial value, the gas turbine speeds up again and the frequency gets back to nominal value. Next case studies the effect of adding the ESS and emulating virtual inertia.

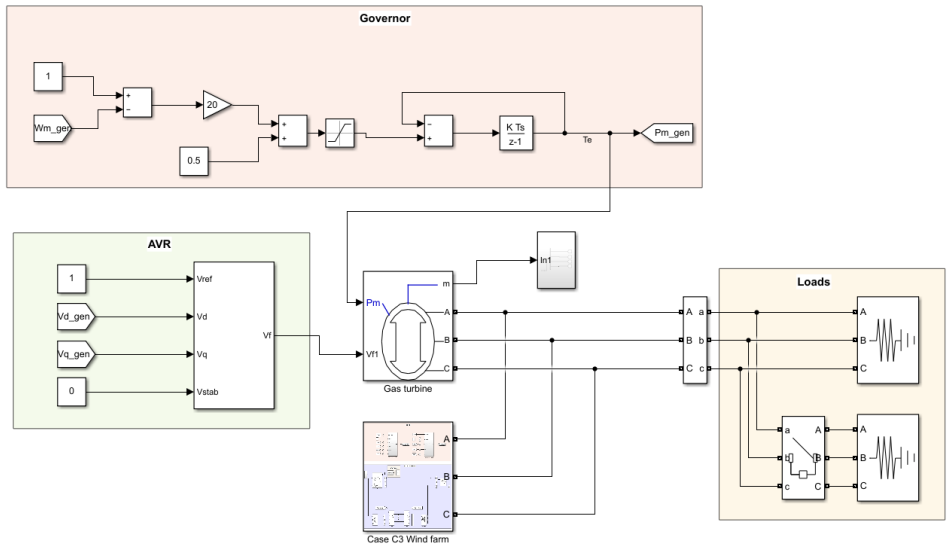

Figure 6.77: Case d simulation model

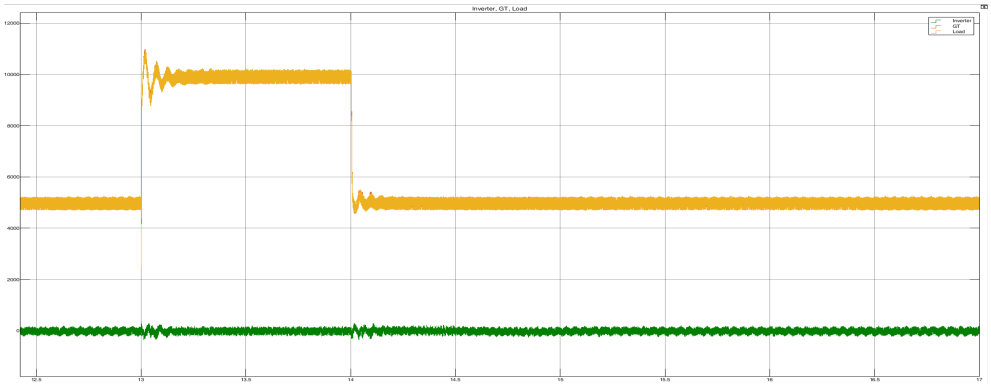

Figure 6.78: Case d- active power of load [W] (yellow), output power of the gas turbine (red) and output power of the ESS [W] (green)

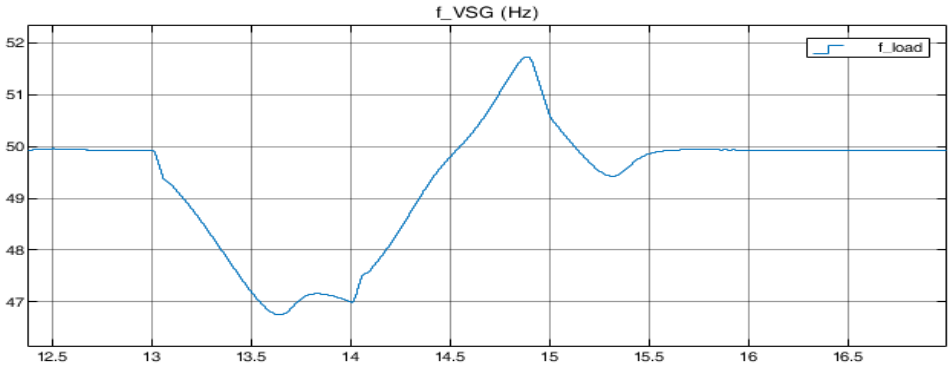

Figure 6.79: Case d- grid frequency [Hz]

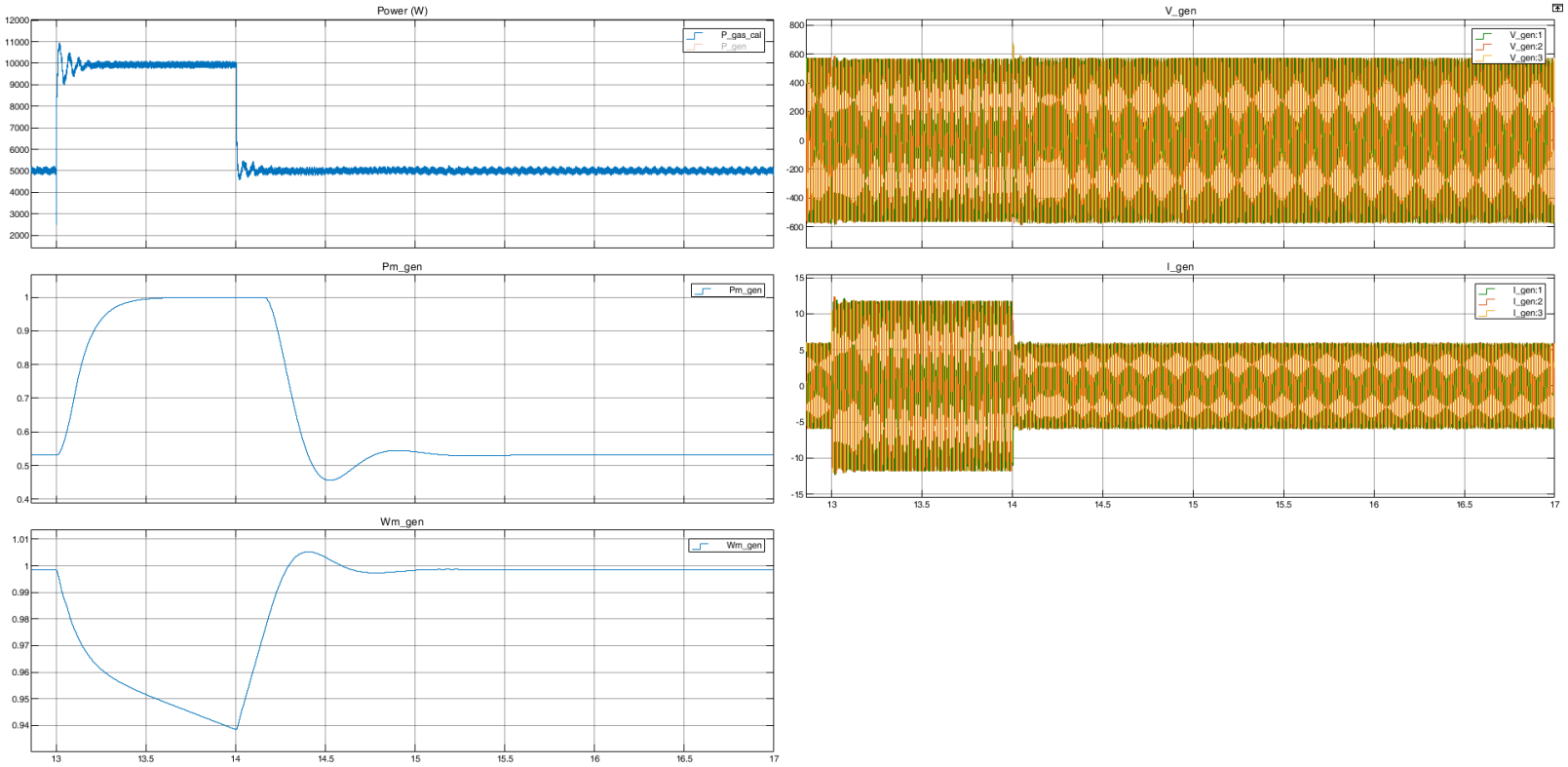

Figure 6.80: Case d- gas turbine simulation results. output power [W] (top-left), input mechanical power [pu] (mid-left), generator speed [pu] (bottom-left), three phase ac output voltage [V] (top-right), and three phase ac current output current [A] (mid-right)

6.5 Case e: Gas turbine, ESS with P controller for Virtual inertia and wind turbine

In this scenario, similar to previous scenario, the additional load of 5 kW is switched in and out at $t = 13,14$ seconds. The P controller successfully implements the inertia emulation by simulating the droop control of a governor in SG. The stress on gas turbine is reduced considerably, because the ESS starts injecting power as soon the load is switched in and frequency deviation is observed. Figure 6.82 shows that the gas turbine power jumps to 10 KW at $t = 13s$ to supply the necessary load, while the ESS slowly injects power to the grid. After about 0.5 seconds that the ESS is contributing approximately 1.8 kW, the gas turbine experience less output power then 10 kW. At $t = 14s$ that the load is set back to the initial value the ESS stops injecting power to the grid after a small transient and the gas turbine also supplies the 5 kW initial load.

Figure 6.83 shows the operation of the ESS. At $t = 13s$ when the additional load is connected, the frequency start to drop. The sensors pick up this change and feedback the frequency to the P controller. The controllers generates the reference current signal for the d axis. The current controllers are operating smoothly with very low oscillations and control the currents. According to the Park transformation, the q axis voltage is set to zero and d axis follows the RMS value of the output voltage. The q axis voltage only deviates from its zero reference value during the transients. The waveform of the current drawn from the ESS is directly linked to the power output of the ESS. The power output (shown as Po_VSG) in the figure justifies the operation of the ESS according to the goal that was defined (which is injection of additional energy to the grid to relieve the stress on gas turbine and emulate virtual inertia). The dP_in waveform shows the output signal of the P controller which divided by the d axis voltage is the current reference. The controllers can be controlled better to have less error and oscillations. The positive contribution of the ESS is directly reflected in the frequency of the grid and the frequency response of the system has been improved substantially and only drops to 48.5 Hz in its nadir point.

Figure 6.84 illustrates the response of the gas turbine to load addition while the ESS is connected. In this scenario, the mechanical input of the gas turbine was not saturated and the speed drop was significantly less (0.974 pu compared to 0.938 pu in previous case), while the magnitude of the peak ac voltage remained constant. Additionally, even if the load change would continue after $t = 14s$ the gas turbine would not loose its speed because the ESS designed is capable of injecting infinite energy and at around $t = 13.8$, the grid reached a new steady state condition. If more restrictions were added to the ESS model, the response would have been different. After $t = 14s$ the system goes back to the initial state after a small transient.

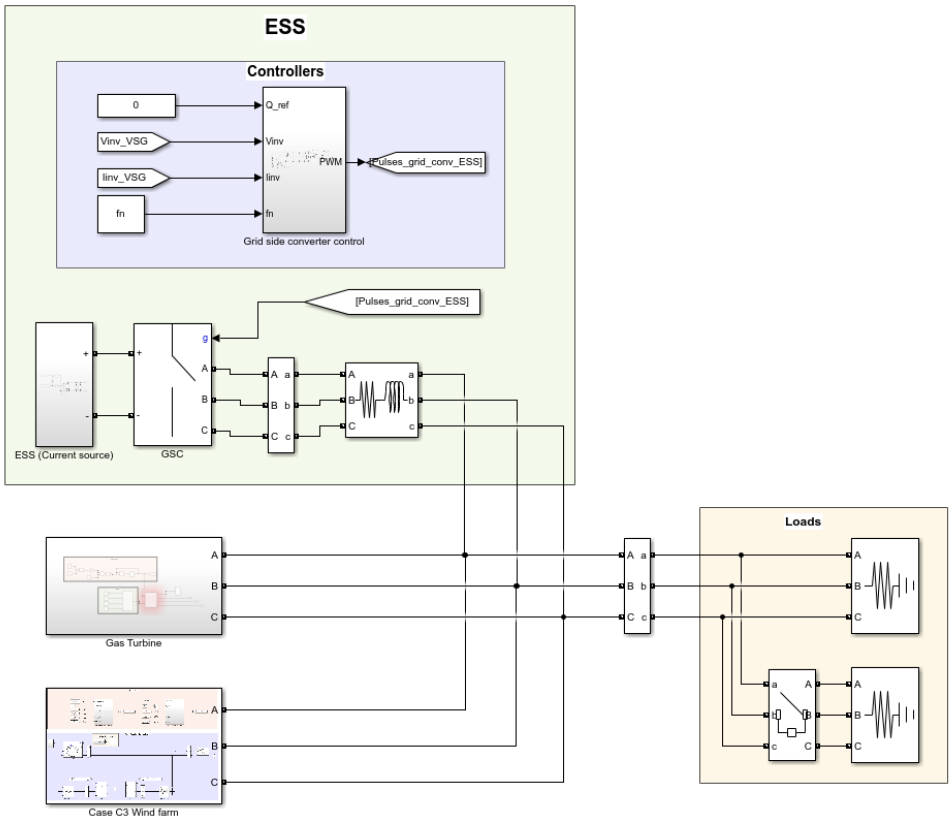

Figure 6.81: Case e simulation model

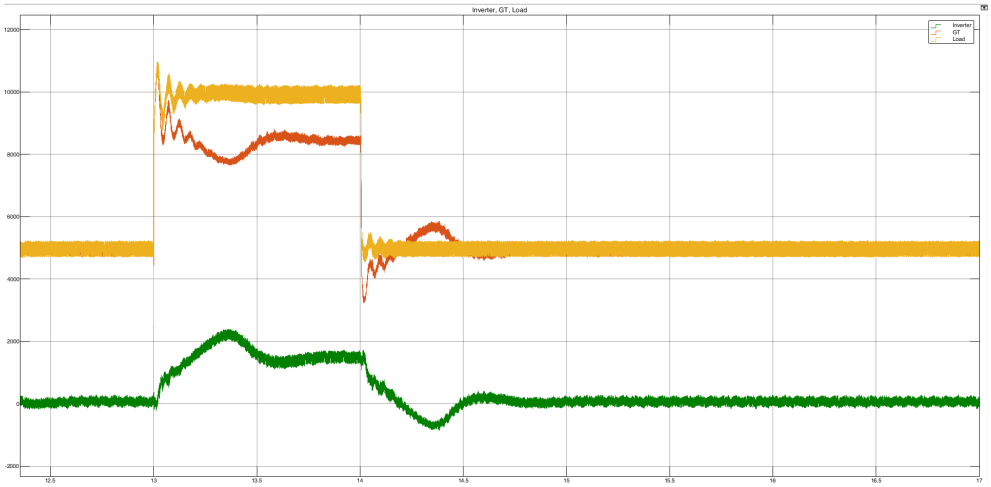

Figure 6.82: Case e- active load power [W] (yellow), gas turbine output power [W] (red), and ESS output power [W] (green)

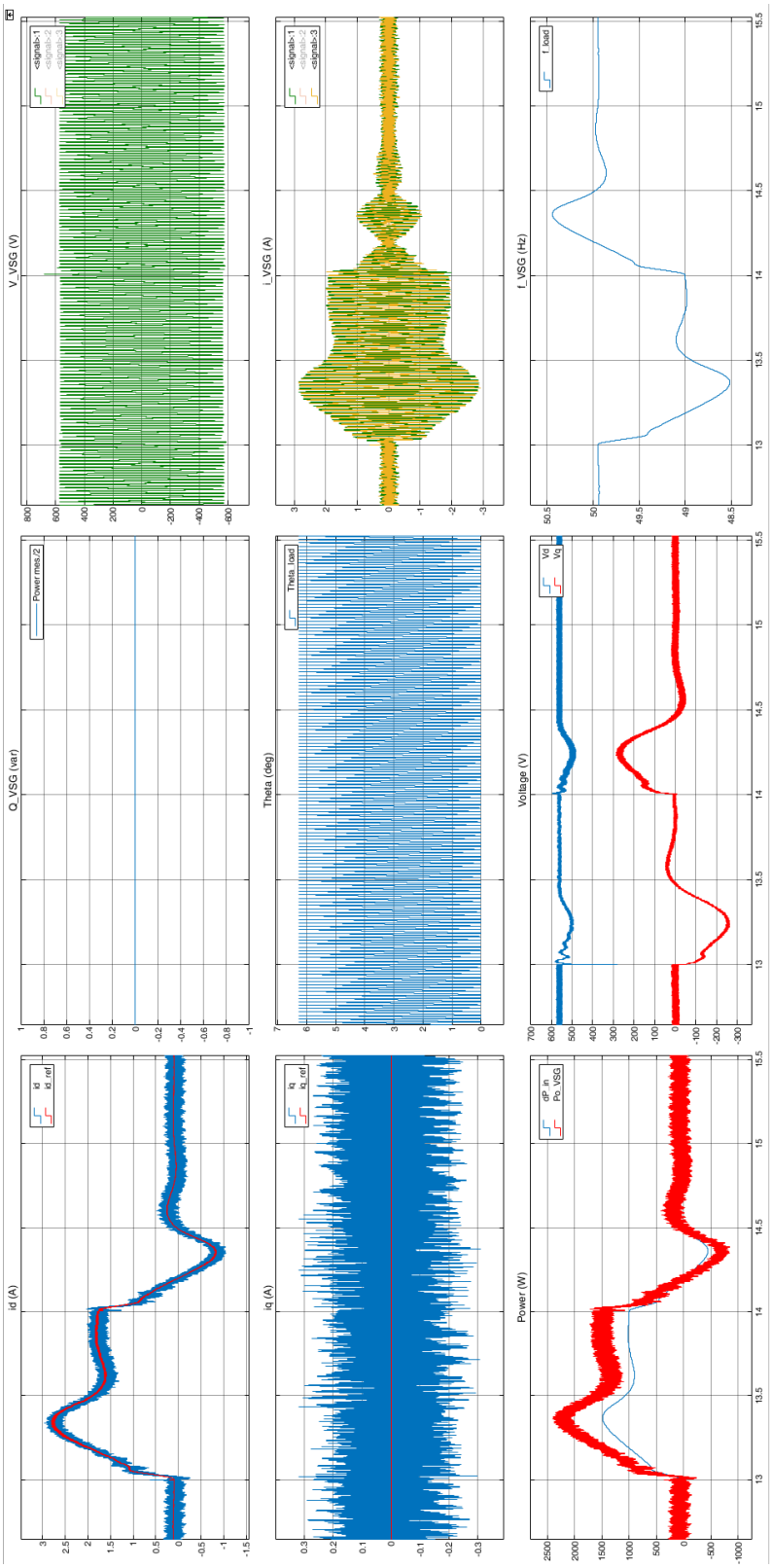

Figure 6.83: Case e- ESS converter simulation results. d axis current and its reference [A] (top-left), q axis current and its reference [A] (mid-left), Output active power and its reference [W] (bottom-left), Output reactive power [Var] (top-mid), PLL angle [deg] (mid-mid), output voltage in d and q reference [V] (bottom-mid), ac output voltage of phase a [V] (top-right), ac output current of phase a [A] (mid-right), and frequency [Hz] (bottom-right)

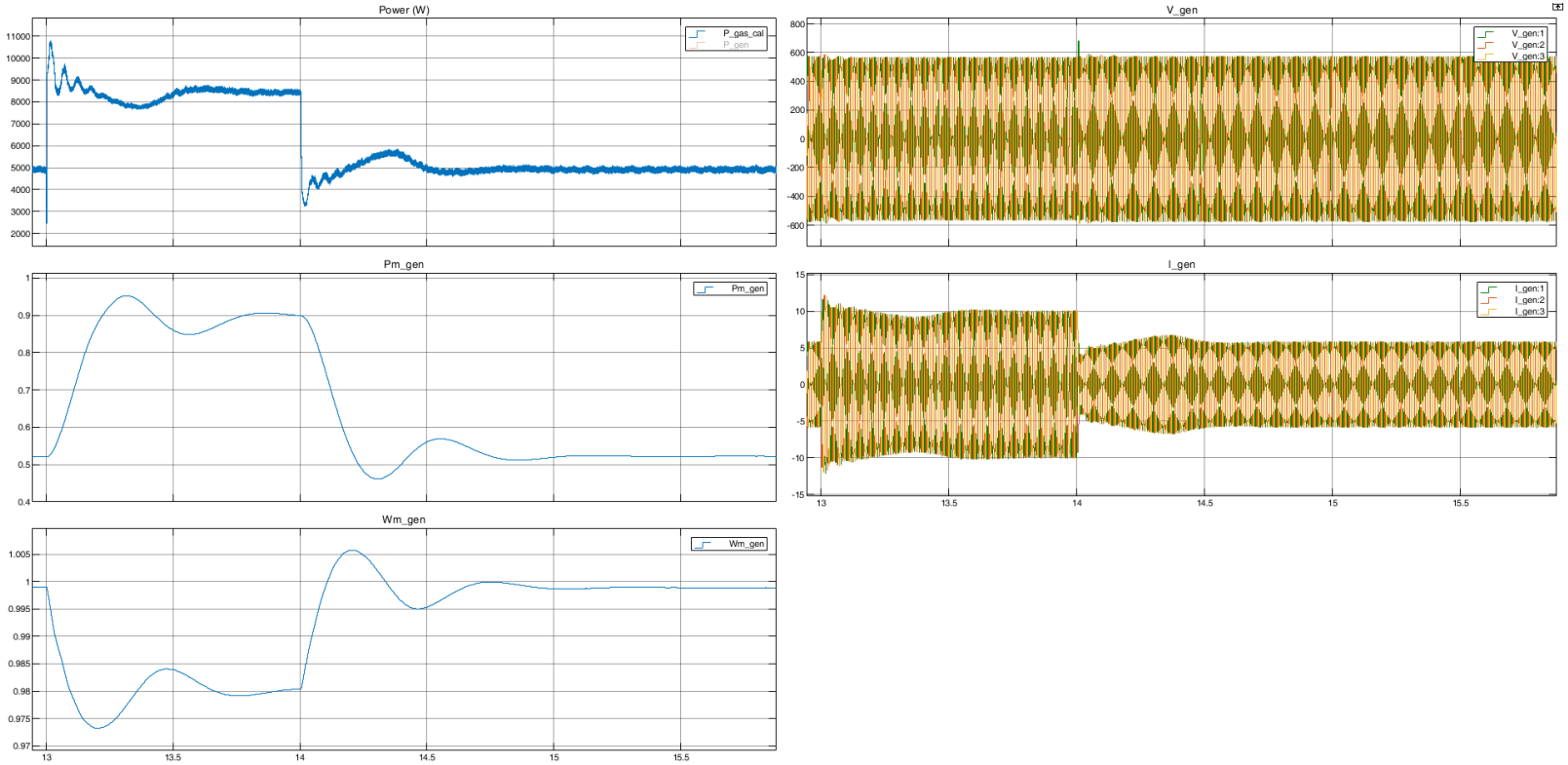

Figure 6.84: Case e- gas turbine simulation results. output power [W] (top-left), input mechanical power [pu] (mid-left), generator speed [pu] (bottom-left), three phase ac output voltage [V] (top-right), and three phase ac current output current [A] (mid-right)

6.6 Case f: Gas turbine, ESS with PI controller for virtual inertia and wind turbine

In this scenario, the load changes similar to previous case. All the explanations of the previous case also applies to this one. The PI controller successfully implements the inertia emulation. The frequency response of the system has been improved substantially and even better than the previous case (frequency nadir is 48.7 Hz instead of 48.5 Hz), although after disconnecting the additional load, the steady state result is achieved later than the previous case. A derivative term could also be added to the controller, but it was avoided in this method due to possible stability issues. Figure 6.85, 6.86 and 6.87 show the response of the system in this case. The system will reach steady state eventually at the initial conditions but due to computational limits the system was only simulated until $t = 17s$.

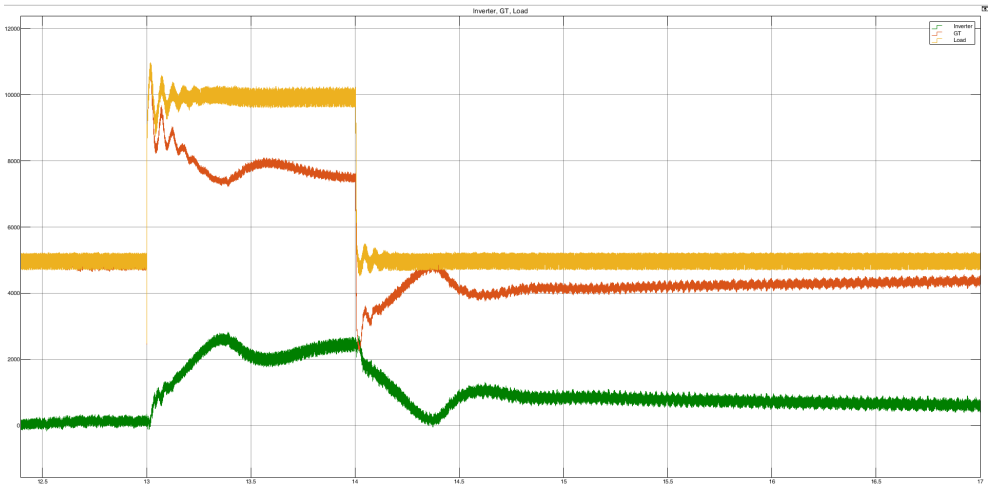

Figure 6.85: Case f- active load power [W] (yellow), gas turbine output power [W] (red), and ESS output power [W] (green)

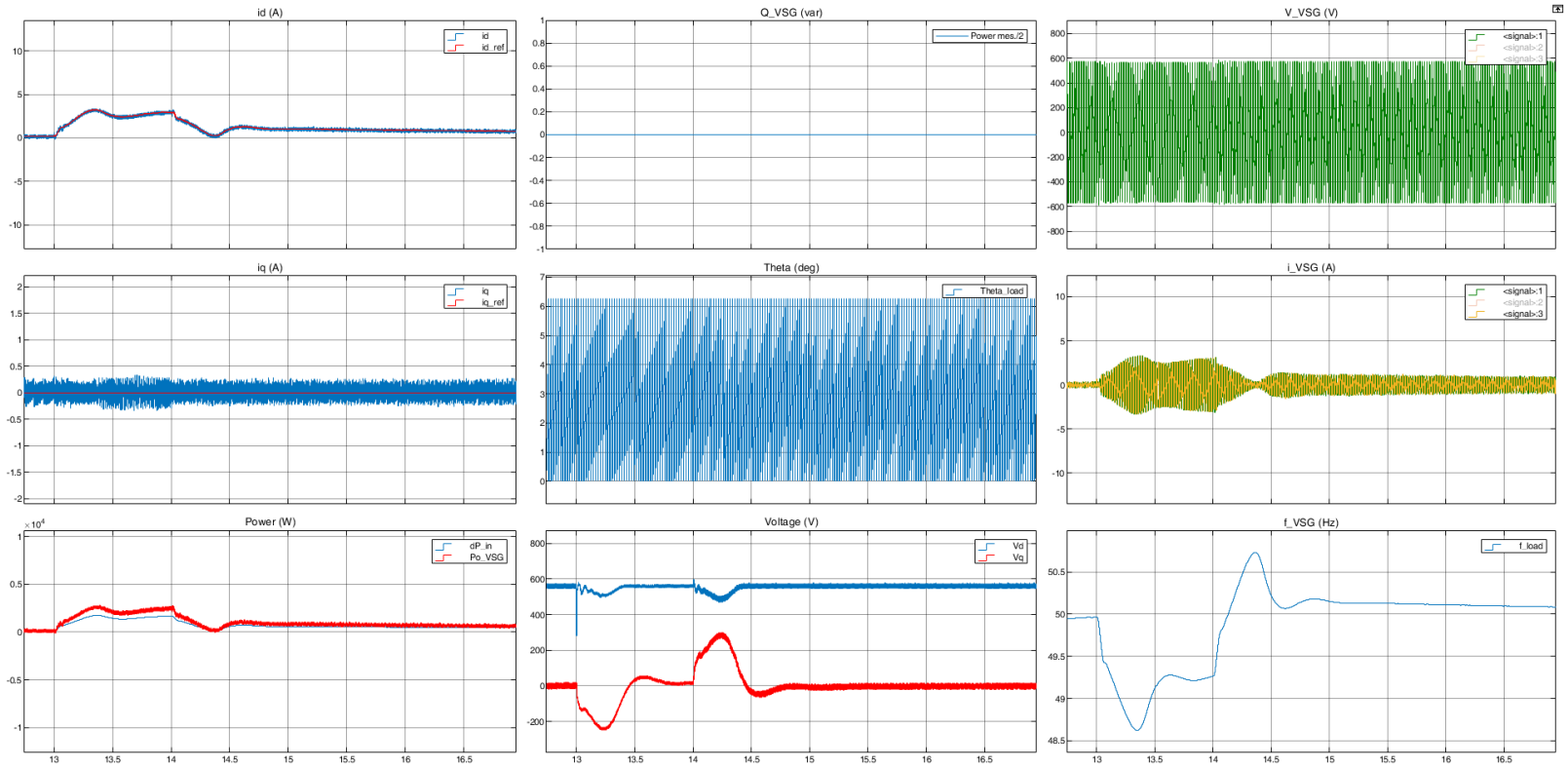

Figure 6.86: Case f- ESS converter simulation results. d axis current and its reference [A] (top-left), q axis current and its reference [A] (mid-left), Output active power and its reference [W] (bottom-left), Output reactive power [Var] (top-mid), PLL angle [deg] (mid-mid), output voltage in d and q reference [V] (bottom-mid), ac output voltage of phase a [V] (top-right), ac output current of phase a [A] (mid-right), and frequency [Hz] (bottom-right)

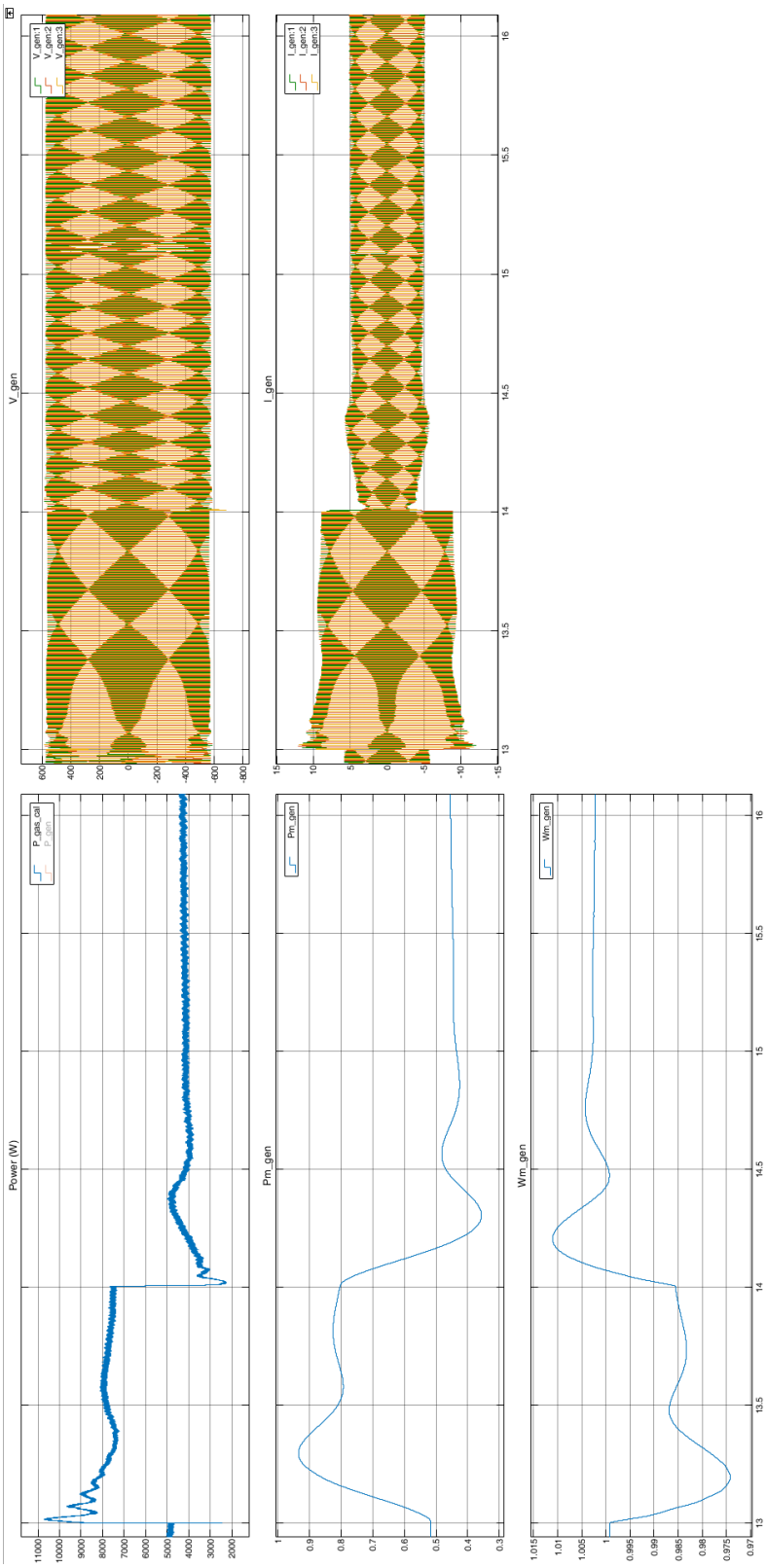

Figure 6.87: Case f- gas turbine simulation results. output power [W] (top-left), input mechanical power [pu] (mid-left), generator speed [pu] (bottom-left), three phase ac output voltage [V] (top-right), and three phase ac current output current [A] (mid-right)

6.7 Case g: Gas turbine, ESS with PI controller and dead zone for virtual inertia and wind turbine

In this scenario, the load changes are identical to last case. The deadzone limits the input of the PI controller and as a result the frequency drops more than in case f (drops to 48.45 Hz). The idea behind adding the deadzone was to reduce the sensitivity of the ESS to the frequency changes in the system, so that the ESS only would be activated if the frequency deviations violates a certain range. A disadvantage of this method is the slower steady state result which is not desirable. Therefore, the addition of the dead zone appears to be unnecessary when the PI controller is implemented. The same explanations of the two previous cases are also valid for this scenario. Figure 6.89, 6.90, and 6.88 show the response of the system in this case.

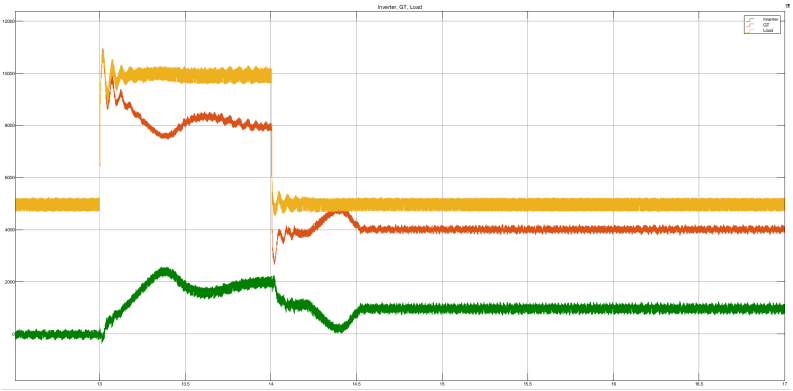

Figure 6.88: Case g- active load power [W] (yellow), gas turbine output power [W] (red), and ESS output power [W] (green)

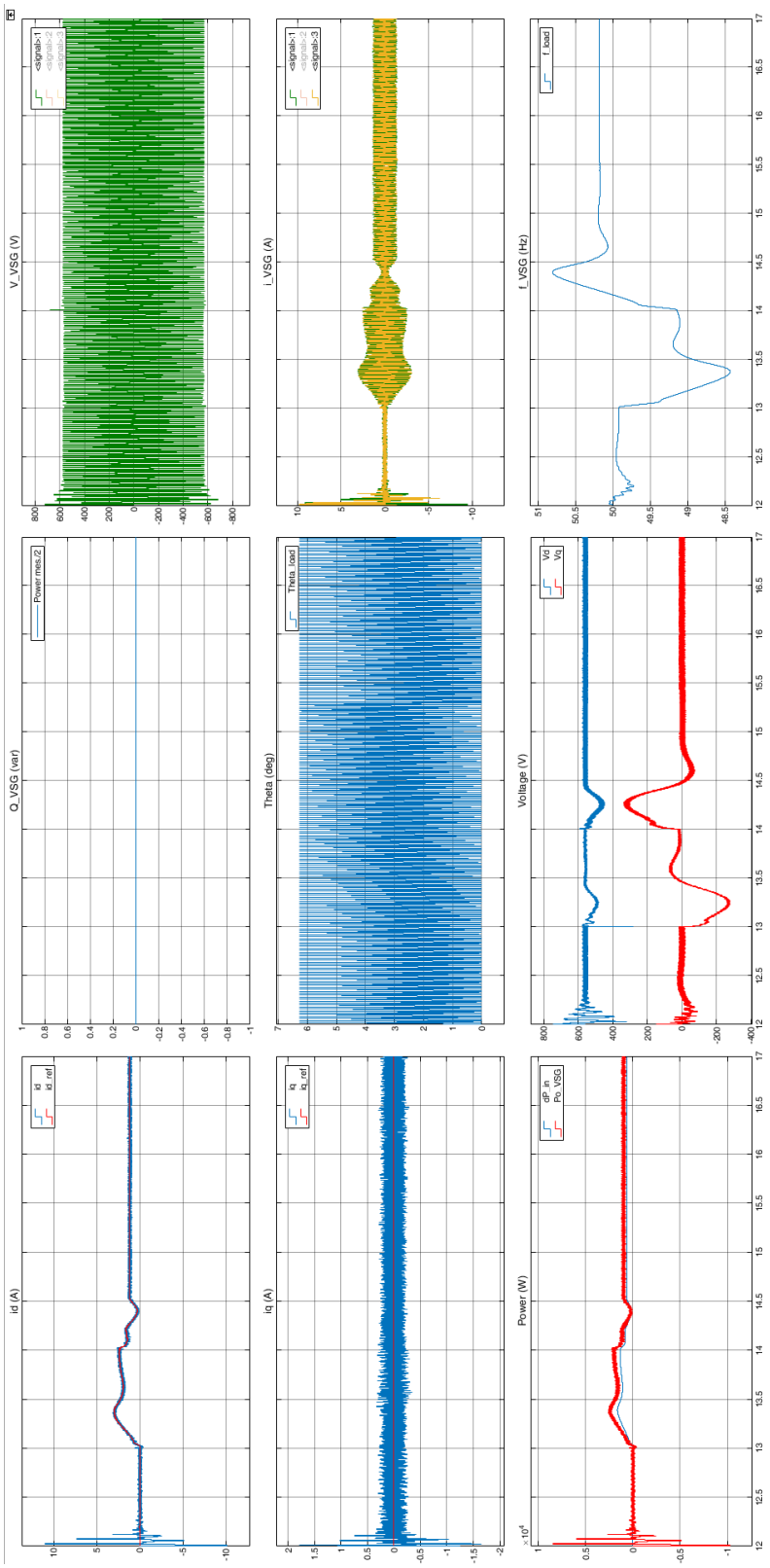

Figure 6.89: Case g- ESS converter simulation results. d axis current and its reference [A] (top-left), q axis current and its reference [A] (mid-left), Output active power and its reference [W] (bottom-left), Output reactive power [Var] (top-mid), PLL angle [deg] (mid-mid), output voltage in d and q reference [V] (bottom-mid), ac output voltage of phase a [V] (top-right), ac output current of phase a [A] (mid-right), and frequency [Hz] (bottom-right)

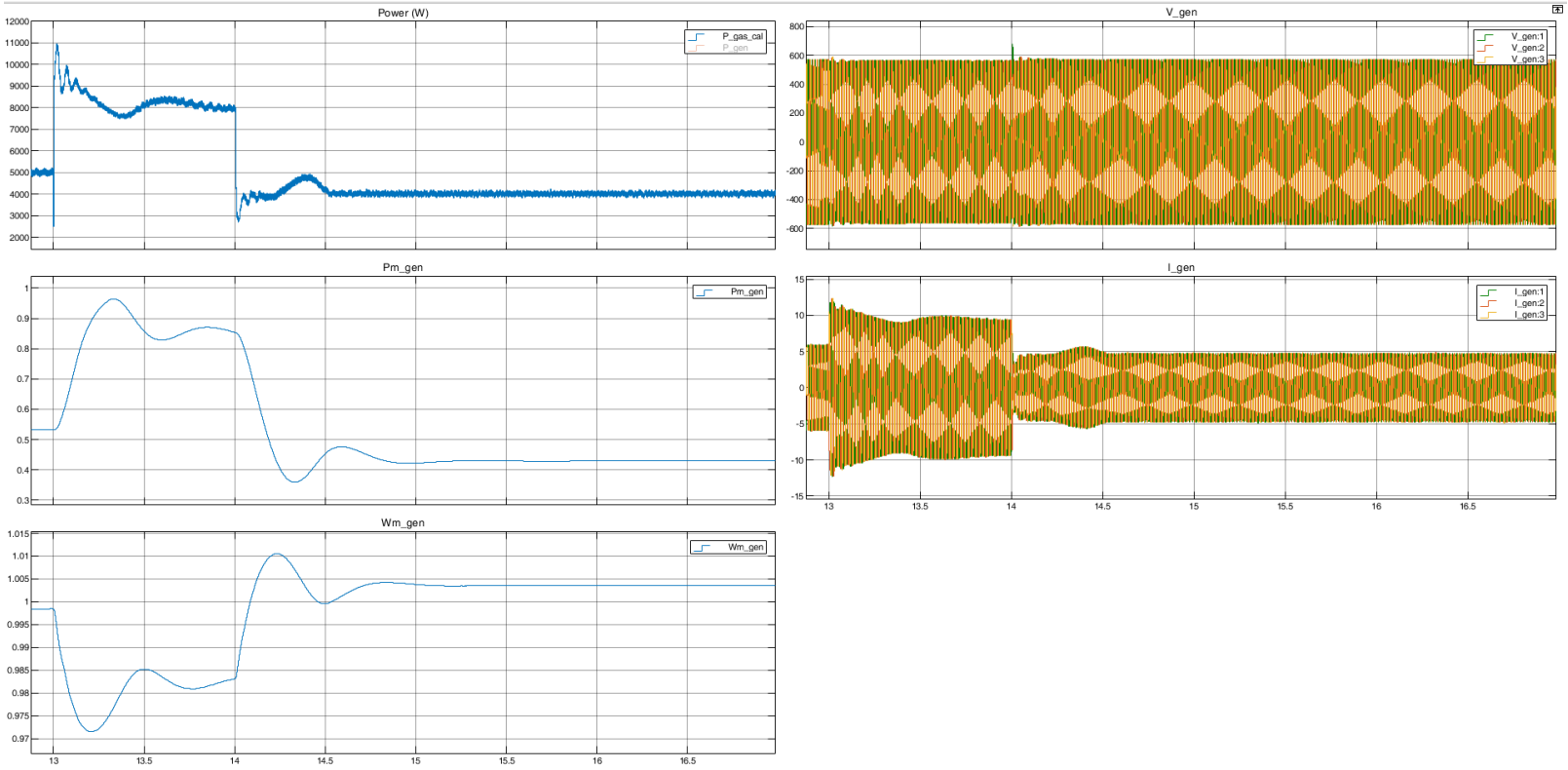

Figure 6.90: Case g- gas turbine simulation results. output power [W] (top-left), input mechanical power [pu] (mid-left), generator speed [pu] (bottom-left), three phase ac output voltage [V] (top-right), and three phase ac current output current [A] (mid-right)

6.8 Comparison between cases with virtual inertia emulation

The results of the previous cases (d to g) are compared in this section.

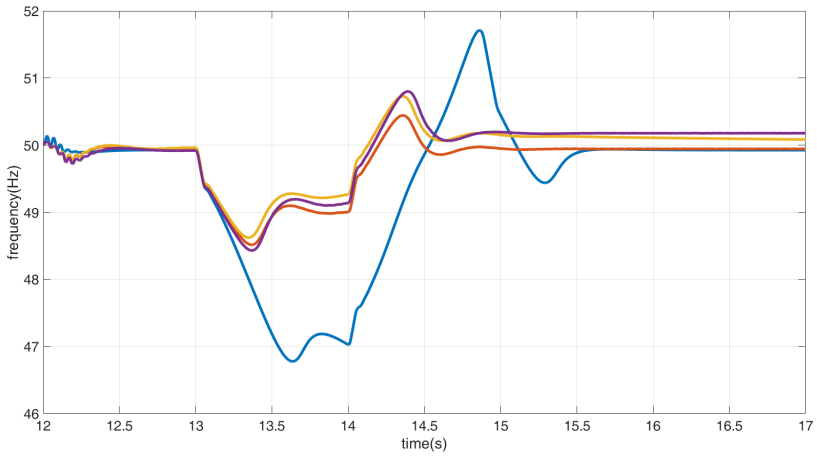

Figure 6.91: Frequency response of the platform grid in case d (blue), e (red), f (yellow), and g (purple) to the load change

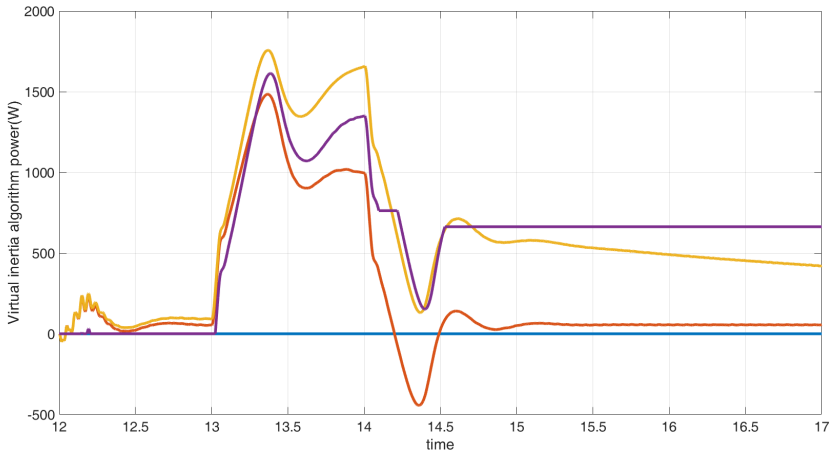

Figure 6.92: Virtual inertia block response in case d (blue), e (red), f (yellow), and g (purple) to the load change

As figure 6.91 illustrates, case f offers the highest inertial support, while case d offers the lowest. In case f, the frequency nadir is 48.7 Hz, while in case d the frequency drops to 46.8 Hz. Also the ROCOF is considerably lower in cases e,f and

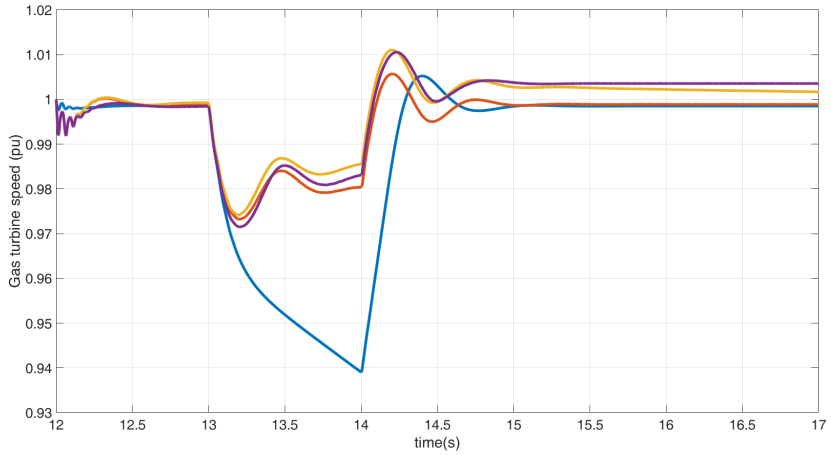

Figure 6.93: Gas turbine speed response in case d (blue), e (red), f (yellow), and g (purple) to the load change

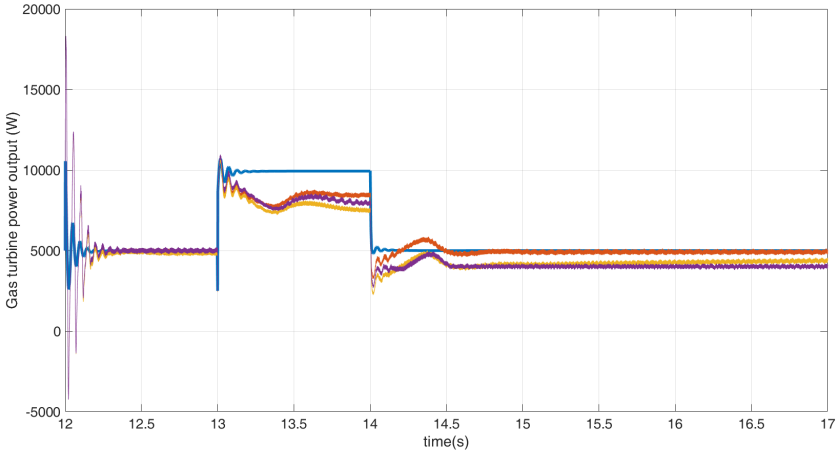

Figure 6.94: Gas turbine output power in case d (blue), e (red), f (yellow), and g (purple) to the load change

g where the ESS contributes to the energy balance of the system and the system restores faster. The contribution of the ESS is shown by the output power of the virtual inertia block, which will be the reference power signal of the ESS converter. As figure 6.92 illustrates, case f draws the highest power form the ESS as expected. Figure 6.94 shows the stress on the gas turbine for the defined scenarios, where case d has the highest impact on the gas turbine, as ESS is not injecting any power to assist the gas turbine. The higher power extraction from ESS in case f is also reflected in gas turbine power output, as in this case the lowest amount of power is extracted from the gas turbine, meaning less stress during the contingency event. As gas turbine speed and output power are linked, similar scenario happens for gas turbine speed as depicted in figure 6.93.

Chapter 7

Conclusions and Future Work

7.1 Conclusions

This thesis provided a literature review on methods to provide virtual inertia for systems with high integration of RES by a thorough presentation on the background involved. Multiple methods were discussed and objectively all the methods strive to provide a dynamic frequency response via the converters. The methodology can be selected based on system characteristics, limitations, level of complexity and other goals. Some of the methods provide more detailed frequency response to the converter (much similar to SG) while others can be as simple as a delay.

The complications of the project involved the operation of the grid as a whole, while considering the interaction of the grid components, tuning of the controllers and priorities for control. Gathering data from the LEOGE platform, it was noted that several loads are dependant on the presence of the gas turbine and therefore, the gas turbine was essential while it had other responsibilities in the grid such as fixing the voltage of the PCC. It was concluded that the loads of the platform can be modeled as a whole without affecting the operation of the system, the inertia emulation algorithm or the interactions with the wind farm.

The wind turbines were scaled down same as loads of the platform for reducing the computation load on the PC used for simulation, without affecting the approach, methodology and the results of the project. The type three connection was used for wind turbines with DFIG. The switching converters were controlled by SVPWM method with signals generated form PI controllers. An MPPT algorithm was shown to be the most suitable option for controlling the RSC. The main goal for the controllers of the DFIG converters were to be able to control the DFIG so that it delivers almost constant power to the grid of the platform and supply the base loads, while eliminating the need for larger gas turbines or diesel generators.

An ESS was proved to be the best option for proving the energy support and

emulating virtual inertia during a contingency event. The model consists of a hypothetically infinite ESS with a switching converter, that is controlled according to the changes in the grid frequency. The developed virtual inertia algorithm for the system was selected such that, the complexity of the project and interactions of the grid components would be straightforward. Each component was validated separately to better analyse its dynamics and effects on the system as a whole. Then the components were assembled together and the final simulations considered the interaction of all the grid elements.

The developed model successfully emulates virtual inertia in the concept model of the oil and gas platform by extracting the necessary energy from the ESS to slow down the ROCOF, while the wind turbine supplies the base loads of the platform. Between the proposed methods for emulating inertia, the PI controlled appeared to provide the best frequency response compared to cases with PI with dead-band, and P controller. A derivative controller was not used to prevent the possible stability issues. For the PI controller to provide a better inertial response, more energy was extracted from the ESS. On the other hand, the gas turbine experienced less stress and was able to maintain its rotor speed at a higher value while the input mechanical power of the generator was also not saturated. Preventing the saturation of the gas turbine input translates to less consumption of fuel for the generator which is aligned with the goal of reducing the carbon emission of the oil and gas platform (Although most of the contribution is because of introducing the offshore wind turbines).

7.2 Future Work

Other than the methods explained in chapter 3, newer methods to provide virtual inertia are being developed. A considerable number of these methods rely on artificial intelligence and optimization algorithms. Some of which, aim to minimize the frequency nadirs while injecting more energy to the grid. Some other strive for reducing the stress on the ESS, maximising its lifetime or optimise the sizing of the ESS.

The other methods to provide virtual inertia can be implemented on this model and compared with the results of this thesis to evaluate the advantages and disadvantages of each one in this case. The addition of neural network based algorithms, which are widely used in the literature, can outperform the conventional PI controllers in speed and accuracy for controlling different parameters of the system. Furthermore, the modeling of the platform itself, can be more detailed and specific limitations and conditions applied due to the nature of different loads on the structure (for example considering unbalanced load and its dynamics). The variable wind speed can be easily incorporated to the final model. Although the power output of the wind farm will be fluctuated around the nominal output, the

imbalance can be compensated with an external energy source. Therefore, with modification of the control model for the ESS, this goal can be achieved. Also, the scenarios can be defined more elaborately and discuss different contingency events for the offshore platform and the virtual inertia strategy can then be analysed more scrutinisingly. Additional ancillary services are defined in grid codes and they can be implemented in the modeling of the system, making the study even more generalised. The study can be expanded to the type of ESS technology used and additional goals for the ESS such as lifetime, sizing and so on can be part of the study.

Bibliography

[1] Y. Zheng, *Virtual inertia emulation in islanded microgrids with energy storage system, master of science thesis, delft university*, 2016. [Online]. Available: http://resolver.tudelft.nl/uuid:51849a15-2f89-447b-8661-ac5d12b44edb.

[2] F. Blaabjerg, R. Teodorescu, M. Liserre and A. Timbus, 'Overview of control and grid synchronization for distributed power generation systems,' *Industrial Electronics, IEEE Transactions on*, vol. 53, pp. 1398–1409, Nov. 2006. DOI: 10.1109/TIE.2006.881997.

[3] P. Denholm, T. Mai, R. W. Kenyon, M. O'Malley and B. Kroposki. (2020). 'Inertia and the power grid: A guide without the spin, nrel,' [Online]. Available: https://www.nrel.gov/docs/fy20osti/73856.pdf..

[4] U. Tamrakar, D. Shrestha, M. Maharjan, B. P. Bhattarai, T. M. Hansen and R. Tonkoski, 'Virtual inertia: Current trends and future directions,' *Applied Sciences*, vol. 7, no. 7, 2017, ISSN: 2076-3417. DOI: 10.3390/app7070654. [Online]. Available: https://www.mdpi.com/2076-3417/7/7/654.

[5] R. Eriksson, N. Modig and K. Elkington, 'Synthetic inertia versus fast frequency response: A definition,' *IET Renewable Power Generation*, vol. 12, Sep. 2017. DOI: 10.1049/iet-rpg.2017.0370.

[6] A. Fernández-Guillamón, E. Gómez-Lázaro, E. Muljadi and Á. Molina-García, 'Power systems with high renewable energy sources: A review of inertia and frequency control strategies over time,' *Renewable and Sustainable Energy Reviews*, vol. 115, p. 109 369, 2019. DOI: 10.1016/j.rser.2019.109369.

[7] W. He, K. Uhlen, M. Hadiya, Z. Chen, G. Shi and E. del Rio, 'Case study of integrating an offshore wind farm with offshore oil and gas platforms and with an onshore electrical grid,' *Journal of Renewable Energy*, vol. 2013, pp. 1–10, 2013. DOI: 10.1155/2013/607165.

[8] H. G. Svendsen, A. Holdyk, I. R. Mosgren and J. Wiik, *Deliverable report: Dsp5_2020_05, test platform specification, modelling and operational optimization results*, 2020.

[9] A. E. Tutorials, *Synchronous generator as a wind power generator*, Dec. 2021. [Online]. Available: https://www.alternative-energy-tutorials.com/wind-energy/synchronous-generator.html.

[10] P. Kundur, *Power system stability and control*. McGraw-Hill.

[11] M. Khatibi, F. Rahmani and T. Agarwal, 'Comparative Analysis of Power System Model Reduction,' *arXiv e-prints*, arXiv:2004.04112, arXiv:2004.04112, Apr. 2020. arXiv: 2004.04112 [eess.SY].

[12] *Frequency control in a power system - technical articles*. [Online]. Available: https://eepower.com/technical-articles/frequency-control-in-a-power-system/#.

[13] P. Tavner, *What are the disadvantages of a pmsg compared to a dfig?* Feb. 2019. [Online]. Available: https://www.researchgate.net/post/What-are-the-disadvantages-of-a-PMSG-compared-to-a-DFIG.

[14] G. Abad, *Doubly fed induction machine: modeling and control for wind energy generation applications*. IEEE Press, 2011.

[15] H. Abu-Rub, M. Malinowski and K. Al-Haddad, *Power electronics for renewable energy systems, transportation, and industrial applications*. Wiley/IEEE, 2014.

[16] B. Kroposki, B. Johnson, Y. Zhang, V. Gevorgian, P. Denholm, B.-M. Hodge and B. Hannegan, 'Achieving a 100% renewable grid: Operating electric power systems with extremely high levels of variable renewable energy,' *IEEE Power and Energy Magazine*, vol. 15, no. 2, pp. 61–73, 2017. DOI: 10.1109/mpe.2016.2637122.

[17] A. Fernández-Guillamón, E. Gómez-Lázaro, E. Muljadi and Á. Molina-García, 'Power systems with high renewable energy sources: A review of inertia and frequency control strategies over time,' *Renewable and Sustainable Energy Reviews*, vol. 115, p. 109 369, 2019. DOI: 10.1016/j.rser.2019.109369.

[18] H. Bevrani, T. Ise and Y. Miura, 'Virtual synchronous generators: A survey and new perspectives,' *International Journal of Electrical Power Energy Systems*, vol. 54, pp. 244–254, 2014. DOI: 10.1016/j.ijepes.2013.07.009.

[19] N. B. Negra, J. Todorovic and T. Ackermann, 'Loss evaluation of hvac and hvdc transmission solutions for large offshore wind farms,' *Electric Power Systems Research*, vol. 76, no. 11, pp. 916–927, 2006, ISSN: 0378-7796. DOI: https://doi.org/10.1016/j.epsr.2005.11.004. [Online]. Available: https://www.sciencedirect.com/science/article/pii/S0378779605002609.

[20] *Wind turbine generator model validation (wtgmv)*. [Online]. Available: https://www.esig.energy/wiki-main-page/wind-turbine-generator-model-validation-wtgmv/.

[21] S. Azmi, K. Ahmed, S. Finney and B. Williams, 'Comparative analysis between voltage and current source inverters in grid-connected application,' *IET Conference on Renewable Power Generation (RPG 2011)*, 2011. DOI: 10.1049/cp.2011.0138.

[22] D. Pattabiraman, R. H. Lasseter. and T. M. Jahns, 'Comparison of grid following and grid forming control for a high inverter penetration power system,' in *2018 IEEE Power Energy Society General Meeting (PESGM)*, 2018, pp. 1–5. DOI: 10.1109/PESGM.2018.8586162.

[23] D. Pattabiraman, R. H. Lasseter. and T. M. Jahns, 'Comparison of grid following and grid forming control for a high inverter penetration power system,' *2018 IEEE Power Energy Society General Meeting (PESGM)*, 2018. DOI: 10.1109/pesgm.2018.8586162.

[24] Q. Zhong, 'Virtual synchronous machines: A unified interface for grid integration,' *IEEE Power Electronics Magazine*, vol. 3, pp. 18–27, 2016.

[25] L. wang Shang, J. Hu, X. YUAN and Y. HUANG, 'Improved virtual synchronous control for grid-connected vscs under grid voltage unbalanced conditions,' *Journal of Modern Power Systems and Clean Energy*, vol. 7, pp. 1–12, Apr. 2018. DOI: 10.1007/s40565-018-0388-2.

[26] W. Kenyon, A. Hoke, J. Tan, B. Kroposki and B.-M. Hodge, 'Grid-following inverters and synchronous condensers: A grid- forming pair?,' Mar. 2020. DOI: 10.1109/PSC50246.2020.9131310.

[27] G. Delille, B. Francois and G. Malarange, 'Dynamic frequency control support by energy storage to reduce the impact of wind and solar generation on isolated power system's inertia,' *Sustainable Energy, IEEE Transactions on*, vol. 3, pp. 931–939, Oct. 2012. DOI: 10.1109/TSTE.2012.2205025.

[28] M. F. M. Arani and E. F. El-Saadany, 'Implementing virtual inertia in dfig-based wind power generation,' *IEEE Transactions on Power Systems*, vol. 28, no. 2, pp. 1373–1384, 2013. DOI: 10.1109/TPWRS.2012.2207972.

[29] N. Kakimoto, S. Takayama, H. Satoh and K. Nakamura, 'Power modulation of photovoltaic generator for frequency control of power system,' *IEEE Transactions on Energy Conversion*, vol. 24, no. 4, pp. 943–949, 2009. DOI: 10.1109/TEC.2009.2026616.

[30] K. M. Cheema, 'A comprehensive review of virtual synchronous generator,' *International Journal of Electrical Power Energy Systems*, vol. 120, p. 106 006, 2020. DOI: 10.1016/j.ijepes.2020.106006.

[31] Q. Zhong, P.-L. Nguyen, Z. Ma and W. Sheng, 'Self-synchronized synchronverters: Inverters without a dedicated synchronization unit,' *IEEE Transactions on Power Electronics*, vol. 29, pp. 617–630, 2014.

[32] R. Hesse, D. Turschner and H. Beck, 'Micro grid stabilization using the virtual synchronous machine (visma),' *Renewable energy power quality journal*, vol. 1, pp. 676–681, 2009.

[33] Y. Chen, R. Hesse, D. Turschner and H. Beck, 'Improving the grid power quality using virtual synchronous machines,' in *2011 International Conference on Power Engineering, Energy and Electrical Drives*, 2011, pp. 1–6. DOI: 10.1109/PowerEng.2011.6036498.

[34] Y. Hirase, K. Abe, K. Sugimoto and Y. Shindo, 'A grid connected inverter with virtual synchronous generator model of algebraic type,' *IEEJ Transactions on Power and Energy*, vol. 132, pp. 371–380, Jan. 2012. DOI: 10.1541/ieejpes.132.371.

[35] D. Singh and K. Seethalekshmi, 'A review on various virtual inertia techniques for distributed generation,' in *2020 International Conference on Electrical and Electronics Engineering (ICE3)*, 2020, pp. 631–638. DOI: 10.1109/ICE348803.2020.9122959.

[36] K. Sakimoto, Y. Miura and T. Ise, 'Stabilization of a power system with a distributed generator by a virtual synchronous generator function,' in *8th International Conference on Power Electronics - ECCE Asia*, 2011, pp. 1498–1505. DOI: 10.1109/ICPE.2011.5944492.

[37] P. Rodriguez, I. Candela and A. Luna, 'Control of pv generation systems using the synchronous power controller,' *2013 IEEE Energy Conversion Congress and Exposition*, 2013. DOI: 10.1109/ecce.2013.6646811.

[38] M. van Wesenbeeck, S. de Haan, P. Varela and K. Visscher, 'Grid tied converter with virtual kinetic storage,' Undefined/Unknown, in *Proceedings 2009 IEEE Bucharest Power Tech Conference*, s.n., Ed., null ; Conference date: 28-06-2009 Through 02-07-2009, IEEE Society, 2009, pp. 1–7, ISBN: 978-1-4244-2235-7. DOI: doi:10.1109/PTC.2009.5282048.

[39] D. Shrestha, U. Tamrakar, Z. Ni and R. Tonkoski, 'Experimental verification of virtual inertia in diesel generator based microgrids,' in *2017 IEEE International Conference on Industrial Technology (ICIT)*, 2017, pp. 95–100. DOI: 10.1109/ICIT.2017.7913065.

[40] F. Katiraei and M. Iravani, 'Power management strategies for a microgrid with multiple distributed generation units,' *IEEE Transactions on Power Systems*, vol. 21, pp. 1821–1831, 2006.

[41] N. Pogaku, M. Prodanovic and T. C. Green, 'Modeling, analysis and testing of autonomous operation of an inverter-based microgrid,' *IEEE Transactions on Power Electronics*, vol. 22, no. 2, pp. 613–625, 2007. DOI: 10.1109/TPEL.2006.890003.

[42] J. M. Guerrero, L. G. de Vicuna, J. Matas, M. Castilla and J. Miret, 'A wireless controller to enhance dynamic performance of parallel inverters in distributed generation systems,' *IEEE Transactions on Power Electronics*, vol. 19, no. 5, pp. 1205–1213, 2004. DOI: 10.1109/TPEL.2004.833451.

[43] W. Zhang, A. Cantarellas, J. Rocabert, A. Luna and P. Rodríguez, 'Synchronous power controller with flexible droop characteristics for renewable power generation systems,' *IEEE Transactions on Sustainable Energy*, vol. 7, pp. 1572–1582, 2016.

[44] B. Johnson, S. Dhople, A. Hamadeh and P. Krein, 'Synchronization of parallel single-phase inverters with virtual oscillator control,' English (US), *IEEE Transactions on Power Electronics*, vol. 29, no. 11, pp. 6124–6138, Nov. 2014, ISSN: 0885-8993. DOI: 10.1109/TPEL.2013.2296292.

[45] M. Ashabani, F. D. Freijedo, S. Golestan and J. M. Guerrero, 'Inducverters: Pll-less converters with auto-synchronization and emulated inertia capability,' *IEEE Transactions on Smart Grid*, vol. 7, no. 3, pp. 1660–1674, 2016. DOI: 10.1109/tsg.2015.2468600.

[46] P. Mangera, F. H. Sumbung and D. Parenden, 'Automatic voltage regulator (avr) controller design based on routh's crution stability analysis in diesel-based power plants,' *Proceedings of the International Conference on Science and Technology (ICST 2018)*, 2018. DOI: 10.2991/icst-18.2018.113.

[47] P. V. D. Male and E. Lourens, 'Operational vibration-based response estimation for offshore wind lattice structures,' *Structural Health Monitoring and Damage Detection, Volume 7 Conference Proceedings of the Society for Experimental Mechanics Series*, pp. 83–96, 2015. DOI: 10.1007/978-3-319-15230-1_9.

[48] A. Abrous, R. Wamkeue and E. M. Berkouk, 'Modeling and simulation of a wind model using a spectral representation method,' *2015 3rd International Renewable and Sustainable Energy Conference (IRSEC)*, 2015. DOI: 10.1109/irsec.2015.7455141.

[49] M. Shinozuka and C.-M. Jan, 'Digital simulation of random processes and its applications,' *Journal of Sound and Vibration*, vol. 25, no. 1, pp. 111–128, 1972. DOI: 10.1016/0022-460x(72)90600-1.

[50] J. C. Kaimal, 'Turbulenece spectra, length scales and structure parameters in the stable surface layer,' *Boundary-Layer Meteorology*, vol. 4, no. 1-4, pp. 289–309, 1973. DOI: 10.1007/bf02265239.

[51] T. H. M. S. Rashid, A. Routh, M. R. Rana, A. I. Ferdous and R. Sayed, 'A novel approach to maximize performance and reliability of pmsg based wind turbine: Bangladesh perspective,' 2018.

[52] H. Al-Hamadani, T. An, M. King and H. Long, 'System dynamic modelling of three different wind turbine gearbox designs under transient loading conditions,' *International Journal of Precision Engineering and Manufacturing*, vol. 18, no. 11, pp. 1659–1668, 2017. DOI: 10.1007/s12541-017-0194-1.

[53] O. Apata and D. Oyedokun, 'An overview of control techniques for wind turbine systems,' *Scientific African*, vol. 10, 2020. DOI: 10.1016/j.sciaf.2020.e00566.

[54] G. Dudgeon, *Wind farm model in simscape: 140 wind turbines*. [Online]. Available: https://www.mathworks.com/matlabcentral/fileexchange/68597-wind-farm-model-in-simscape-140-wind-turbines.

[55] C. Bajracharya, M. Molinas, J. Suul and T. Undeland, 'Understanding of tuning techniques of converter controllers for vsc-hvdc,' Jun. 2008.

[56] L. Ping, X. Jian, K. Yong, Z. Hui and C. Jian, 'For prototype super-conducting magnetic energy storage (smes) [voltage source convertor control scheme],' *Proceedings IPEMC 2000. Third International Power Electronics and Motion Control Conference (IEEE Cat. No.00EX435)*, DOI: 10.1109/ipemc.2000.884543.

[57] M. Vujacic, O. Dordevic and G. Grandi, 'Evaluation of dc-link voltage ripple in seven-phase pwm voltage source inverters,' *2018 IEEE International Telecommunications Energy Conference (INTELEC)*, 2018. DOI: 10.1109/intlec.2018.8612327.

[58] M. Salcone and J. Bond, 'Selecting film bus link capacitors for high performance inverter applications,' *2009 IEEE International Electric Machines and Drives Conference*, 2009. DOI: 10.1109/iemdc.2009.5075431.

[59] M. Anwar and M. Teimor, 'An analytical method for selecting dc-link-capacitor of a voltage stiff inverter,' *Conference Record of the 2002 IEEE Industry Applications Conference. 37th IAS Annual Meeting (Cat. No.02CH37344)*, DOI: 10.1109/ias.2002.1042651.

[60] H. Brantsæter, Ł. Kocewiak, A. R. Årdal and E. Tedeschi, 'Passive filter design and offshore wind turbine modelling for system level harmonic studies,' *Energy Procedia*, vol. 80, pp. 401–410, 2015. DOI: 10.1016/j.egypro.2015.11.444.

Appendix

Low Emission Oil and Gas Open (LEOGO) Platform

The platform has reservoir water pressure support by injection of production water and water from subsea reservoir. A gas lift is used to reduce the weight of fluid column in borehole and reduce the bottomhole backpressure. The annual oil and gas production of the platform is considered to be 3.14 and 1.57 Million Standard cubic meters ($Mil.Sm^3$), respectively. The platform components are as followed [8]:

- Wells:
  - 15 production wells
  - 15 water injection wells (used to increase reservoir pressure)
- Energy supply:
  - 3 gas turbine generators
  - waste heat covers heat demand
  - Diesel generator for emergency backup power
- Main electric load:
  - separator trains (compressors)
  - gas lift compressor
  - gas re-compressor (increasing gas pressure after separator train)
  - oil export pumps (for transport to neighbour platform)
  - water injection pumps (produced water and seawater)
  - seawater lift pumps for injection
  - living quarters and auxiliary loads
  - drilling (rarely in operation on a production platform)

The platform has three voltage levels of $11kV, 690V$ and $400V$ supplied through various energy sources. The power sources of the LEOGO platform consist of main gas turbines, an Uninterrupted Power Supply (UPS) system and an emergency diesel generator.

Table 1: Field characteristics parameter values

Parameter	**Value**	**Comment**
Height from seabed to platform	100 m	Typical NCS value. Sea depth + platform height
Wellhead pressure	6 *MPa* (60 *bar*)	Typical NCS pressure: 25 *MPa* reservoir / 10 *MPa* well head (at seabed)
Gas injection rate for gas lift	20 *MPa* injection pressure Injection Rate (Q_{inj})/Oil Production (Q_{oil}) = 220	Q_{inj} is assumed proportional to Q_{oil}
Separator train inlet pressure	4 *MPa*	Typical values are 3-5 *MPa*(inlet pressure is controlled by choke valve)
Separator train outlet pressure	2 *MPa* (gas) 0.3 *MPa* (oil) 0.7 *MPa* (water)	
Gas export pressure	6 *MPa*	Normally 3-5 *MPa*. Ca 10 *MPa* out of compressor (and drop to 6 *MPa* at export point)
Oil export pressure	3 *MPa*	Ca 5 *MPa* out of oil pump (and 2 *MPa* pressure drop in pipe)
Water injection pressure	6 *MPa*	Somewhat higher than wellhead pressure
Well stream flow	50 Sm^3/s	sum from all wells into manifold/separator
Well stream composition	Gas Oil Ratio (GOR) = 500 Water Cut (WC) = 0.6	These numbers have been adjusted to match the gas/oil/water production: gas: 49.75 Sm^3/s = 4.3 mill Sm^3/day oil: 0.1 Sm^3/s = 8640 Sm^3/day water: 0.15 Sm^3/s = 12960 kSm^3/day (1 Sm^3 = 6.2898 barrels)
Pipe diameters	200 *mm*	Used to compute pipe friction (and hence pressure drop and pump/compressor power demand)

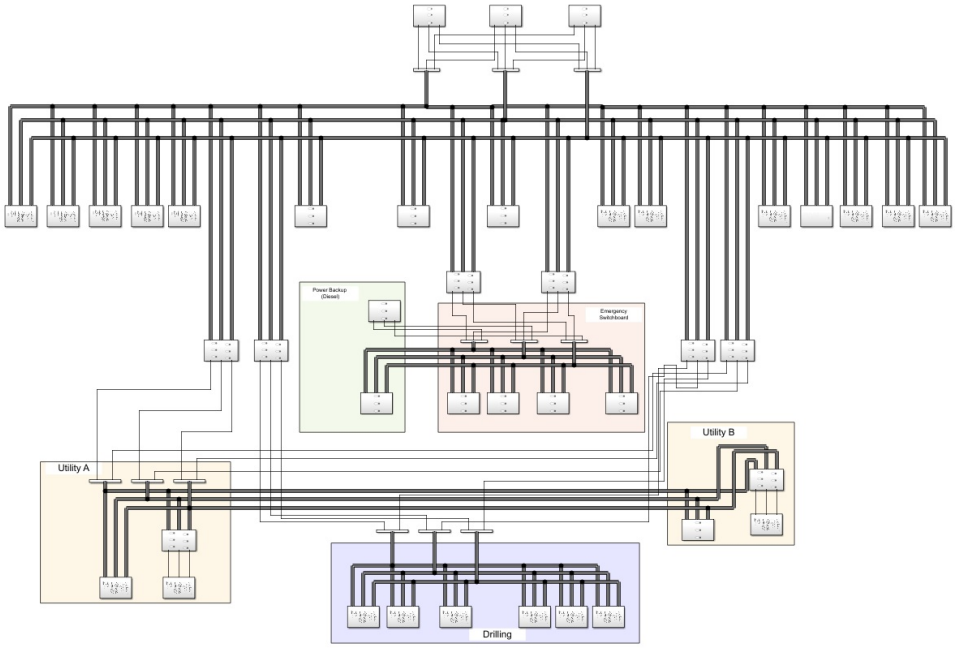

Figure 1: LEOGO platform electrical grid

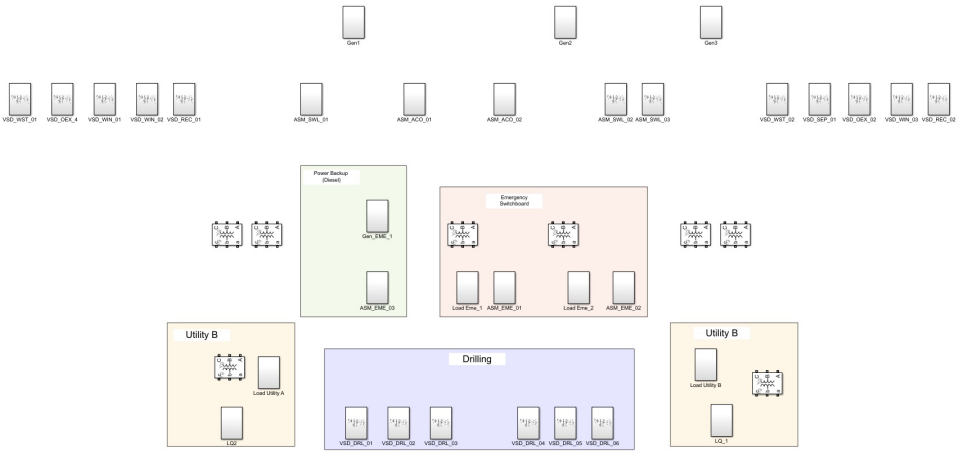

Figure 2: LEOGO platform-name of each component

Table 2: Generator data for the LEOGO platform

Generators							
		Basic				AVR	Governer and Engine
Tag Name	Description	Nominal frequency	Nominal voltage	Nominal generator power	Nominal engine power	Template	Template
Gen1	Gas turbine generator	50	11kV	28 MW	21.8 MW	IEEE_ AC8B	IEEE_GGOV1
gen2	Gas turbine generator	50	11kV	28 MW	21.8 MW	IEEE_ AC8B	IEEE_GGOV1
Gen3	Gas turbine generator	50	11kV	28 MW	21.8 MW	IEEE_ AC8B	IEEE_GGOV1
Gen_EME_1	Diesel generator	50	690V	2.8 MW	21.8 MW	IEEE_ AC8B	IEEE_GGOV1

Table 3: Transformer data for the LEOGO platform

Transformers									
Tag Name	Description	Nominal power	Primary nom. voltage	Secondary nom. voltage	Nominal frequency	Primary reactance	Primary resistance	Secondary reactance	Secondary resistance
TRA_EME_01	1.6 MVA 11/0.69 kV Dyn11 ASEA-mod.TypTr2	1.6 MW	11 kV	690 V	50	0.00396875	0.00396875	0.029736325	0.00396875
TRA_EME_02	1.6 MVA 11/0.69 kV Dyn11 ASEA-mod.TypTr2	1.6 MW	11 kV	690 V	50	0.00396875	0.00396875	0.029736325	0.00396875
TRA_Dril_01	3.3 MVA 11/0.69 kV 1.6 GEAFOL_modified.TypTr2	3.3 MW	11 kV	690 V	50	0.0549806	0.001460315	0.0549806	0.001460315
TRA_Dril_02	3.3 MVA 11/0.69 kV 1.6 GEAFOL_modified.TypTr2	3.3 MW	11 kV	690 V	50	0.0549806	0.001460315	0.0549806	0.001460315
TRA_UTL_01	0.8 MVA 11/0.69 kV Dyn11 ASEA_mod.TypTr2	0.8 MW	11 kV	690 V	50	0.02961148	0.0048125	0.02961148	0.0048125
TRA_UTL_02	0.8 MVA 11/0.69 kV Dyn11 ASEA_mod.TypTr2	0.8 MW	11 kV	690 V	50	0.02961148	0.0048125	0.02961148	0.0048125
TRA_UTL_03	0.6 MVA 0.69/0.4 kV Transformer-mod.TypTr2	0.6 MW	690 V	400 V	50	0.02961148	0.0048125	0.02961148	0.0048125
TRA_UTL_04	0.6 MVA 0.69/0.4 kV Transformer-mod.TypTr2	0.6 MW	690 V	400 V	50	0.02961148	0.0048125	0.02961148	0.0048125

143

Table 4: VSD load data for the LEOGO platform

VSD load															
Tag Name	Description	Nominal voltage	VSD power factor	VSD efficiency	Nominal active power	Nominal voltage	Nominal frequency	Nominal power factor	Nominal efficiency	Pole pairs	Inertia constant	Starting torque	Synch speed load torq	Use Load Power	Load Power
VSD_OEX_01	50Hz\11 kV\1500 kW/11 kV/1491.TypAsmo	11 kV	0.9	95.8	1.5 MW	11 kV	50	0.89	95	1	0.86	0.66	0.88	Yes	0.38 MW
VSD_OEX_02	50Hz\11 kV\1500 kW/11 kV/1491.TypAsmo	11 kV	0.9	95.8	1.5 MW	11 kV	50	0.89	95	1	0.86	0.66	0.88	Yes	0.38 MW
VSD_REC_01	50Hz\11 kV\7860 kW/11 kV/1482.TypAsmo	11 kV	0.91	96.1	7.86 MW	11 kV	50	0.8	95	1	0.8	0.55	0.91	Yes	5.8 MW
VSD_REC_02	50Hz\11 kV\7860 kW/11 kV/1482.TypAsmo	11 kV	0.91	96.1	7.86 MW	11 kV	50	0.8	95	1	0.8	0.55	0.91	Yes	5.8 MW
VSD_SEP_01	50Hz\11 kV\7860 kW/11 kV/1482.TypAsmo	11 kV	0.91	96.1	7.86 MW	11 kV	50	0.8	95	1	0.8	0.55	0.91	Yes	3.53 MW
VSD_WIN_01(1)	50Hz\11 kV\4800 kW/11 kV.TypAsmo	11 kV	0.88	96.3	4 MW	11 kV	50	0.8	95	1	0.8	0.7	0.88	Yes	3.4 MW
VSD_WIN_02(1)	50Hz\11 kV\4800 kW/11 kV.TypAsmo	11 kV	0.88	96.3	4 MW	11 kV	50	0.8	95	1	0.8	0.7	0.88	Yes	3.4 MW
VSD_WIN_03(1)	50Hz\11 kV\4800 kW/11 kV.TypAsmo	11 kV	0.88	96.3	4 MW	11 kV	50	0.8	95	1	0.8	0.7	0.88	Yes	3.4 MW
VSD_WST_01	50Hz\11 kV\4800 kW/11 kV.TypAsmo	11 kV	0.88	96.3	4 MW	11 kV	50	0.8	95	1	0.8	0.7	0.86	Yes	4.4 MW
VSD_WST_02	50Hz\11 kV\4800 kW/11 kV.TypAsmo	11 kV	0.88	96.3	4 MW	11 kV	50	0.8	95	1	0.8	0.7	0.86	Yes	4.4 MW
VSD_DRL_01	50Hz\1000 kW/0.69 kV/1.TypAsmo	690 V	0.92	96.8	1 MW	690 V	50	0.8	95	1	0.8	0.7	0.92	No	0
VSD_DRL_02	50Hz\1000 kW/0.69 kV/1.TypAsmo	690 V	0.92	96.8	1 MW	690 V	50	0.8	95	1	0.8	0.7	0.92	No	0
VSD_DRL_03	50Hz\1000 kW/0.69 kV/1.TypAsmo	690 V	0.92	96.8	1 MW	690 V	50	0.8	95	1	0.8	0.7	0.92	No	0
VSD_DRL_04	50Hz\1000 kW/0.69 kV/1.TypAsmo	690 V	0.92	96.8	1 MW	690 V	50	0.8	95	1	0.8	0.7	0.92	No	0
VSD_DRL_05	50Hz\1000 kW/0.69 kV/1.TypAsmo	690 V	0.92	96.8	1 MW	690 V	50	0.8	95	1	0.8	0.7	0.92	No	0
VSD_DRL_06	50Hz\1000 kW/0.69 kV/1.TypAsmo	690 V	0.92	96.8	1 MW	690 V	50	0.8	95	1	0.8	0.7	0.92	No	0

Table 5: PQ load data for the LEOGO platform

PQ load								
Tag Name	Description	Nominal voltage	Nominal active power	Nominal reactive power	Nominal power factor	Load mode	Voltage dependency	Minimum voltage
LQ1	General Load	400	0.5 MW	0	0.99	1	0	0.1
LQ2	LV load	400	0.5 MW	0	0.99	1	0	0.1
Load Utility A	MV Load	690	3 MW	0	0.9	1	0	0.1
Load Utility B	MV Load	690	4 MW	0	0.9	1	0	0.1
Load EME_1	General load	690	0.5 MW	0.1 MVAR	0.98	1	0	0.1
Load EME_2	General load	690	0.5 MW	0.1 MVAR	0.98	1	0	0.1

145

Table 6: Fixed speed motors data for the LEOGO platform

Motors- fixed speed											
Basic					Motor Control	Load torque					
Tag Name	Description	Nominal apparent power	Nominal frequency	Nominal voltage	Template	Starting torque	Synch. Speed load torq.	Use Load Power	Load Power	Torque speed dep., xF	Torque speed dep., xL
ASM_EME_01	50Hz\500 kW/0.69 kV/1.TypAsmo	563190 W	50	690 V	Default	0.3	0.88	No	0	2	5
ASM_EME_02	50Hz\500 kW/0.69 kV/1.TypAsmo	563190 W	50	691 V	Default	0.3	0.88	No	0	2	5
ASM_EME_03	50Hz\500 kW/0.69 kV/1.TypAsmo	563190 W	50	692 V	Default	0.3	0.88	No	0	2	5
ASM_SWL_01	50Hz\11 kV\750 kW/11 kV.TypAsmo	889648 W	50	11 kV	Default	0.3	0.87	Yes	0.75 MW	2	5
ASM_SWL_02	50Hz\11 kV\750 kW/11 kV.TypAsmo	889648 W	50	12 kV	Default	0.3	0.87	Yes	0.75 MW	2	5
ASM_SWL_03	50Hz\11 kV\750 kW/11 kV.TypAsmo	889648 W	50	13 kV	Default	0.3	0.87	Yes	0.75 MW	2	5
ASM_ACO_01	\50Hz\11 kV\3000 kW/11 kV.TypAsmo	3485819 W	50	14 kV	Default	0.3	0.89	Yes	1.75 MW	2	5
ASM_ACO_02	\50Hz\11 kV\3000 kW/11 kV.TypAsmo	3485819 W	50	15 kV	Default	0.3	0.89	Yes	1.75 MW	2	5

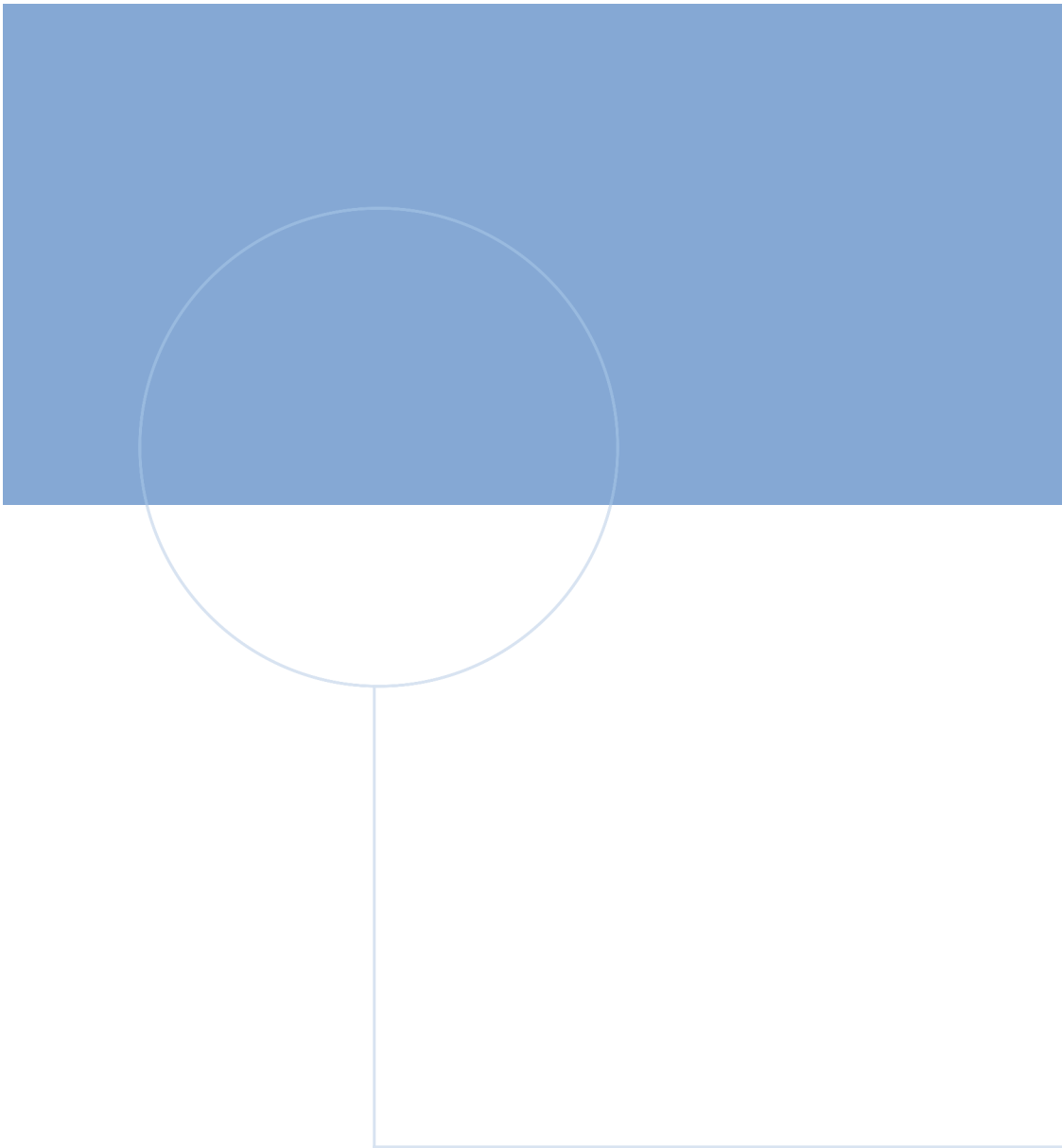

NTNU

Norwegian University of
Science and Technology